



---

Publicly Accessible Penn Dissertations

---

1985

# Profile Structures of Thin Multilayer Films by X-ray Diffraction Using Direct and Refinement Methods of Analysis

Victor Skita  
*University of Pennsylvania*

Follow this and additional works at: <https://repository.upenn.edu/edissertations>

---

## Recommended Citation

Skita, Victor, "Profile Structures of Thin Multilayer Films by X-ray Diffraction Using Direct and Refinement Methods of Analysis" (1985). *Publicly Accessible Penn Dissertations*. 3213.  
<https://repository.upenn.edu/edissertations/3213>

This paper is posted at ScholarlyCommons. <https://repository.upenn.edu/edissertations/3213>  
For more information, please contact [repository@pobox.upenn.edu](mailto:repository@pobox.upenn.edu).

---

# Profile Structures of Thin Multilayer Films by X-ray Diffraction Using Direct and Refinement Methods of Analysis

## **Abstract**

Meridional x-ray diffraction data from Langmuir-Blodgett multilayers containing two to ten molecular monolayers of arachidic acid were analyzed by two independent methods. A Patterson function deconvolution technique uniquely provided the electron density profile (8Å resolution) of the average, symmetric bilayer repeated in the multilayer. This average bilayer appeared to disorder as the number of bilayers in the multilayer decreased. A refinement technique, which does not assume a centrosymmetric structure or the existence of a unit cell, uniquely provided the profile structure of the multilayer itself. In particular it could distinguish the individual monolayers in the multilayer. Meridional x-ray scattering data from Langmuir-Blodgett multilayers composed of arachidic acid and either myristic acid or polymerized 10,12 pentacosadiynoic acid were also analyzed by the refinement technique. It found that only the last monolayer in the deposition sequence (ie. the surface monolayer) was disordered and that ordering of the surface monolayer can be induced by the deposition of an additional monolayer. In addition, an application of Langmuir-Blodgett multilayer thin films and their characterization by x-ray scattering is discussed with regards to the structural study of membrane-membrane interactions and the triggering of cellular components of the immune system.

## **Degree Type**

Dissertation

## **Degree Name**

Doctor of Philosophy (PhD)

## **First Advisor**


J. Kent Blasie

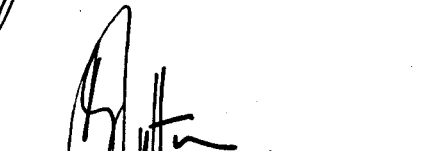
PROFILE STRUCTURES OF THIN MULTILAYER FILMS BY X-RAY  
DIFFRACTION USING DIRECT AND REFINEMENT  
METHODS OF ANALYSIS

VICTOR SKITA  
A DISSERTATION  
in  
BIOPHYSICS

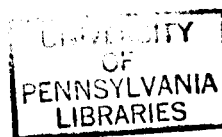
Presented to the faculties of the University of Pennsylvania in  
Partial Fulfillment of the Requirements for the Degree of Doctor of  
Philosophy

1985

  
\_\_\_\_\_  
Supervisor of Dissertation

  
\_\_\_\_\_  
Graduate Group Chairperson

QH  
002  
1985  
S628



Faint, illegible text at the top of the page, possibly bleed-through from the reverse side.

**This work is dedicated to  
my family whose unconditional  
support was always present.**

Faint, illegible text in the middle section of the page, possibly bleed-through from the reverse side.

## ACKNOWLEDGMENTS

Foremost, I would like to thank my advisor Dr. J. Kent Blasie. This dissertation would not have been possible without his guidance and insight. I am indebted to Dr. Anthony Garito for the use of his Lauda film balance and the resources in his laboratory. As my thesis committee chairman, Tony advice was invaluable. I like to thank Dr. Sol Gruner for his wise counsel throughout my graduate school career. Sol has had a profound influence on my outlook toward science. During the last five years I have had countless interactions with fellow graduate student, Robert Fischetti. It is not surprising that Bob knows my work better than any other person. We have spent hundreds of hours not only working together in developing and maintaining equipment and software, we have also analyzed, criticized, and reanalyzed each others data more times than I would like to count. Through this process I have learned a tremendous amount from Bob; what more can I say but thanks. I would like to thank Dr. Donatella Pascolini for her consistently helpful advice. For her struggles with fabricating Langmuir-Blodgett films of myristic acid, Wendy Richardson deserves a great deal of thanks. Finally, I must thank Francisco Asturias for his almost limitless source of clever ideas.

## ABSTRACT

### PROFILE STRUCTURES OF THIN MULTILAYER FILMS BY X-RAY DIFFRACTION USING DIRECT AND REFINEMENT METHODS OF ANALYSIS

Victor Skita  
J. Kent Blasie

Meridional x-ray diffraction data from Langmuir-Blodgett multilayers containing two to ten molecular monolayers of arachidic acid were analyzed by two independent methods. A Patterson function deconvolution technique uniquely provided the electron density profile (8Å resolution) of the average, symmetric bilayer repeated in the multilayer. This average bilayer appeared to disorder as the number of bilayers in the multilayer decreased. A refinement technique, which does not assume a centrosymmetric structure or the existence of a unit cell, uniquely provided the profile structure of the multilayer itself. In particular it could distinguish the individual monolayers in the multilayer. Meridional x-ray scattering data from Langmuir-Blodgett multilayers composed of arachidic acid and either myristic acid or polymerized 10,12 pentacosadiynoic acid were also analyzed by the refinement technique. It found that only the last monolayer in the deposition sequence (ie. the surface monolayer) was disordered and that ordering of the surface monolayer can be induced by the deposition of an additional monolayer. In addition, an application of Langmuir-Blodgett multilayer thin films and their characterization by x-ray scattering is discussed with regards to the structural study of membrane-membrane interactions and the triggering of cellular components of the immune system.

## TABLE OF CONTENTS

DEDICATION.....	ii
ACKNOWLEDGMENTS.....	iii
ABSTRACT.....	iv
TABLE OF CONTENTS.....	v
FIGURE SUMMARY.....	ix
PREFACE.....	xi
CHAPTER ONE	
Introduction.....	1
References for Chapter One.....	4
CHAPTER TWO	
General Theory	
Part I. Introduction.....	6
Part II. Scattering Theory.....	7
Part III. Diffraction from Infinite Systems.....	24
Part IV. Diffraction from Finite Systems.....	32
References for Chapter Two.....	36
CHAPTER THREE	
Sample Preparation and X-Ray Methods	
Part I. Multilayer Preparation.....	37

Part II. X-Ray Diffraction Methods.....	44
References for Chapter Three.....	54
<b>CHAPTER FOUR</b>	
<b>Results</b>	
Part I. Arachidic Acid Multilayers.....	55
Part II. Arachidic Acid, Myristic Acid, and 10,12 Pentacosadiynoic Acid Mixed Multilayers.....	60
<b>CHAPTER FIVE</b>	
<b>Analysis</b>	
Part I. Arachidic Acid Multilayers.....	70
Part II. Arachidic Acid, Myristic Acid, and 10,12 Pentacosadiynoic Acid Mixed Multilayers.....	91
References for Chapter Five.....	100
<b>CHAPTER SIX</b>	
<b>Discussion</b>	
Part I. Arachidic Acid Multilayers: Box Refinement.....	101
Part II. Arachidic Acid Multilayers: Model Calculations.....	111
Part III. Arachidic Acid, Myristic Acid, and 10,12 Pentacosadiynoic Acid Mixed Multilayers.....	118



<b>CHAPTER SEVEN</b>	
Conclusion.....	122
References for Chapter Seven.....	126
<b>CHAPTER EIGHT</b>	
The Study of Thin Multilayer Films — A Discussion of a Biophysical Application.....	127
References for Chapter Eight.....	131
<b>APPENDIX I</b>	
Fourier Transform of an Infinite Periodic Array of Delta Functions.....	132
<b>APPENDIX II</b>	
Shifting of Diffraction Maxima for Multilayers of Finite Extent.....	134
<b>APPENDIX III</b>	
Reconstruction of the Unit Cell Patterson by the Method of Linear Equations.....	135
<b>APPENDIX IV</b>	
Direct Deconvolution Method.....	138
<b>APPENDIX V</b>	
Fourier Synthesis of the Electron Density Profile.....	142

**APPENDIX VI**

**Box Refinement Technique..... 144**

**APPENDIX VII**

**Symmetric and Antisymmetric Contributions of the  
Electron Density Profile to the Intensity Function... 148**

**BIBLIOGRAPHY..... 149**

**INDEX..... 153**

## FIGURE SUMMARY

Figure 1.	Ewald's Sphere of Reflection.....	31
Figure 2.	Isotherms, Arachidic Acid and 10,12 Pentacosadiynoic Acid.....	43
Figure 3A.	Rocking Curve, Arachidic Acid N=5.....	50
Figure 3B.	Rocking Curve, Arachidic Acid N=1.....	51
Figure 4.	OTS Scattering.....	53
Figure 5.	Corrected Intensity Functions, Arachidic Acid N=1,2,3,5.....	57
Figure 6.	Multilayer Patterson Functions, Arachidic Acid N=1,2,3,5.....	59
Figure 7.	Corrected Intensity Functions for AAMM, AAAM, and AAAA multilayers.....	63
Figure 8.	Multilayer Patterson Functions for AAMM, AAAM, and AAAA multilayers.....	65
Figure 9.	Corrected Intensity Functions for DDDA and DDD multilayers.....	67
Figure 10.	Multilayer Patterson Functions for DDDA and DDD multilayers.....	69
Figure 11.	Unit Cell Patterson Functions, Arachidic Acid N=2,3,5.....	78
Figure 12.	Unit Cell Deconvolution, Arachidic Acid N=2,3,5.....	80
Figure 13.	Fourier Synthesis, Arachidic Acid N=2,3,5.....	82
Figure 14.	Unit Cell Electron Density Profile for DPPC, 35°C and 49°C.....	84
Figure 15.	Model Electron Density Profiles.....	86
Figure 16.	Model Electron Density Profile Calculated Intensity Functions.....	88

Figure 17. Box Refinement Multilayer Profiles, Arachidic Acid N=1,2,3.....	90
Figure 18A. Corefinement Multilayer Profiles, AAAM <i>versus</i> AAAA.....	95
Figure 18B. Corefinement Multilayer Profiles, AAMM <i>versus</i> AAAA.....	96
Figure 18C. Corefinement Multilayer Profiles, AAMM <i>versus</i> AAAM.....	97
Figure 19. Corefinement Multilayer Profiles, DDDA <i>versus</i> DDD.....	99
Figure 20. Step-Function Equivalent Models, Arachidic Acid N=1,2,3.....	106
Figure 21. Calculated Intensity Functions, Arachidic Acid N=2.....	108
Figure 22. Calculated Patterson Functions, Arachidic Acid N=2.....	110
Figure 23. Calculated Intensity Function, Arachidic Acid N=2 showing Asymmetric Contribution.....	117

1953, p. 100.

... of the structure of any arbitrary substance from the intensity data alone. It is only a question of precision of measurement and, consequently, how large is number of solutions.

**Except for some asymmetric substances, in principle there is nothing which prevents a direct determination of the structure of any arbitrary substance from the intensity data alone. It is only a question of precision of measurement and, consequently, how large is number of solutions.**

—from *Hosemann and Bagchi*  
*Direct Analysis of Diffraction by Matter.*  
*North-Holland Publishing Company, 1962.*

## CHAPTER ONE: INTRODUCTION

X-ray diffraction from oriented fatty acid ( $\text{CH}_3\text{-[CH}_2\text{]}_n\text{-COOH}$ ) multilayers was observed and first interpreted by Müller [1-1] and Müller and Shearer [1-2] in 1923. They concluded that a "complete [structural] solution" was not plausible at that time, and settled for calculating the average methyl ( $-\text{CH}_3$ ) to carboxyl ( $-\text{COOH}$ ) spacing from their powder patterns.

Fatty acid monolayers were first deposited onto solid glass substrates by Katherine Blodgett [1-3, 1-4] and later by Blodgett and Langmuir [1-5]. X-ray diffraction studies of these Langmuir-Blodgett films deposited onto metal [1-6] and glass [1-7] substrates soon followed. Holley and Bernstein [1-8] speculated Langmuir-Blodgett films could be used to study the correlation between the number of cooperating Langmuir-Blodgett monolayers with the experimental line widths observed in the diffraction patterns.

In a series of papers Irving Langmuir and Vincent Schafer discuss the fabrication of Langmuir-Blodgett films that either incorporate proteins during the film deposition process [1-9, 1-10] or by conditioning the surface of an Langmuir-Blodgett film so as to adsorb proteins from solution [1-10, 1-11, 1-12]. They used optical methods to measure the thickness of their protein (urease, pepsin, albumin, or cholesterol) layers. More recently, McLean [1-13] outlined the procedure for the fabrication (via the Langmuir-Blodgett technique) of stable polar substrates using diacetylene containing molecules.

Kopp *et al.* [1-14] have pointed out that membrane proteins should ideally be studied at an interface between high dielectric (water) and low dielectric (membrane) phases. Investigations on the functional interactions between biological cells [1-15], and on antibody-antigen interactions [1-16, 1-17] use Langmuir-Blodgett films as a model system. The study of transmembrane potentials [1-18], for instance, which depend critically on the orientation of the membrane proteins could be enhanced by fabricating appropriate Langmuir-Blodgett protein films. The detailed structural study and analysis of simple Langmuir-Blodgett systems composed of only a few molecular monolayers is critical if one wishes to study the structural-functional relationship of membrane proteins in Langmuir-Blodgett films.

X-ray diffraction can in principle be used to investigate the structure of these simple, very thin multilayer films containing only a few molecular monolayers deposited on solid substrates by the Langmuir-Blodgett technique. One would like to ascertain whether the structures of the individual monolayers differ from one another and particularly whether the substrate perturbs certain individual monolayers in the multilayer film. Previous analyses of the meridional x-ray diffraction from such multilayer films have employed either a non-unique modeling of the multilayer electron density profile to fit the observed diffraction data [1-19] or direct methods (multilayer profile Patterson function deconvolution [1-20] and counter-ion isomorphous replacement [1-21]) to uniquely derive the

electron density profile of the average, symmetric bilayers or bilayer pairs repeated in the multilayer. Most methods of unambiguous structural analysis employing x-ray scattering are limited in that they require (or assume) the repetition of some average structural unit (unit cell) in a periodic array of effectively infinite extent.

This study is composed of two parts. In part one meridional x-ray diffraction data from multilayers containing one, two, three and five bilayers of arachidic acid deposited on alkylated glass substrates was collected. Data from these multilayers were analyzed by two independent methods for comparative purposes. A Patterson function deconvolution technique [1-20] provided uniquely the electron density profiles (8Å resolution) of the average, symmetric bilayer as a function of the number of times  $N$  ( $N = 2, 3, 5$ ) it was repeated in the multilayer. A box-refinement technique [1-22, 1-23] for the homologous series of multilayer structures  $N = 1, 2, 3$  uniquely provided the electron density profile (8Å resolution) of the multilayer itself, namely of each individual monolayer as a function of its position in the three multilayers.

The second part consists of studying Langmuir-Blodgett multilayers composed of monolayers of different amphiphilic macromolecular species each have different chain lengths. Direct methods assuming a repeating unit cell could thus not be employed; rather a variant of the box refinement technique was used to study these mixed multilayer systems.



#### REFERENCES FOR CHAPTER ONE

- [1-1] Müller, A. The X-ray Investigation of Fatty-Acids. *J. Chem Society*. 123:2043-2047 (1923)
- [1-2] Müller, A., Shearer, G. Further X-Ray Measurements of Long-chain Compounds and a Note on their Interpretation. *J. Chem Society*. 123:3156-3164 (1923)
- [1-3] Blodgett, K. Monomolecular Films of Fatty Acids on Glass. *JACS*. 56:495 (1934)
- [1-4] Blodgett, K. Successive Monomolecular Layers on a Solid Surface. *JACS*. 57:1007-1022 (1935)
- [1-5] Blodgett, K., Langmuir, I. Built-up Films of Barium Stearate and their Optical Properties. *Physical Review*. 51:964-982 (1937)
- [1-6] Clark, G., Sterrett, R., Leppla, P. X-ray Diffraction Studies of Built-up Films of Long-Chain Compounds. *JACS*. 56:495-496 (1934)
- [1-7] Clark, G., Leppla, P. X-ray Diffraction Studies of Built-up Films. *JACS*. 58:2199-2201 (1936)
- [1-8] Holley, C., Bernstein, S. X-ray Diffraction by a Film of Counted Molecular Layers. *Phys. Rev.* 49:403 (1936)
- [1-9] Langmuir, I., Schaefer, V., Wrinch, D. Built-up Films of Proteins and their Properties. *Science* 85:76-80 (1937)
- [1-10] Langmuir, I., Schaefer, V. Activities of Urease and Pepsin Monolayers. *JACS* 60:135[1-1357 (1938)
- [1-11] Langmuir, I., Schaefer, V. Optical Measurements of the Thickness of a Film Adsorbed From a Solution. *JACS* 59:1406 (1937)
- [1-12] Langmuir, I., Schaefer, V. Improved Methods of Conditioning Surfaces for Adsorption. *JACS* 59:1762-1763 (1937)
- [1-13] McLean, L., Durrani, A., Whittam, M., Johnston, D., Chapman, D. Preparation of Stable Polar Surfaces Using Polymerizable Long-Chain Diacetylene Molecules. *Thin Solid Films* 99:127-131 (1983)

- [1-14] Kopp, F., Cuendet, P., Mühlethaler, K., Zuber, H. Hydrophobic Membrane Protein from Chromatophores of *Rhodospirillum Rubrum*. Structural and Spectroscopic Studies of Monolayers and Multilayers. *BBA* 553:438-449 (1979)
- [1-15] Tschärner, V., McConnell, H. Physical Properties of Lipid Monolayers on Alkylated Planar Glass Surfaces. *Biophys. J.* 36:421-427 (1981)
- [1-16] Hafeman, D., Tschärner, V., McConnell, H. Specific Antibody-Dependent Interactions between Macrophages and Lipid Haptens in Planar Lipid Monolayers. *PNAS* 78:4552-4556 (1981)
- [1-17] Uzigiris, E., Kornberg, R. Two-dimensional Crystallization Technique for Imaging Macromolecules, with Application to Antigen-Antibody-Complement Complexes. *Nature* 301:125-129 (1983)
- [1-18] Packham, N., Dutton, P.L., Mueller, P. Photoelectric Currents Across Planar Bilayer Membranes Containing Bacterial Reaction Centers. *Biophys. J.* 37:465-473 (1982)
- [1-19] Pomerantz, M., Segmüller, A. High Resolution X-ray Diffraction From Small Numbers of Langmuir-Blodgett Layers of Manganese Stearate. *Thin Solid Films* 68:33-45 (1980)
- [1-20] Lesslauer, W., Blasie, J.K. Direct determination of the Structure of Barium Stearate Multilayers by X-ray Diffraction. *Biophys. J.* 12:175-190 (1972)
- [1-21] McIntosh, T., Waldbillig, R., Robertson, D. Lipid Bilayer Ultrastructure Electron Density Profiles and Chain Tilt Angles as Determined by X-ray Diffraction. *BBA* 448:15-33 (1976)
- [1-22] Stroud, R., Agard, D. Structure Determination of Asymmetric Membrane Profiles Using an Iterative Fourier Method. *Biophys. J.* 25:495-512 (1979)
- [1-23] Makowski, L. The Use of Continuous Diffraction Data as a Phase Constraint. I. One-Dimensional Theory. *J. Appl. Cryst.* 14:160-168 (1981)

## CHAPTER TWO: GENERAL THEORY

### Part I. Introduction

The general theory presented herein attempts to concisely review scattering theory, and then extend the basic concepts to diffraction from both infinite and finite one-dimensional systems. The quantum mechanical derivation of scattering is well known; the formalism used is based largely on Eugen Merzbacher's approach [2-1] and somewhat on that of Gordon Baym [2-2]. The extension of general scattering theory to x-radiation comes from Hoseman and Bagchi [2-3] and John Coley [2-4]. The discussion of diffraction from an infinite system is based on Ashcroft and Mermin [2-5] and Coley [2-4]. Diffraction from a finite system is discussed in detail by Hoseman and Bagchi [2-3], and to a lesser extent by Coley [2-4].

## Part II. Scattering Theory

Scattering involves the bombardment of atoms in a target with a beam of particles. These particles are scattered by the target atoms and are detected as an intensity. This intensity varies with scattering angle. Quantum mechanically, we wish to derive the eigenfunctions of the scattered beam; this being directly related to the observed intensities, or likelihood of finding a particle at a certain place.

Certain assumptions are made. 1) The effect of the scattering center on the particles can be represented by a potential  $V(r)$  which falls to zero within a finite region of the scattering center. This would exclude a pure Coulombic field. 2) The scattering is elastic (ie. without energy loss or gain by the projectile) 3) The incident particles do not interact with each other.

The Hamiltonian is given by:

$$\begin{aligned} \mathcal{H} &= \mathcal{H}_0 + V(r) \\ &= -\frac{\hbar^2}{2\mu} \nabla^2 + V(r) \end{aligned} \quad (\text{II-1})$$

The incident particles can be represented by a wave packet of the form:

$$\psi(r,0) = (2\pi)^{-3/2} \int \phi(k) \exp[ik \cdot (r-r_0)] d^3k \quad (\text{II-2})$$

where  $\phi(k)$  is the momentum distribution. It is assumed that  $\phi(k)$  is centered on  $k = k_0$ , and is non-zero in the vicinity of  $k_0$ . Note,  $\phi(k)$  and  $\psi(r,0)$  are related by a Fourier transform.

If  $\psi(r,0)$  can be expanded in terms of its eigenfunctions  $\psi_n(r)$ :

$$\psi(r,0) = \sum_n c_n \psi_n(r)$$

then  $\psi(r,t)$  is given by:

$$\psi(r,t) = \sum_n c_n \psi_n(r) \exp\left[-\frac{i}{\hbar} E_n t\right] \quad (\text{II-3})$$

Equation (II-3) describes the eigenfunctions of the Hamiltonian  $\mathcal{H}_0$  and not  $\mathcal{H}$ . The eigenfunctions for  $\mathcal{H}_0$  are the solution of a free particle with eigenvalues  $E_n$ . However, if we can find a solution  $\psi_k(r)$  that satisfies Schrödinger's equation:

$$\mathcal{H}\psi_k = E\psi_k \quad (\text{II-4})$$

equation (II-2) after substituting  $\psi_k$  for the free particle solution,  $\exp[ik \cdot r]$ , would yield:

$$\psi(r,0) = \int \phi(k) \exp[-ik \cdot r_0] \psi_k(r) d^3k \quad (\text{II-5})$$

From equation (II-3) we would then obtain:

$$\psi(r,t) = \int \phi(k) \exp[-ik \cdot r_0] \psi_k(r) \exp\left[-\frac{i}{\hbar} E_k t\right] d^3k$$

$$\psi(r,t) = \int \phi(k) \exp[-ik \cdot r_0 - i\omega t] \psi_k(r) d^3k \quad (\text{II-6})$$

$$\text{where } \hbar\omega = E_k = \frac{\hbar^2 k^2}{2\mu}$$

The problem then reduces to finding an appropriate wave function  $\psi_k(r)$  that satisfies equation (II-4).

Solving (II-4) for  $\psi_k(r)$  after substituting (II-1) yields:

$$-\frac{\hbar^2}{2\mu} \nabla^2 \psi_k + V(r)\psi_k = E_k \psi_k$$

$$\nabla^2 \psi_k + \frac{2\mu}{\hbar^2} E_k \psi_k = V(r) \frac{2\mu}{\hbar^2} \psi_k$$

$$(\nabla^2 + k^2) \psi_k = U(r)\psi_k \quad (\text{II-7})$$

where  $k^2 = \frac{2\mu}{\hbar^2} E$

and  $U(r) = \frac{2\mu}{\hbar^2} V(r)$

Equation (II-7) is solved by solving the homogenous equation:

$$(\nabla^2 + k^2) \psi_k = 0 \quad (\text{II-8})$$

and then finding the particular solution. The solution to (II-8) is just the wave function for a free particle:

$$\psi_{k, \text{hg}} = (2\pi)^{-\frac{3}{2}} \exp[i\mathbf{k} \cdot \mathbf{r}] \quad (\text{II-9})$$

To find the particular solution, let us consider the family of functions defined by:

$$(\nabla^2 + k^2) G(\mathbf{r}, \mathbf{r}') = -4\pi\delta(\mathbf{r} - \mathbf{r}')$$

where  $G(\mathbf{r}, \mathbf{r}')$  is known as Green's function.

By inspection, the solution to the inhomogenous equation (II-7) is:

$$\psi_k(\mathbf{r}) = -1/4\pi \int U(\mathbf{r}') G(\mathbf{r} - \mathbf{r}') \psi_k(\mathbf{r}') d^3\mathbf{r}' \quad (\text{II-10})$$

This can be verified by substituting (II-10) into equation (II-7).

$$(\nabla^2 + k^2) \psi_k = U(\mathbf{r}) \psi_k$$

$$U(\mathbf{r})\psi_{\mathbf{k}} = -1/4\pi \int (\nabla^2 + k^2) U(\mathbf{r}') \times \\ G(\mathbf{r}-\mathbf{r}') \psi_{\mathbf{k}}(\mathbf{r}') d^3\mathbf{r}'$$

$$U(\mathbf{r})\psi_{\mathbf{k}} = \int \delta(\mathbf{r}-\mathbf{r}') U(\mathbf{r}') \psi_{\mathbf{k}}(\mathbf{r}') d^3\mathbf{r}'$$

$$U(\mathbf{r})\psi_{\mathbf{k}} = U(\mathbf{r})\psi_{\mathbf{k}}$$

QED

We must now find an appropriate Green's function.  $G(\mathbf{r},\mathbf{r}')$  can be defined in terms of the Fourier transform of  $g(\mathbf{k}')$ .

$$G(\mathbf{r}-\mathbf{r}') = \int g(\mathbf{k}') \exp[i\mathbf{k}' \cdot (\mathbf{r}-\mathbf{r}')] d^3\mathbf{k}' \quad (\text{II-11})$$

Multiplying the left and right side of (II-11) by  $(\nabla^2 + k^2)$  and using the definition of Green's function yields:

$$-4\pi\delta(\mathbf{r}-\mathbf{r}') = \int g(\mathbf{k}') \nabla^2 \exp[i\mathbf{k}' \cdot (\mathbf{r}-\mathbf{r}')] d^3\mathbf{k}' + \\ k^2 \int g(\mathbf{k}') \exp[i\mathbf{k}' \cdot (\mathbf{r}-\mathbf{r}')] d^3\mathbf{k}' \quad (\text{II-12})$$

Substituting the Dirac delta function:

$$\delta(\mathbf{r}) = (1/2\pi)^3 \int \exp[i\mathbf{k}' \cdot \mathbf{r}] d^3\mathbf{k}'$$

into (II-12) and letting  $\mathbf{r}' = 0$  (for convenience) yields:

$$-4\pi(1/2\pi)^3 \int \exp[i\mathbf{k}' \cdot \mathbf{r}] d^3\mathbf{k}' = \\ \int g(\mathbf{k}') [k^2 - k'^2] \exp[i\mathbf{k}' \cdot \mathbf{r}] d^3\mathbf{k}'$$

Thus

$$g(\mathbf{k}') = \frac{1}{2\pi^2} [k^2 - k'^2]^{-1}$$

and

$$G(\mathbf{r}) = \frac{1}{2\pi^2} \int [k'^2 - k^2]^{-1} \exp[i\mathbf{k}' \cdot \mathbf{r}] d^3\mathbf{k}'$$

Integrating over the angles yields:

$$G(\mathbf{r}) = \int_{-\infty}^{+\infty} \frac{\exp[i\mathbf{k}' \cdot \mathbf{r}]}{k'^2 - k^2} dk'$$

The above integral has singularities at  $k' = \pm k$ . By choosing an appropriate contour and using the residue theorem we can solve for Green's function:

$$G(\mathbf{r}) = \frac{\exp[ikr]}{r}$$

For  $r' \neq 0$  we have a more generalized result:

$$G(\mathbf{r}, \mathbf{r}') = \frac{\exp[ik|\mathbf{r} - \mathbf{r}'|]}{|\mathbf{r} - \mathbf{r}'|} \quad (\text{II-13})$$

Substituting (II-13) into (II-10) yields the particular solution:

$$\psi_{k,pt} = -1/4\pi \int U(\mathbf{r}') \frac{\exp[ik|\mathbf{r} - \mathbf{r}'|]}{|\mathbf{r} - \mathbf{r}'|} \psi_k(\mathbf{r}') d^3\mathbf{r}'$$

The sum of the homogeneous solution (II-9) and the particular solution is the general solution to equation (II-10):



$$\psi_k = (2\pi)^{-3/2} \exp[ik \cdot r] -$$

$$1/4\pi \int U(r') \frac{\exp[ik|r-r'|]}{|r-r'|} \psi_k(r') d^3r'$$

If we assume that we observe the scattering far from the target (ie. the Fraunhofer condition, namely  $r' \ll r$ ) the following approximation can be made.

$$k|r-r'| = kr - k\hat{r} \cdot r' + \frac{k(\hat{r} \times r')^2}{2r} + \dots$$

$$k|r-r'| \sim kr - k\hat{r} \cdot r'$$

$$\text{Let } k' = k\hat{r}$$

$$\text{then } k|r-r'| \sim kr - k' \cdot r'$$

Substituting into the general solution yields the well-known asymptotic solution:

$$\psi_k \sim (2\pi)^{-3/2} \exp[ik \cdot r] -$$

$$1/4\pi \int U(r') \frac{\exp[ikr]}{r} \times \exp[-ik' \cdot r'] \psi_k(r') d^3r'$$

$$\psi_k \sim (2\pi)^{-3/2} \exp[ik \cdot r] -$$

$$\frac{\exp[ikr]}{4\pi r} \times$$

$$\int U(r') \exp[-ik' \cdot r'] \psi_k(r') d^3r'$$

$$\psi_k \sim (2\pi)^{-3/2} \left[ \exp[-ik \cdot r] + \frac{\exp[ikr]}{r} f_k(k') \right]$$

where

$$f_k(k') = -\frac{(2\pi)^{\frac{3}{2}}}{4\pi} \int \exp[-ik' \cdot r'] U(r') \psi_k(r') d^3r' \quad (\text{II-14})$$

Substituting (II-14) into equation (II-6) yields:

$$\begin{aligned} \psi(r, t) = & \int \phi(k) \exp[-ik \cdot r_0 - i\omega t] \times \\ & \left[ \frac{1}{(2\pi)^{\frac{3}{2}}} \exp[ik \cdot r] + \frac{\exp[ikr]}{r} f_k(k') \right] \times \\ & d^3k \quad (\text{II-15}) \end{aligned}$$

$$\begin{aligned} \text{Since } \omega &= \frac{\hbar}{2\mu} k^2 \\ &= \frac{\hbar}{2\mu} [k_0 + (k - k_0)]^2 \\ &= \frac{\hbar}{2\mu} [2k_0 \cdot k - k_0^2 + (k - k_0)^2] \end{aligned}$$

If we assume  $(k - k_0)^2 \rightarrow 0$  (ie. the wave packet does not spread appreciably when it is displaced by the macroscopic distance  $r_0$ ), we obtain from the above expansion of  $\omega$ :

$$\omega \sim \frac{\hbar}{2\mu} [2k_0 \cdot k - k_0^2]$$

$$\begin{aligned} \text{then } -i[k \cdot r_0 - \omega t] &= -ik \cdot r_0 - i \frac{\hbar}{2\mu} [2k_0 \cdot k - k_0^2] t \\ &= -ik \cdot r_0 - i \left( \frac{\hbar}{\mu} k_0 \cdot kt \right) + i \frac{\hbar}{2\mu} k_0^2 t \\ &= -ik \cdot r_0 - i v_0 t + i \omega_0 t \end{aligned}$$

where  $v_0 = \frac{\hbar k_0}{\mu}$

and  $\omega_0 = \frac{\mu}{2\hbar} v_0^2$

Equation (II-15) can now be rewritten:

$$\psi(\mathbf{r}, t) = \int \phi(\mathbf{k}) \exp[-i\mathbf{k} \cdot (\mathbf{r}_0 + \mathbf{v}_0 t) + i\omega_0 t] \times$$

$$\left[ \frac{1}{(2\pi)^{\frac{3}{2}}} \exp[i\mathbf{k} \cdot \mathbf{r}] + \frac{\exp[i\mathbf{k} \cdot \mathbf{r}]}{r} f_{\mathbf{k}}(\mathbf{k}') \right] \times$$

$$d^3\mathbf{k}$$

$$\psi(\mathbf{r}, t) = \int \left[ \phi(\mathbf{k}) \exp[-i\mathbf{k} \cdot (\mathbf{r}_0 + \mathbf{v}_0 t) + i\omega_0 t] \times$$

$$\frac{1}{(2\pi)^{\frac{3}{2}}} \exp[i\mathbf{k} \cdot \mathbf{r}] \right] d^3\mathbf{k} +$$

$$\int \left[ \phi(\mathbf{k}) \exp[-i\mathbf{k} \cdot (\mathbf{r}_0 + \mathbf{v}_0 t) + i\omega_0 t] \times$$

$$\frac{1}{(2\pi)^{\frac{3}{2}}} \frac{\exp[i\mathbf{k} \cdot \mathbf{r}]}{r} f_{\mathbf{k}}(\mathbf{k}') \right] d^3\mathbf{k}$$

With the help of equation (II-6) for  $\mathbf{r} \rightarrow \mathbf{r} - \mathbf{v}_0 t$  we obtain:

$$\psi(\mathbf{r}, t) = \psi(\mathbf{r} - \mathbf{v}_0 t, 0) \exp[i\omega_0 t] +$$

$$\frac{1}{(2\pi)^{\frac{3}{2}}} \int \left[ \phi(\mathbf{k}) \exp[i\omega_0 t] \times$$

$$\exp[i(\mathbf{k} \cdot \mathbf{r} - \mathbf{k} \cdot (\mathbf{r}_0 + \mathbf{v}_0 t))] \frac{1}{r} f_{\mathbf{k}}(\mathbf{k}') \right] d^3\mathbf{k} \quad (\text{II-16})$$

Since we assumed  $\phi(k)$  differs from zero only for  $k \approx k_0$  then:

$$kr = k \cdot \hat{k} r$$

$$\sim k \cdot \hat{k}_0 r$$

$$\text{and } kr = k \cdot (r_0 + v_0 t) \sim k \cdot \hat{k}_0 r - k \cdot (r_0 + v_0 t)$$

$$\sim k \cdot (\hat{k}_0 r - r_0 + v_0 t)$$

Substituting  $kr$  from above in (II-16) and comparing the result to equation (II-2) yields:

$$\psi(r, t) = \psi(r - v_0 t, 0) \exp[i\omega_0 t] +$$

$$\frac{f_k(k')}{r} \psi(r\hat{k}_0 - v_0 t, 0) \exp[i\omega_0 t] \quad (\text{II-17})$$

Equation (II-17) applies itself to an easy physical interpretation of the scattering problem. The first term, aside from a phase factor ( $\exp[i\omega_0 t]$ ) is just the initial wave packet displaced without change in shape; the second term is a radially expanding replica of the initial wave packet as seen by the scatterer, reduced in amplitude by a factor  $f_k(k')/r$ .  $f_k(k')$  is known as the scattering amplitude.

Equation (II-14) can be rewritten in terms of  $V(r')$ :

$$f_k(k') = - \frac{(2\pi)^{3/2} \mu}{\hbar^2} \int \exp[-ik' \cdot r'] V(r') \psi_k(r') d^3 r'$$

where  $V(r') = \frac{\hbar^2}{2\mu} U(r)$

This not an explicit expression for  $f_k(k')$  since  $\psi_k$  is in the integrand. The first-order Born approximation replaces  $\psi_k(r')$  with a plane wave:

$$\psi(\mathbf{r}') \sim (2\pi)^{-3/2} \exp[i\mathbf{k} \cdot \mathbf{r}'] \quad (\text{II-18})$$

to yield:

$$f_{\mathbf{k}}(\mathbf{k}') \sim \frac{-\mu}{2\pi\hbar^2} \int \exp[-i\mathbf{k}' \cdot \mathbf{r}'] V(\mathbf{r}') \exp[i\mathbf{k} \cdot \mathbf{r}'] d^3r' \quad (\text{II-19})$$

In the first Born approximation the scattering amplitude is proportional to the matrix element of the scattering potential between an incoming and an outgoing plane waves. Scattering can thus be looked upon as a perturbation of the incident particle by some potential distribution. This approximation is valid for weak potentials and high incident energies.

Equation (II-19) can be rewritten to yield:

$$f_{\mathbf{k}}(\mathbf{k}') \sim - \frac{\mu}{2\pi\hbar^2} \int V(\mathbf{r}') \exp[-i(\mathbf{k}' - \mathbf{k}) \cdot \mathbf{r}'] d^3r'$$

let  $2\pi\mathbf{q} = -(\mathbf{k}' - \mathbf{k})$

then

$$f_{\mathbf{k}}(\mathbf{q}) \sim - \frac{\mu}{2\pi\hbar^2} \int V(\mathbf{r}') \exp[2\pi i\mathbf{q} \cdot \mathbf{r}'] d^3r' \quad (\text{II-20})$$

Equation (II-20) is a general solution to scattering of a particle wave by a potential. It is valid for neutrons, electrons, and x-rays. For x-rays we can substitute for the reduced mass  $\mu$  (equation II-21) to yield (II-22).

$$p = \frac{h}{\lambda} = \mu c$$

$$\therefore \mu = \frac{h}{c\lambda} \quad (\text{II-21})$$

$$f_{\mathbf{k}}(\mathbf{q}) \sim -\frac{1}{c\lambda h} \int V(\mathbf{r}') \exp[2\pi i \mathbf{q} \cdot \mathbf{r}'] d^3 r' \quad (\text{II-22})$$

Since the scattering potential is proportional to the electron density distribution,  $-\rho(\mathbf{r}')$ , for x-ray scattering we obtain:

$$F(\mathbf{q}) = \int \rho(\mathbf{r}') \exp[2\pi i \mathbf{q} \cdot \mathbf{r}'] d^3 r'$$

where  $F(\mathbf{q})$  is called the structure factor or structure amplitude and is equal to  $f_{\mathbf{k}}(\mathbf{q})$ . Substituting  $\mathbf{r}$  for  $\mathbf{r}'$  for simplicity yields:

$$F(\mathbf{q}) = \int \rho(\mathbf{r}) \exp[2\pi i \mathbf{q} \cdot \mathbf{r}] d^3 r \quad (\text{II-23})$$

Equation (II-23) states that the structure factor is proportional to the Fourier transform of the electron density distribution. Inversely the Fourier transform of the structure factor is proportional to the electron density distribution (II-24).

$$\rho(\mathbf{r}) = \int F(\mathbf{q}) \exp[-2\pi i \mathbf{q} \cdot \mathbf{r}] d^3 q \quad (\text{II-24})$$

From an experimental point of view, it is the differential cross section (which represents the number of scattering particles in a given area  $d\sigma$  per solid angle  $d\Omega$ ) which is most interesting. The differential cross section is proportional to what is measured in a scattering experiment, and is given by:

$$\frac{d\sigma}{d\Omega} = |f_{\mathbf{k}}(\mathbf{k}')|^2 \quad (\text{II-25})$$

The ratio of the observed intensity  $I(\mathbf{q})$  to the total incident beam intensity  $I_0(\mathbf{q})$  (ie.  $\psi\psi^*$ ) is equal to the differential cross section; therefore, the observed intensity is proportional to the structure factor multiplied by its complex conjugate.

$$I(\mathbf{q}) = F(\mathbf{q}) \cdot F^*(\mathbf{q}) \quad (\text{II-26})$$

Substituting equation (II-25) with the understanding that  $I(\mathbf{q})$  represents a relative intensity (thus eliminating the proportional symbol) yields:

$$I(\mathbf{q}) = \int \rho(\mathbf{r}') \exp[2\pi i \mathbf{q} \cdot \mathbf{r}'] d^3 \mathbf{r}' \times \int \rho(\mathbf{r}) \exp(-2\pi i \mathbf{q} \cdot \mathbf{r}) d^3 \mathbf{r}$$

If we choose  $\mathbf{r}' = \mathbf{r} + \mathbf{u}$  and integrate over  $d^3 \mathbf{u}$ , the above expression becomes:

$$I(\mathbf{q}) = \int \rho(\mathbf{r} + \mathbf{u}) \exp[2\pi i \mathbf{q} \cdot (\mathbf{r} + \mathbf{u})] d^3 \mathbf{u} \times \int \rho(\mathbf{r}) \exp[-2\pi i \mathbf{q} \cdot \mathbf{r}] d^3 \mathbf{r}$$

Rearranging yields:

$$= \int \exp[-2\pi i \mathbf{q} \cdot \mathbf{u}] \left[ \int \rho(\mathbf{r}) \rho(\mathbf{r} + \mathbf{u}) d^3 \mathbf{r} \right] d^3 \mathbf{u} \quad (\text{II-27})$$

If we let:

$$P(\mathbf{u}) = \int \rho(\mathbf{r}) \rho(\mathbf{r} + \mathbf{u}) d^3 \mathbf{r}$$

$$= \rho(u) * \rho(-u) \quad (\text{II-28})$$

where  $P(u)$  is called the Patterson function. The " \* " in equation (II-28) denotes the convolution operator. The Patterson function is thus the autocorrelation of the electron density function.

Substituting  $P(u)$  into (II-27) and letting  $u \rightarrow r$  (for consistency) yields:

$$I(\mathbf{q}) = \int P(\mathbf{r}) \exp[2\pi i \mathbf{q} \cdot \mathbf{r}] d^3 \mathbf{r} \quad (\text{II-29})$$

Equation (II-29) states that the intensity function is proportional to the Fourier transform of the Patterson function. Inversely, the Fourier transform of the intensity function is proportional to the Patterson function (equation 30).

$$P(\mathbf{r}) = \int I(\mathbf{q}) \exp[-2\pi i \mathbf{q} \cdot \mathbf{r}] d^3 \mathbf{q} \quad (\text{II-30})$$

The projection of a three dimension electron density distribution onto a two-dimensional electron density distribution is given by equation (II-31). The electron density distribution is said to be projected onto the  $y$ - $z$  plane.

$$\rho(y, z) = \int \rho(\mathbf{r}) dx \quad (\text{II-31})$$

Substituting equation (II-25) into (II-31) yields:

$$\rho(y, z) = \int \left[ \int F(\mathbf{q}) \exp[-2\pi i (q_x x + q_y y + q_z z)] d^3 \mathbf{q} \right] dx$$

Rearranging the integrand



$$\rho(y,z) = \int F(q) \exp[-2\pi i(q_y y + q_z z)] * \left[ \int \exp[-2\pi i q_x x] dx \right] dq_x dq_y dq_z$$

and using the definition of the delta function

$$\delta(q_x) = \int \exp[-2\pi i q_x x] dx$$

we obtain:

$$\rho(y,z) = \int \left[ \int F(q) \exp[-2\pi i(q_y y + q_z z)] \delta(q_x) dq_x \right] * dq_y dq_z$$

Evaluating the integral over x yields equation (II-32).

$$\rho(y,z) = \int F(0, q_y, q_z) \exp[-2\pi i(q_y y + q_z z)] dq_y dq_z \quad (II-32)$$

Thus, the Fourier transform of the structure factor in the  $q_y$ - $q_z$  plane is just the projection of the electron density distribution onto the  $y$ - $z$  plane. From (II-32) we can directly write the inverse Fourier transform.

$$F(0, q_y, q_z) = \int \rho(y,z) \exp[2\pi i(q_y y + q_z z)] dy dz \quad (II-33)$$

The Fourier transform of the electron density distribution projected onto the  $y$ - $z$  plane is the structure factor in the  $q_x$ - $q_y$  plane.

The above procedure is applied a second time to calculate the  $F(0,0,q_z)$ . The two dimensional electron density distribution is projected onto the  $z$  axis by integrating along the  $y$  axis. The

resulting one dimensional electron density distribution is called the electron density profile  $\rho(z)$ .

$$\rho(z) = \int \rho(y,z) dy \quad (\text{II-34})$$

Substituting equation (II-32) yields:

$$\rho(z) = \int \left[ \int F(0, q_y, q_z) \exp[-2\pi i(q_y y + q_z z)] \times \right. \\ \left. dq_y dq_z \right] dy$$

Rearranging the equation and substituting for the delta function.

$$\rho(z) = \int F(0, q_y, q_z) \exp[-2\pi i q_z z] \times \\ \left[ \int \exp[-2\pi i q_y y] dy \right] dq_y dq_z \\ = \int F(0, q_y, q_z) \exp[-2\pi i q_z z] \delta(q_y) dq_y dq_z$$

Integrating over  $y$  yields:

$$\rho(z) = \int F(0, 0, q_z) \exp[-2\pi i q_z z] dq_z \quad (\text{II-35})$$

Thus, the electron density profile is the Fourier transform of the structure factor along  $q_z$ . Consequently, the inverse Fourier transform yields:

$$F(0, 0, q_z) = \int \rho(z) \exp[2\pi i q_z z] dz \quad (\text{II-36})$$

$F(0,0,q_z)$  is commonly also referred as  $F(0,0,s)$  or  $F(0,0,q_\perp)$ . For simplicity let us replace  $F(0,0,q_z)$  with  $F(q_z)$  with the understanding that  $F(q_z)$  is not analogous to  $\rho(z)$  (in as much as  $\rho(z)$  is a projection of a three-dimensional distribution onto the  $z$ -axis), but merely represents the structure factor along the  $q_z$ -axis.

Rewriting equations (II-35), (II-36) and extending the above formalism to equations (II-29), (II-30), (II-26), (II-28) result in the basic equations of one-dimensional scattering theory (II-37), (II-38), (II-39), (II-40), (II-41), (II-42).

$$F(q_z) = \int \rho(z) \exp[2\pi i q_z z] dz \quad (\text{II-37})$$

$$\rho(z) = \int F(q_z) \exp[-2\pi i q_z z] dq_z \quad (\text{II-38})$$

$$I(q_z) = \int P(z) \exp[2\pi i q_z z] dz \quad (\text{II-39})$$

$$P(z) = \int I(q_z) \exp[-2\pi i q_z z] dq_z \quad (\text{II-40})$$

$$I(q_z) = F(q_z) F^*(q_z) \quad (\text{II-41})$$

$$P(z) = \rho(z) * \rho(-z) \quad (\text{II-42})$$

Since

$$2\pi q = k - k' \quad (\text{II-43})$$

and the magnitude of the incoming (incident) wave vector is the same as that of the outgoing (scattered) wave vector (i.e. elastic scattering):

$$k = k'$$

we can derive an expression for the magnitude of  $q$  where  $2\theta$  is the angle between the incident and scattered waves.

$$2\pi q = 2k \sin \theta \tag{II-44}$$

Given:

$$k = \frac{1}{\lambda}$$
$$= \frac{2\pi}{\lambda}$$

then  $|q|$  (in units of reciprocal length) is given by:

$$q = \frac{2 \sin \theta}{\lambda} \tag{II-45}$$

### Part III. Diffraction from Infinite Systems

Scattering from an electron density distribution (in the case of x-rays) which is composed of a repeating subunit (or unit cell) is known as diffraction. Diffraction maxima result from the constructive interference of particle waves scattered from the individual scattering centers. For a Bravais lattice with lattice vectors given by:

$$\mathbf{R} = n_1 \mathbf{a}_1 + n_2 \mathbf{a}_2 + n_3 \mathbf{a}_3 \quad (\text{II-46})$$

where  $\mathbf{a}_1, \mathbf{a}_2, \mathbf{a}_3$  are the primitive vectors of the Bravais lattice, and  $n_1, n_2, n_3$  are integers, the condition for constructive interference requires:

$$(\mathbf{k} - \mathbf{k}') \cdot \mathbf{R} = 2\pi m \quad (\text{II-47})$$

where  $m$  is an integer. This condition can be written in a more conventional form:

$$\exp[i(\mathbf{k} - \mathbf{k}') \cdot \mathbf{R}] = 1$$

The above expression is the von Laue formulation of diffraction by a crystal.

The reciprocal lattice vector is defined as:

$$\mathbf{Q} = k_1 \mathbf{b}_1 + k_2 \mathbf{b}_2 + k_3 \mathbf{b}_3 \quad (\text{II-48})$$

and  $\mathbf{b}_1, \mathbf{b}_2, \mathbf{b}_3$  are the primitive vectors of the reciprocal Bravais lattice and  $k_1, k_2, k_3$  are integers. The primitive vectors of the reciprocal lattice are defined in terms of the primitive vectors

$a_1, a_2, a_3$  as follows:

$$b_1 = \frac{a_2 \times a_3}{a_1 \cdot (a_2 \times a_3)} \quad (\text{II-49})$$

$$b_2 = \frac{a_3 \times a_1}{a_1 \cdot (a_2 \times a_3)} \quad (\text{II-50})$$

$$b_3 = \frac{a_1 \times a_2}{a_1 \cdot (a_2 \times a_3)} \quad (\text{II-51})$$

In addition:

$$a_i \cdot b_j = \delta_{ij} \quad (\text{II-52})$$

where  $\delta_{ij}$  is the Kronecker delta:

$$\delta_{ij} = 0 \quad i \neq j$$

$$\delta_{ij} = 1 \quad i = j$$

Diffraction can be easily visualized by a geometric construction known as Ewald's sphere of reflection (see figure 1). Let us define the origin in reciprocal space to be the point  $o$  and the reciprocal coordinate axes to be defined by the unit vectors  $\hat{s}_x, \hat{s}_y, \hat{s}_z$ . Construct a sphere of radius  $1/\lambda$  whose surface intersects the reciprocal origin and whose center is point  $c$ . This is Ewald's sphere. Let  $\vec{\tau}_0$  represents the incident wave given by  $k/2\pi$ . Our reciprocal lattice has coordinate axes defined by unit vectors  $\hat{q}_x, \hat{q}_y, \hat{q}_z$ ; its origin must coincide with point  $o$ .  $k/2\pi$  (the scattered vector) is represented by the vector  $\vec{\tau}_s$  where  $s$  must be a point on the surface of the Ewald's sphere if the scattering is elastic.  $q$  therefore is represented by the vector  $\vec{os}$ .

If  $q = Q$ , then the condition for constructive interference

(equation II-47) is fulfilled since (with II-43, II-48, II-52):

$$\begin{aligned}(\mathbf{k} - \mathbf{k}') \cdot \mathbf{R} &= 2\pi \mathbf{Q} \cdot \mathbf{R} \\ &= 2\pi(n_1 k_1 \mathbf{a}_1 \cdot \mathbf{b}_1 + n_2 k_2 \mathbf{a}_2 \cdot \mathbf{b}_2 \\ &\quad + n_3 k_3 \mathbf{a}_3 \cdot \mathbf{b}_3) \\ &= 2\pi(n_1 k_1 + n_2 k_2 + n_3 k_3) \\ &= 2\pi m\end{aligned}$$

$m$  must be an integer since  $n_1, n_2, n_3$  and  $k_1, k_2, k_3$  are integers. In other words, constructive interference from the lattice planes (in real space) perpendicular to the reciprocal lattice vector  $\mathbf{Q}$  requires the surface of Ewald's sphere to intersect the reciprocal lattice point defined by the reciprocal lattice vector  $\mathbf{Q}$ . These lattice planes are indexed by  $k_1, k_2, k_3$ , as is the reflection produced by the constructive interference.

Generally the reciprocal lattice points do not intersect the surface of Ewald's sphere for any  $q$ , and the condition for constructive interference is not met. For monochromatic light sources there are three options to overcome this problem. One can rotate Ewald's sphere (i.e. rotate the light source), rotate the reciprocal lattice (i.e. rotate the crystal), or rotate both the light source and the crystal. In practice, the second option is the most practical.

Consider the following electron density distribution for a one dimensional crystal of periodicity  $d$  in the  $z$  direction:

$$\rho(q_z) = \sum_{-\infty}^{+\infty} \delta(z - \ell d) \quad (\text{II-53})$$

Using equation (II-37) to yield (see appendix I):

$$F(q_z) = \sum_{-\infty}^{\infty} \delta(q_z - \frac{\ell}{d}) \quad (\text{II-54})$$

From the above expression,  $F(q_z) \neq 0$  if and only if  $q_z = \ell/d$ .

If we use equation (II-45), we have  $F(q_z) \neq 0$  if and only if:

$$\frac{2\sin\theta_\ell}{\lambda} = \ell \cdot \left[ \frac{1}{d} \right]$$

Thus we have a reciprocal lattice of periodicity  $1/d$ . The above expression can be rearranged to give Bragg's law in its usual form:

$$2d\sin\theta_\ell = \ell\lambda \quad (\text{II-55})$$

In terms of Ewald's sphere of reflection (figure 1) we need only consider the  $s_x$ - $s_z$  plane if we choose the incident beam in the  $s_x$  direction.  $\vec{\tau}$  thus lies along the  $s_x$  axis. We define the angle between  $\hat{s}_x$  and  $\hat{q}_x$  to be  $\omega$ . By rotating the crystal around the  $q_y$  axis we are able to intersect the reciprocal lattice points (located at  $\ell/d$ ) with Ewald's sphere at point  $s$ . This is a function of both  $\langle \cos$  and  $\omega$ .  $\langle \cos$  by definition is equal to  $2\theta$  (equation II-43). Since we are rotating only about the  $q_y$  axis, the angle between  $\hat{s}_z$  and  $\hat{q}_z$  is also  $\omega$ . Simple geometry leads us to conclude that  $\omega = \theta$ ;  $\omega$  and  $2\theta$  are said to be coupled (ie. they are not independent variables). This forms the basis of the so called  $\theta - 2\theta$  scan. For  $\omega = 0$  the only



reciprocal lattice point to intersect the surface of Ewald's sphere is the origin ( $\ell=0$ ); thus  $2\theta=0^\circ$ . The reciprocal lattice will intersect the surface of Ewald's sphere at the origin and at  $q_z=\ell/d$  if we rotate the crystal around the  $q_y$  axis until  $\omega=\omega_\ell$ ; this corresponds to  $2\theta_s = 2\theta_\ell$ .

We can instead use von Laue's formulation for diffraction from an infinite crystal to solve the problem of the one dimensional crystal aligned along the z axis. We start by constructing a simple three dimensional crystal and consider the reciprocal lattice vectors for  $k_1=k_2=0$  and  $k_3=\ell$ . Thus we choose to observe only the  $(00\ell)$  reflections. Let us begin by defining our Bravais lattice vector (equation II-46):

$$R = n_1 a_1 + n_2 a_2 + n_3 a_3$$

$$\text{where } a_1 = \hat{x}$$

$$a_2 = \hat{y}$$

$$a_3 = \hat{z}$$

$$\text{and } n_3 = d$$

thus

$$R = n_1 \hat{x} + n_2 \hat{y} + d \hat{z}$$

Equations (II-48) through (II-51) let us define our reciprocal lattice vector.

$$Q = \frac{\ell}{d} \hat{q}_z$$

For constructive interference to occur (ie.  $q = Q$ ) we have from equations (II-43) and (II-47):

$$2\pi R \cdot Q = 2\pi m \quad (m=\text{integer})$$

Substituting for Q and R, we conclude that  $l$  must be an integer.

With the help of equations (II-43) and (II-45) we again obtain Bragg's law:

$$\frac{2\sin\theta_l}{\lambda} = \frac{l}{d}$$

The reflection observed for:

$$\omega_l = \theta_l = \sin^{-1} \left[ \frac{l\lambda}{2d} \right]$$

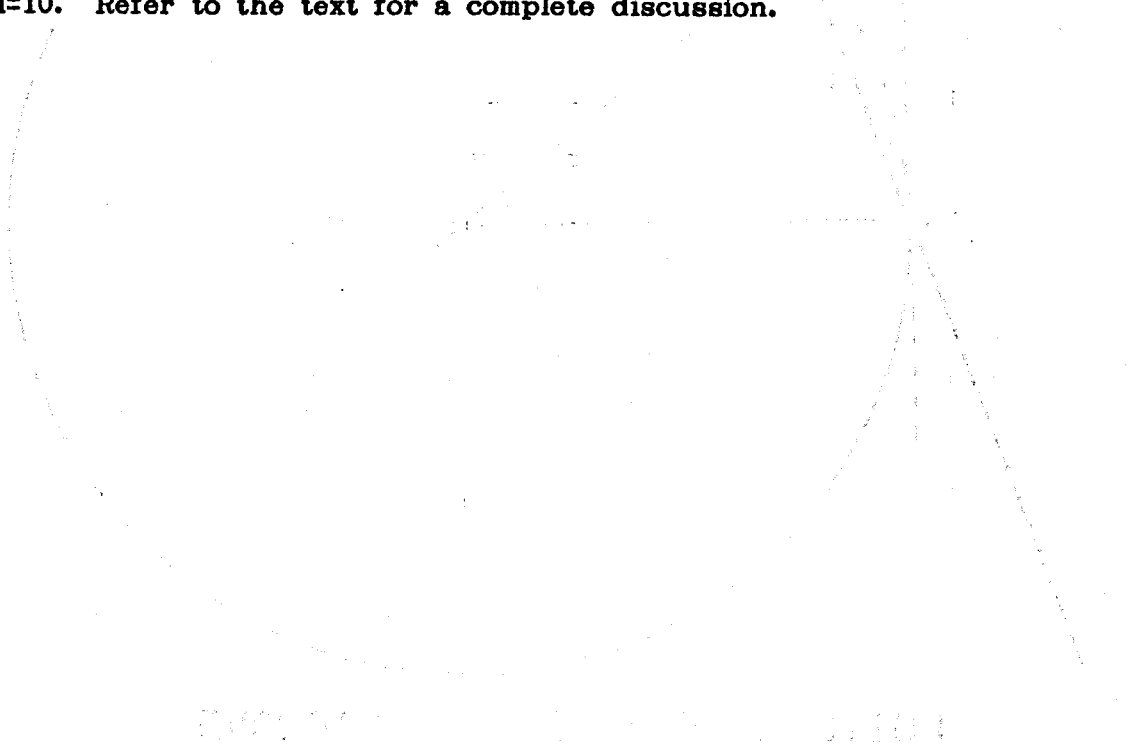
corresponding to

$$2\theta_l = 2\sin^{-1} \left[ \frac{l\lambda}{2d} \right]$$

arises from the constructive interference from the family of real space planes perpendicular to Q. Thus, constructive interference between the  $(00l)$  lattice planes, where the distance between the planes is  $d/l$ , gives rise to the  $(00l)$  reflection.

Figure 1

The intersection of Ewald's sphere of reflection with the  $\hat{s}_x-\hat{s}_z$  is shown. A one-dimensional reciprocal lattice along the  $\hat{q}_z$  is rotated by an angle  $\omega$  with respect to the  $\hat{s}_z$  axis, causing the  $l=10$  reciprocal lattice point to intersect the surface of the Ewald sphere. The von Laue conditions for constructive interference are thus satisfied for  $l=10$ . Refer to the text for a complete discussion.





#### Part IV. Diffraction from Finite Systems

The meridional intensity function for a multilayer composed of  $N$  repeated unit cells containing a bilayer with a unit cell translation vector along the  $z$  direction of magnitude  $d$  is given by the following equation:

$$I(q_z) = |F_{uc}(q_z)|^2 |L_n(q_z)|^2 * W(q_z) \quad (\text{II-56})$$

where

$$|L_n(q_z)|^2 = \sum_{l=-\infty}^{+\infty} \delta\left(q_z - \frac{l}{d}\right) * |B(q_z)|^2 \quad (\text{II-57})$$

and

$F_{uc}(q_z)$  = unit cell profile structure factor

$|L_n(q_z)|^2$  = the reciprocal lattice or interference function for the multilayer profile

$B(q_z)$  = Fourier transform of the multilayer profile box function

$W(q_z)$  = incident beam-shape function

The Fourier transform of equations (II-56) and (II-57) (using equation II-38) yields the multilayer profile Patterson function (equation II-58) (i.e. the multilayer profile autocorrelation function) and the multilayer profile lattice autocorrelation function respectively (equation II-59).

$$P_{m1}(z) = \left[ [\rho_{uc}(z) * \rho_{uc}(-z)] * \tilde{I}_n^2(z) \right] \cdot w(z) \quad (\text{II-58})$$

and

$$\tilde{l}_n^2(z) = \sum_{n=-\infty}^{+\infty} \delta(z-nd) \cdot \tilde{b}^2(z) \quad (\text{II-59})$$

where

$\rho_{uc}(z)$  = average unit cell electron density profile

$b(z)$  = multilayer profile box function

$w(z)$  = Fourier transform of the beam-shape function

and  $\tilde{l}_n^2(z)$  and  $\tilde{b}^2(z)$  represent the autocorrelation of  $l_n(z)$  and  $b(z)$  respectively.

For our multilayer composed of  $N$  repeated unit cells with its unit cell translation vector along the  $z$  direction of magnitude  $d$ :

$$\rho_{uc}(z) = 0 \text{ for } |z| > d/2$$

and

$$\begin{aligned} b(z) &= 1 \text{ for } -Nd/2 < z \leq Nd/2 \\ &= 0 \text{ otherwise} \end{aligned}$$

Substituting equation (II-42) into (II-58) yields:

$$P_{m1}(z) = \left[ \rho_{uc}(z) * \tilde{l}_n^2(z) \right] \cdot w(z) \quad (\text{II-60})$$

From the above definition of  $b(z)$  we can calculate  $|B(q_z)|^2$  to obtain:

$$|B(q_z)|^2 = \left[ \int_{-Nd/2}^{+Nd/2} \exp[2\pi i q_z z] dz \right]^2$$

$$\begin{aligned}
&= (Nd)^2 \left[ \frac{\sin \pi Nd q_z}{\pi Nd q_z} \right]^2 \\
&= (Nd)^2 \operatorname{sinc}^2(\pi Nd q_z)
\end{aligned}$$

The multilayer reciprocal lattice function  $|L_n(q_z)|^2$  (equation II-57) is therefore just the superposition of  $\operatorname{sinc}^2(\pi Nd q_z)$  placed at multiples of the reciprocal lattice vector  $1/d$ .  $|L_n(q_z)|^2$  has principal maxima at  $q_z = \ell/d$ . Between adjacent principal maxima  $|L_n(q_z)|^2$  has  $N-1$  local minima located at multiples of  $1/Nd$ , and  $N-2$  local (auxiliary or secondary) maxima located approximately half way between the local minima.

As the number of bilayers increases to large  $N$ , the Fourier transform of the multilayer profile box function  $[B(q_z)]$  approaches a Dirac delta function. The reciprocal lattice or interference function in turn approaches an infinite series of delta functions spaced at  $1/d$  along the  $q_z$ -axis. The intensity function (equation II-56) is then simply the modulus squared of the unit cell structure factor "sampled" at  $1/d$  along  $q_z$ , convoluted with the beam-shape function. This is simply the Bragg diffraction limit.

For reasonably finite  $N$  the intensity function is composed of diffraction maxima centered near the Bragg limit; the diffraction maxima may be shifted since the unit cell structure factor modulus squared is sampled by a superposition of  $\operatorname{sinc}^2(\pi Nd q_z)$  (appendix II). The intensity function may also contain distinct secondary maxima depending on  $N$  and  $W(q_z)$ . The diffraction maxima broaden as  $N$  decreases due to  $\operatorname{sinc}^2(\pi Nd q_z)$  as well.

As the number of bilayers decreases to  $N = 1$ , there is a corresponding broadening and shifting of the diffraction maxima, at which point  $I(q_z)$  is no longer sampled [ $|L_n(Qz)|^2 \rightarrow \text{constant}$ ] and the observed intensity represents the modulus squared of the unit cell or bilayer structure factor convoluted with the beam-shape function.

From the equation (II-60) it can be seen that  $P_{m1}(z)$  is pseudoperiodic in  $d$ , and decays to zero at  $|z| = Nd$ . This is not surprising since the multilayer autocorrelation function for a finite multilayer must of course also be finite. The finite size or extent of the multilayer is mathematically incorporated into the above formalism through  $b(z)$ . The Fourier transform of  $\tilde{b}^2(z)$  gives rise to the  $\text{sinc}^2$  in the multilayer interference function which broadens the principal maxima and is responsible for the appearance of secondary maxima in the intensity function. Sampling of the unit cell profile structure factor modulus squared by the  $\text{sinc}^2$  also shifts the diffraction maxima from the Bragg limit positions (appendix II).



## REFERENCES FOR CHAPTER TWO

- [2-1] Merzbacher, E., *Quantum Mechanics*, John Wiley and Sons, 1970.
- [2-2] Baym, G., *Lectures on Quantum Mechanics*, Benjamin/Cummings Publishing Company, 1978.
- [2-3] Hoseman, R., Bagchi, S.N., *Direct Analysis of Diffraction by Matter*, North-Holland Publishing Company, 1962.
- [2-4] Coley, J.M., *Diffraction Physics*, North-Holland Publishing Company, 1981.
- [2-5] Ashcroft, N.W., Mermin, N.D., *Solid State Physics*, Holt, Rinehart and Winston, 1976.

## CHAPTER THREE: SAMPLE PREPARATION AND X-RAY METHODS

### Part I. Multilayer Preparation

Multilayers samples were prepared by depositing successive monolayers of various carboxylic acids using the Langmuir-Blodgett technique [1-4] onto a flat glass substrate which was made hydrophobic by covalently binding an octadecyltrichlorosilane (OTS) monolayer to its surface [3-1]. The arachidic and myristic acids (Aldrich) had been zone refined with 50 zone passes at a rate of 1 cm/hr and the purity (>99.995%) of the center fraction confirmed by DSC measurements (Dupont 990). Triple distilled water was used in all stages of the preparation, including distillation over  $\text{KMnO}_4$  to remove organic contaminants.

The Lauda (Messgeräte-Werk, FRG) Langmuir system used for the deposition process consists of a trough having dimensions of 700 mm  $\times$  150 mm  $\times$  6 mm (*l,w,d*), a movable barrier perpendicular to the long-axis of the trough, a stationary barrier parallel to the movable barrier, a film balance, and electronics to drive the movable barrier, measure the surface pressure, and to monitor the temperature of the system. The stationary barrier separates the reference surface from the surface on which the monolayer of interest is spread (film surface). The monolayer is contained within the area defined by the two long axes of the trough and the stationary and movable barriers, with the maximum surface area of the film surface being  $\sim 560 \text{ cm}^2$ . The film balance measures the differential pressure on the stationary barrier. This differential pressure is the result of the net force

exerted on the stationary barrier by the reference and film surfaces. As a monolayer is compressed by the movable barrier, the differential pressure measured by the film balance increases. A feedback mechanism adjusts the position of the movable barrier to maintain a constant surface pressure during the deposition process.

Prior to deposition, the trough is clean with chloroform. After twenty minutes (ample time for all the chloroform to evaporate) the trough is filled with triple distilled water. The water surface between the barriers is first aspirated to remove any surface impurities, and then "compressed"; surface impurities result in a non-zero differential surface pressure measured between the reference surface and the film surface. Impurities resulting in pressures of  $< 1.0$  dyne/cm for a film surface of  $\sim 15$  cm<sup>2</sup> are acceptable.

The carboxylic acids used in this study are solubilised in chloroform [1mg/ml]. A monolayer ( $2.025 \times 10^{17}$  molecules) is spread upon the clean (*see above*) water surface between the stationary and movable barriers, and stabilized for three minutes to allow for the chloroform to evaporate. Routinely a pressure versus surface area isotherm of the carboxylic acid is measured to ascertain the purity of the carboxylic acid. The shape and collapse pressure of the isotherm are very reliable indicators as to the quality of the film. After the monolayer film collapses, the water surface is cleaned by aspiration and a second film is spread. After the film is stabilized and compressed to a given constant pressure, it is allowed to equilibrate

for twenty minutes.

Figure 2 shows the isotherms for arachidic acid  $[\text{CH}_3-(\text{CH}_2)_{18}-\text{COOH}]$  (bottom) and 10,12 pentacosadiynoic acid  $[\text{CH}_3-(\text{CH}_2)_{11}-\text{C}\equiv\text{C}-\text{C}\equiv\text{C}-(\text{CH}_2)_6-\text{COOH}]$  (top). These isotherms are characteristic of the two compounds, with 10,12 pentacosadiynoic acid [3-2] exhibiting a broad sigmoidal-like isotherm with a collapse pressure of 57 dyne/cm and the arachidic acid exhibiting a sharper curve with a collapse pressure of 61 dyne/cm.

The multilayers used in the first part of this study consist of a homologous series of arachidic acid multilayers. The arachidic acid monolayer was kept at a constant surface pressure of 20 dyne/cm and a temperature of 17.5°C during the deposition; the subphase was a 1mM  $\text{CdCl}_2$  solution of pH < 6.0. The substrate was dipped through the monolayer at a rate of 3.0 mm/min.

Since the OTS covered substrate is hydrophobic (due to the covalently attached alkane chains), a monolayer of arachidic acid is deposited onto the substrate surface as the substrate is lowered through the arachidic acid monolayer into the sub-phase. As the specimen (its surface now hydrophilic from the fatty acid carboxyl groups) is raised from the sub-phase through the arachidic acid monolayer, a second monolayer of fatty acid is deposited onto the substrate, leaving a hydrophobic surface. This process may be repeated several times to create a variable number N of arachidic acid bilayers. The multilayer specimens in this study consisted of one, two, three and five arachidic acid bilayers.

Two sets of multilayers were used in the second study. They were 1) finite sequences of arachidic acid (A) and myristic acid [ $\text{CH}_3-(\text{CH}_2)_{12}-\text{COOH}$ ] (M) monolayers and 2) finite sequences of arachidic acid and 10,12 pentacosadiynoic acid (D) monolayers. The carboxylic acid monolayers were deposited at a temperature of 17.5°C at a constant surface pressure of 15 dyne/cm for the myristic acid and 20 dyne/cm for the arachidic acid and the 10,12 pentacosadiynoic acid; the subphase was a 1 mM  $\text{CdCl}_2$  solution of pH < 6.0.

The first set of multilayers consist of two arachidic acid monolayers deposited onto the glass-OTS substrate followed by the deposition of either a) two arachidic acid monolayers to yield two arachidic acid bilayers (AAAA), b) one arachidic acid monolayer followed by a myristic acid monolayer to yield three arachidic acid monolayers and one myristic acid monolayer (AAAM), or c) two myristic acid monolayers to yield an arachidic acid bilayer followed by a myristic acid bilayer (AAMM).

The second set consists of a DDDA multilayer. The insert (upper right) in figure 2 shows partial isotherms for 10,12 pentacosadiynoic acid (left) and arachidic acid (right) for this deposition. After three monolayers of 10,12 pentacosadiynoic acid were deposited onto the glass-OTS substrate, the film surface was aspirated and cleaned, while the multilayer (glass-OTS substrate plus three monolayers of 10,12 pentacosadiynoic acid) were below the film surface. A monolayer of arachidic acid was then spread onto the water surface and equilibrated. As the multilayer was raised from beneath the

surface the final arachidic acid monolayer was deposited onto the multilayer.

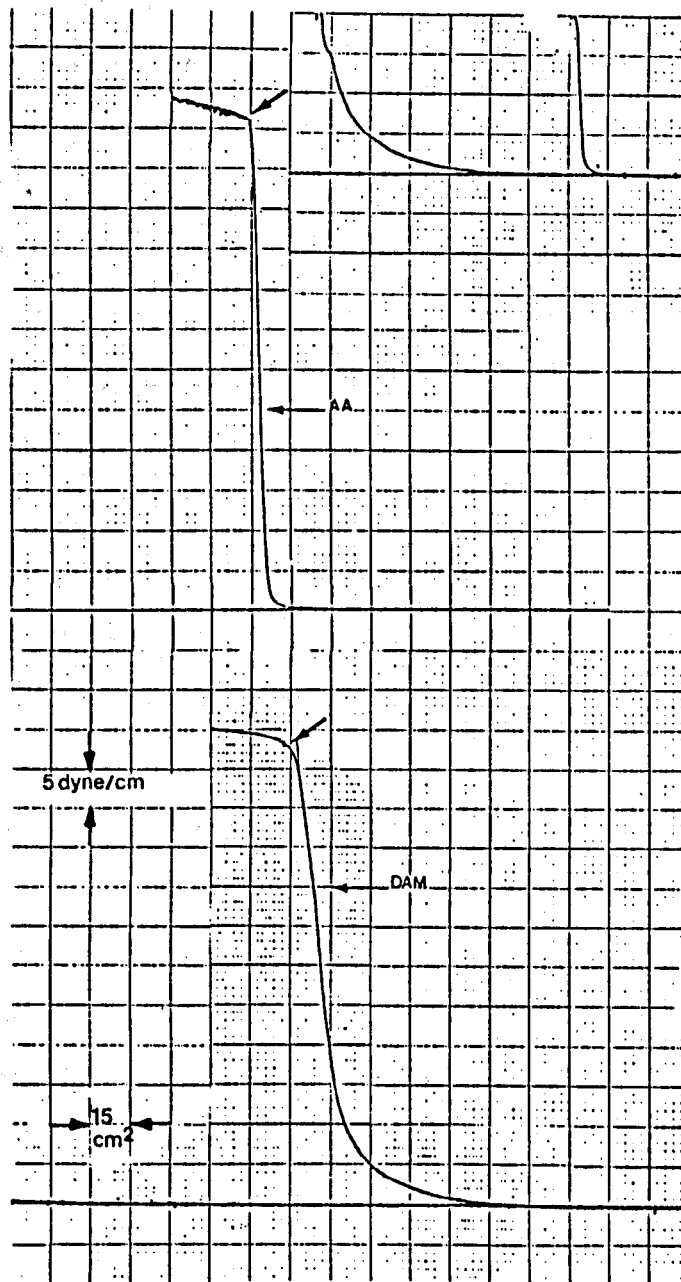
Following deposition the 10,12 pentacosadiynoic acid monolayers in the DDDA multilayer were polymerized with uv light to form diacetylene polymer (the polyene polymer chains being perpendicular to the monomer hydrocarbon chains) [3-2, 3-3].

After data was collected on the DDDA multilayer it was washed for three minutes in 10 mM NaOH to remove the surface arachidic acid monolayer. The resulting DDD multilayer was then further studied.

Figure 2

Isotherms for arachidic acid  $[\text{CH}_3-(\text{CH}_2)_{18}-\text{COOH}]$  (top) and 10,12 pentacosadiynoic acid  $[\text{CH}_3-(\text{CH}_2)_{11}-\text{C}\equiv\text{C}-\text{C}\equiv\text{C}-(\text{CH}_2)_8-\text{COOH}]$  (bottom) are shown. The pressure where each film collapsed is indicated by the diagonal arrows at the top of each isotherm. The insert shows partial isotherms of 10,12 pentacosadiynoic acid (left) and arachidic acid (right) obtained during the deposition of the DDDA multilayer.

Figure 2



ISOTHERMS  
ARACHIDIC AND PENTACOSADIYNOIC ACID



## Part II. X-Ray Diffraction Methods

Meridional x-ray diffraction was observed as a function of  $q_z$  [ $|q_z| = (2\sin\theta)/\lambda$ ] (II-45) corresponding to elastic momentum transfers parallel to the z-axis perpendicular to the substrate plane. The incident x-ray beam defines an angle  $\omega$  with the substrate plane (x-y).

The multilayers were positioned on the  $\omega$  axis of a two-axis diffractometer with a low impedance, position-sensitive linear detector (PSD) [3-4, 3-5] mounted on the  $2\theta$  axis. The linear detector was aligned along the  $q_z$  direction. An Elliott GX-6 rotating anode x-ray generator was used to produce CuK x-rays at a target loading of  $\sim 2.5$  KW/mm<sup>2</sup>. Nickel filters were used to select the CuK $\alpha$  line ( $\lambda=1.54$  A) which was line focused parallel to the multilayer plane with Frank's optics [3-6, 3-7]. X-ray beam width and the PSD system resolution result in a  $\Delta q_z$  resolution of  $\sim .003\text{\AA}^{-1}$ . The full beam line height (3 mm) was accepted by the PSD over the entire  $q_z$  range for the multilayer specimens investigated due to their small mosaic spread (see below).

Specimens were kept at room temperature (23-25°C) and at a relative humidity of  $< 0.1\%$  in a sealed canister. Helium paths with thin aluminum foil windows were used to reduce air scattering along the incident and scattered beam paths.

Omega scans ( $\Delta\omega = .02^\circ$ ) consisting of two minute exposures per omega value were done on each specimen over an omega range from  $\sim .5$  to  $6.5$  degrees. Each full scan took approximately 10 hours and

was controlled by a Digital Equipment Corporation PDP 11/24 computer. The sum of these exposures form a composite pattern which represents the meridional intensity function  $I(0,0,q_z)$ . As the value of omega is decreased below  $\sim 0.8^\circ$ , specular scattering due to the glass-OTS surface predominates and begins to saturate the detector. Scattering in this region of momentum transfer space arises only from the substrate and the interference between arachidic acid bilayers and the substrate. Due to this intense specular scattering from the substrate, the intensity functions were truncated for  $q_z < \sim 0.01\text{\AA}^{-1}$ . Thus the electron density profiles derived represent relative and not absolute electron densities.

A plot of the integrated intensity of a diffraction maximum at  $q_z \sim \ell/d$ , where  $\ell$  is an integer and  $d$  is the average periodicity in Angstroms of the multilayer projected onto the z-axis, versus omega gives a "rocking curve" for diffraction maximum  $\ell$  whose FWHM is a measure of the mosaic spread of the multilayer. Rocking curves for  $\ell = 1, 2, 3$  for  $N=5$  and  $\ell = 2, 3$  for  $N=1$  are shown in figure 3, where  $N$  refers to the number of arachidic acid bilayers in the multilayer. The rocking curve for the first maximum for  $N=1$  could not be measured as accurately since the specular scattering contributes considerable intensity in the region of momentum transfer space  $q_z \sim 1/d$  for this multilayer.

Each rocking curve is a composite of a strong, narrow feature at  $\omega=\theta_n$  for diffraction maxima  $\ell$  centered on a weak, broad feature extending over  $0^\circ \leq \omega \leq 2\theta_n$ . The measured mosaic spread for the narrow

feature in each rocking curve is  $\sim 0.13^\circ$  and is  $\sim 1.50^\circ$  for the broad feature. The narrow features in the rocking curves are most likely due to the well-oriented domains of the multilayers and the broad features are probably a result of misoriented components. The relative contribution of oriented *versus* misoriented domains in the multilayers remain fairly constant for  $N=1$  to 5. The measured mosaic spread of the specular scattering from a OTS-glass substrate alone is  $\sim 0.08^\circ$  since the beam is focused along  $q_z$  at the face of the detector. Hence, beam convergence at the specimen contributes to the measured mosaic spread of the multilayers.

As mentioned above, specular scattering due to the OTS-glass substrate predominates the meridional intensity function at  $q_z \leq \sim 0.02\text{\AA}^{-1}$ . It is possible to fit the intensity function derived from an OTS-glass sample with two exponentials over the range of  $q_z$  utilized in these studies. A quickly decaying exponential can be fit to the very low angle OTS-glass specular scattering, while a slowly decaying exponential function can be fit to the higher angle part of the intensity function to correct for substrate background scattering (figure 4). Similar exponentials were used to correct the meridional intensity functions of the one, two, three and five bilayer multilayer specimens. The first observable diffraction maxima of the intensity function for the one bilayer specimen appears as a shoulder at  $q_z \sim 0.02\text{\AA}^{-1}$  on the more intense specular scattering at smaller  $q_z$ . This shoulder can be resolved by subtracting the quickly decaying exponential of the specular scattering from the intensity function of

the one bilayer sample. The intensity functions for the two, three and five bilayer samples exhibit a much better resolved first order diffraction maximum. This occurs since the contribution to the intensity function from the multilayer increases quadratically with the number of bilayers, while the contribution from the specular scattering stays nearly the same. This background scattering correction causes unavoidable errors in determining the relative magnitude and shape of the first diffraction maximum especially for the one bilayer specimen. Data from one bilayer samples collected with a SIT two-dimensional detector [3-8, 3-9] using synchrotron radiation aided in the background scattering correction for the one bilayer data due to the very different two-dimensional shapes of the diffraction maxima observed from the specimen and the specular scattering from the substrate.

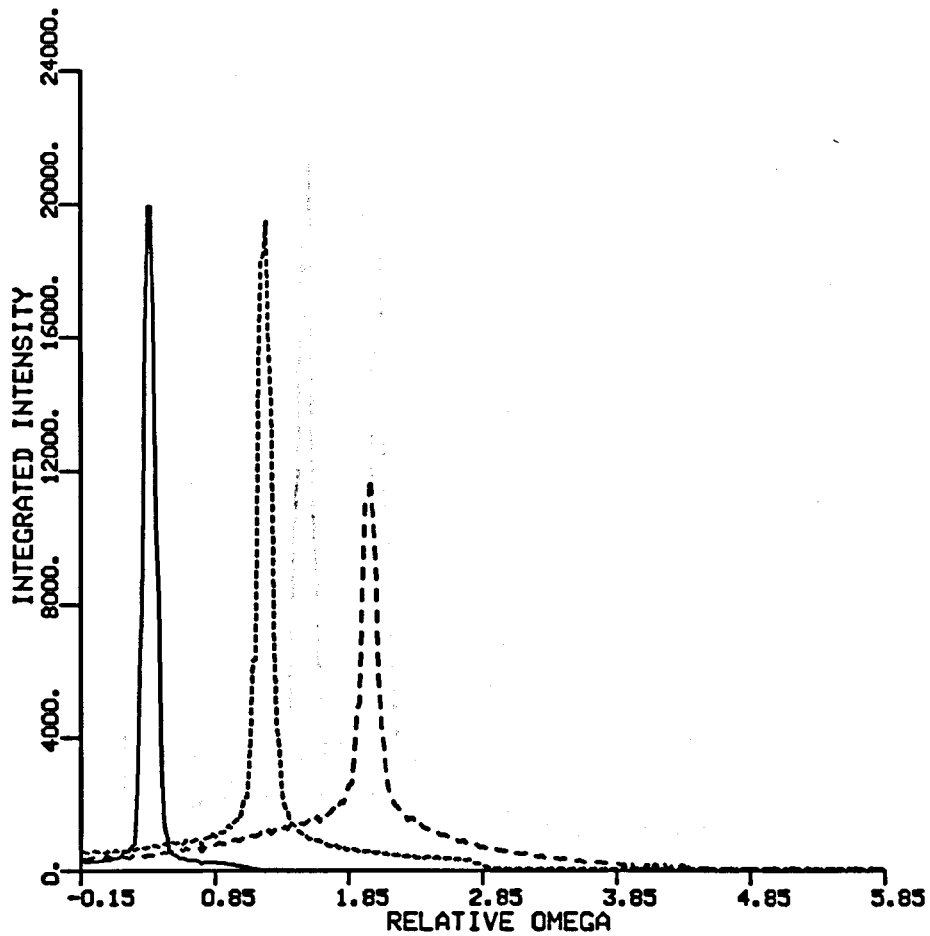
A Lorentz correction of  $q_z$  was applied to the intensity function to correct for the oscillation of the multilayer in the  $\omega$ -scan [2-3]. Since the specimens have a thickness ranging between  $\sim 50\text{\AA}$  and  $300\text{\AA}$ , no absorption correction is required for the  $\omega$  range used. The  $q_z$  Lorentz correction fixes the origin in momentum transfer space, errors in which will change the relative magnitudes of the diffraction maxima in the corrected intensity function,  $I_o(q_z)$ . For the two, three and five bilayer data sets, a plot of the diffraction order number versus the center of mass of the meridional diffraction maximum in channels gives a reasonable first estimate of the origin as the x-intercept, while a good approximation of the average



Figure 3A and 3B

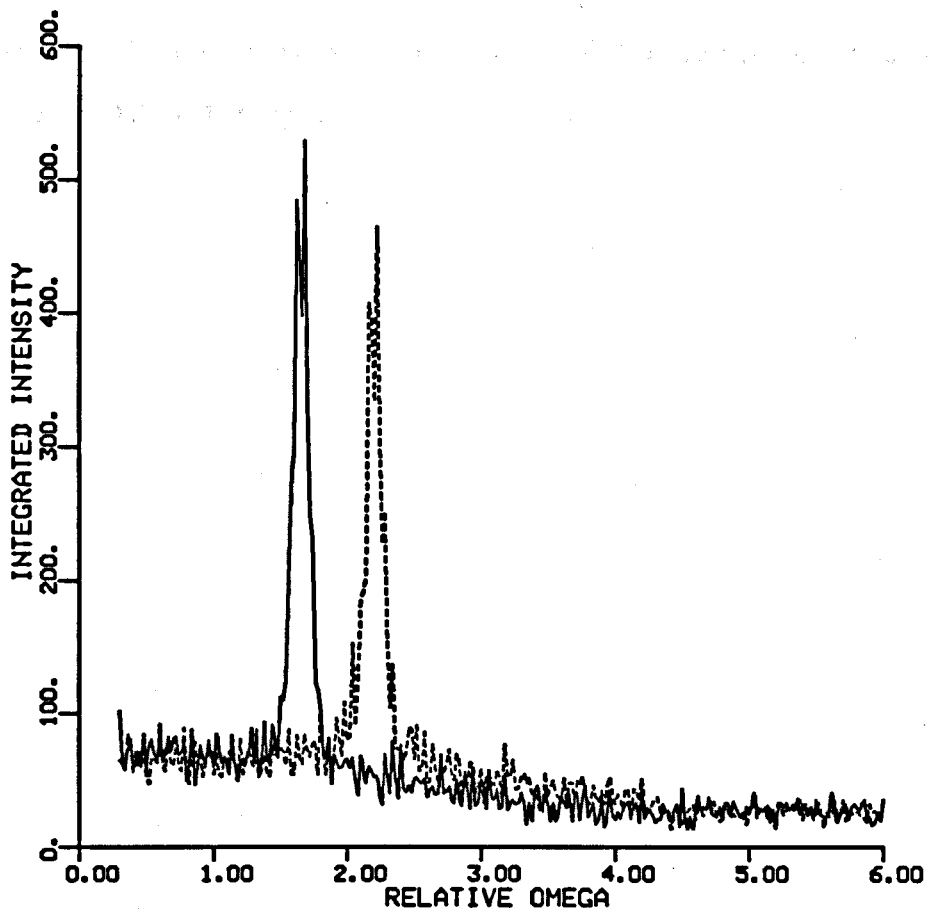
The rocking curves for the five bilayer multilayer are shown in figure 3A with the solid line the rocking curve for  $t=1$  (attenuated by a factor of 10), the dotted line the rocking curve for  $t=2$ , and the dashed line the rocking curve for  $t=3$ . The rocking curves for the one bilayer multilayer are shown in figure 3B with the dotted line the rocking curve for  $t=2$  and the dashed line the rocking curve for  $t=3$ .

Figure 3A



ROCKING CURVE N=5  
l=1 (\*0.10); l=2; l=3

Figure 3B



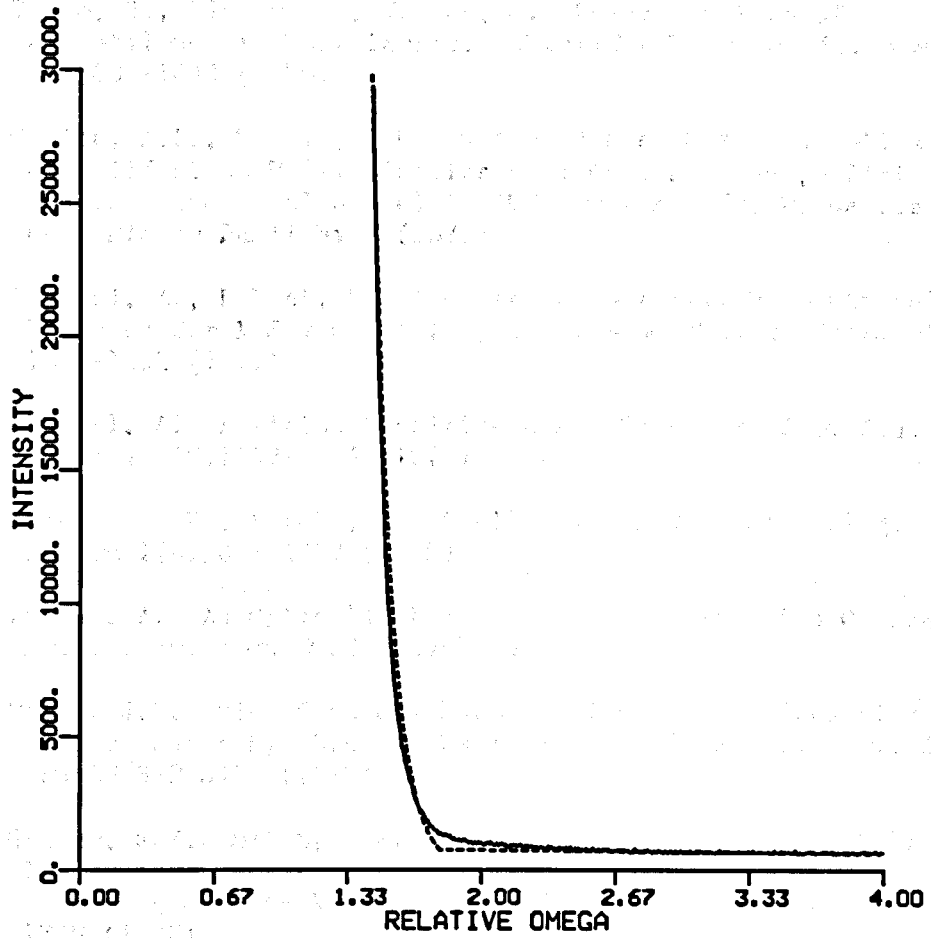
ROCKING CURVE N=1  
1=2 and 1=3



Figure 4

The solid line shows the OTS-scattering observed as a function of relative  $\omega$ , fitted with two exponential functions (dotted line). For  $\omega < \sim 0.2^\circ$  scattering from the OTS-glass substrate exceeds  $10^4$  cps. The detector is count rate limited and begins saturate at a count rate above  $\sim 1.5 \times 10^4$  cps.

Figure 4



OTS SCATTERING  
with exponential fit

### REFERENCES FOR CHAPTER THREE

- [3-1] Sagiv, J. Organized Monolayers by Adsorption. 1. Formation and Structure of Oleophobic Mixed Monolayers on Solid Surfaces. *JACS.* 102:92-98 (1980)
- [3-2] Tieke, B., Lieser, G., Wegner, G. Polymerization of Diacetylenes in Multilayers. *Journal of Polymer Science.* 17:1631-1644 (1979)
- [3-3] Garito, A.F., McGhie, A.R., Kalyanaraman, P.S. Kinetics of Solid State Polymerization of 2,4-Hexadiyne-1,6-Diol-Bis (P-Toluene Sulfonate) in *Molecular Metals*, W. Hatfield, ed., Plenum Publishing (1979)
- [3-4] Gabriel, A., DuPont, Y. A Position Sensitive Proportional Detector for X-Ray Crystallography. *Rev. Sci. Instrum.* 43: 1600-1602 (1972)
- [3-5] Gabriel, A. Position Sensitive X-Ray Detector. *Rev. Sci. Instrum.* 48:1303-1305 (1977)
- [3-6] Ehrenberg, W., Franks, A. Small-Angle X-Ray Scattering. *Nature* 170:1076-1077 (1952)
- [3-7] Franks, A. An Optically Focusing X-Ray Diffraction Camera. *Proc. Phys. Soc. B* 68:1054-1064 (1955)
- [3-8] Milch, J.R. Slow Scan SIT Detector for X-Ray Diffraction Studies Using Synchrotron Radiation. *IEEE Trans. Nucl. Sci.* NS-26:338-341 (1979)
- [3-9] Gruner, S.M., Milch, J.R., Reynolds, G.T. Slow-Scan Silicon-Intensified Target-TV X-Ray Detector for Quantitative Recording of Weak X-Ray Images. *Rev. Sci. Instrum.* 53:1770-1778 (1982)

## CHAPTER FOUR: RESULTS

### Part I. Arachidic Acid Multilayers

Figure 5 shows the corrected meridional intensity functions for the one, two, three and five bilayer arachidic acid specimens. Note that as the number of bilayers decreases the diffraction maxima broaden, until continuous diffraction is observed for  $N = 1$ . This broadening of the diffraction maxima are a direct result of  $B(q_z)$  (equation II-57) and consequently of  $b(z)$  (equation II-59). Also observe that as  $N$  decreases, diffraction maxima two and three, and diffraction maxima four and five, shift together. (Appendix II)

The Patterson or multilayer autocorrelation functions for the one, two, three, and five bilayer specimens are shown in figure 6. The Patterson function must also be sensitive to the total size or extent of the multilayer along the  $z$ -axis and to a first approximation are pseudoperiodic and decay nearly linearly to zero at  $z = \pm Nd$ . This property of  $P_{m1}(z)$  was used iteratively to refine the origin of  $I_0(q_z)$ . Oscillations in the Patterson functions for  $z \geq \pm Nd$  are a result of errors in determining the magnitude and shape of the first maximum in the corrected intensity functions and the truncation of the data for  $q_z < 0.01\text{\AA}^{-1}$  due to the intense specular scattering from the substrate in that region of reciprocal space.

As can be seen in the aforementioned figures the intensity and Patterson functions are very sensitive to the number  $N$  of bilayers in a given multilayer thin film for sufficiently small  $N$  relative to  $W(q_z)$ .

Figure 5

The Lorentz  $q_z$ -corrected, meridional intensity functions for one, two, three, and five bilayer arachidic acid multilayers (*from top to bottom*) are shown by the solid line. The first maxima of the corrected intensity functions have been scaled to unity. The dotted lines (for  $N = 1, 2, 3$ ) represent intensity functions calculated from the multilayer electron density profiles derived by the box refinement technique.

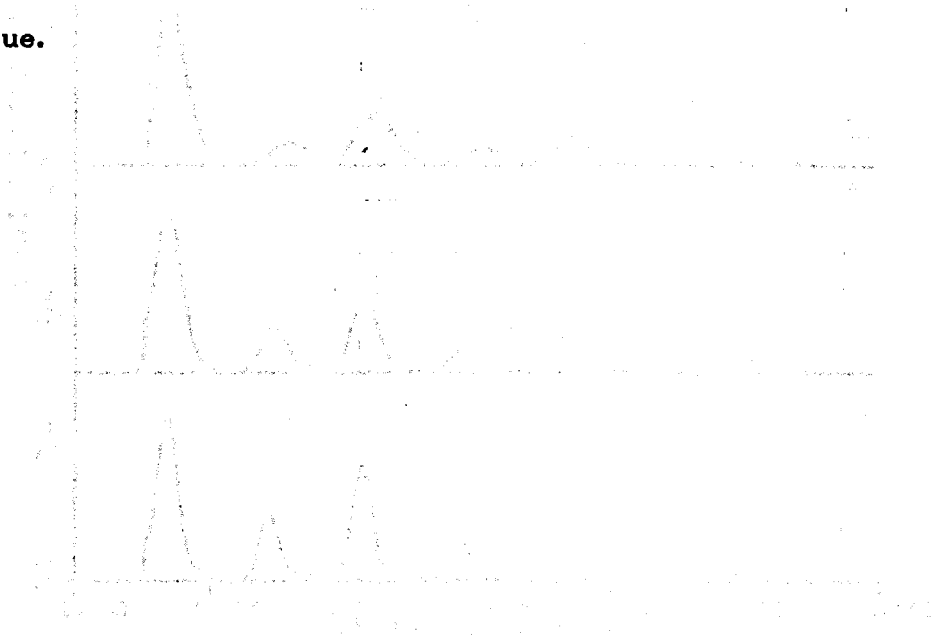
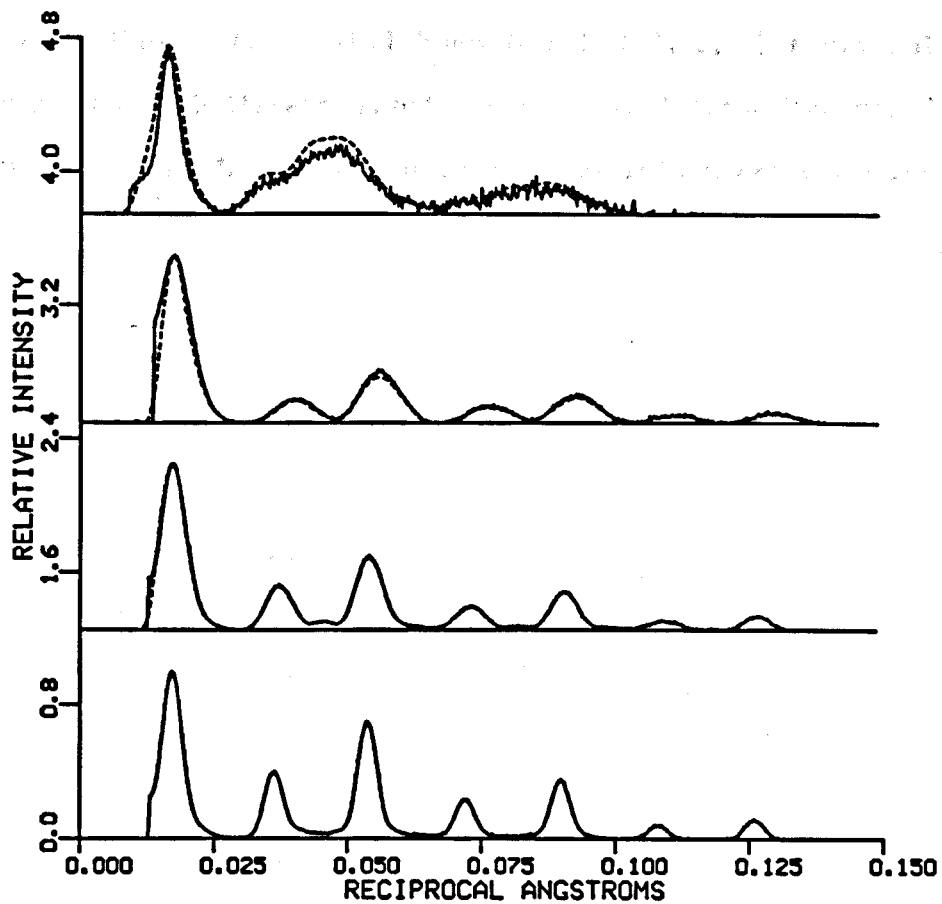


Figure 5



CORRECTED  $I(Q_z)$   
N=1, 2, 3, 5 arachidic acid bilayers

Figure 6

The multilayer profile Patterson functions for one, two, three, and five bilayer arachidic acid multilayers (*from top to bottom*) are shown by the solid lines. The dotted lines (for  $N = 1, 2, 3$ ) represent the multilayer profile Patterson functions calculated from the multilayer electron density profiles obtained by the box refinement procedure.

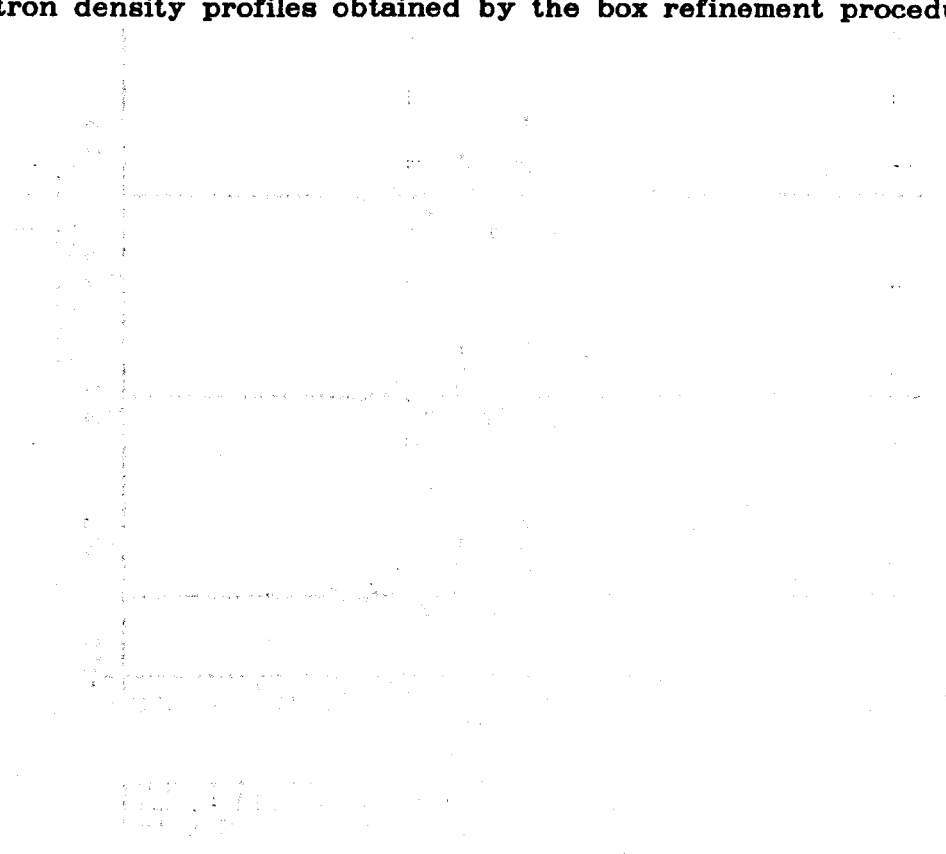
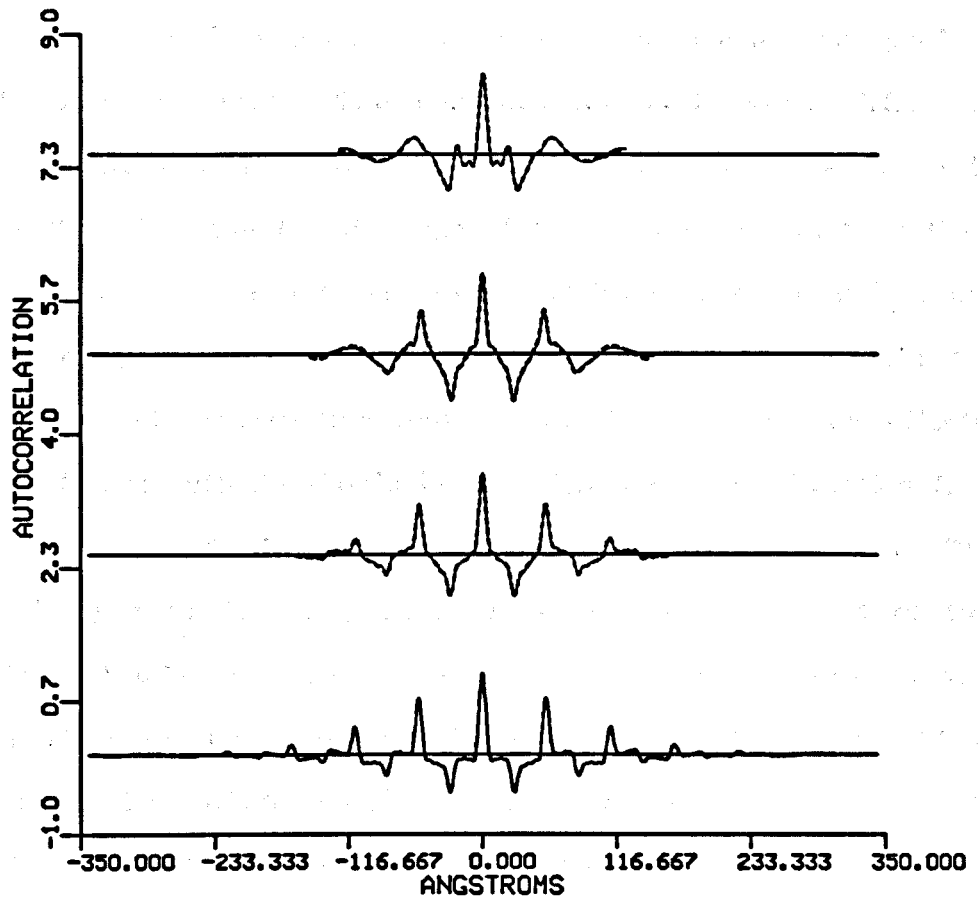


Figure 6



MULTILAYER PATTERNS  
N=1, 2, 3, 5 arachidic acid bilayers



## Part II. Arachidic Acid, Myristic Acid, and 10,12 Pentacosdiynoic Acid Mixed Multilayers

Figure 7 shows the corrected intensity functions for the AAAA, AAAM, and AAMM multilayer films. All the corrected intensity functions in figure 7 are indicative of asymmetric multilayer profiles of finite size or extent. The non-zero minima between diffraction maxima indicate that the profiles are asymmetric (see discussion in appendix V) while the broad shape of the maxima results from their finite extent. The meridional x-ray diffraction from multilayers composed of periodic sequences of monolayers should contain the most pronounced constructive and destructive interference effects. Such interference effects should be diminished in the diffraction from multilayers composed of non-periodic sequences of monolayers. The AAAA multilayer to first approximation is periodic composed of two arachidic acid bilayers; diffraction from the multilayer consequently contains stronger interference effects than the AAAM and AAMM multilayers. The AAAM multilayer corrected intensity function is similar to the AAAA multilayer corrected intensity function except for the somewhat lesser relative magnitudes of the diffraction maxima at higher  $q_z$ . The corrected intensity function for the AAMM multilayer differs considerably from the corrected intensity functions of the AAAM and AAAA multilayers with diffraction maxima of lesser relative magnitudes at higher  $q_z$  and less-defined diffraction minima.

Autocorrelation functions for the AAAA, AAAM, and AAMM multilayers are shown in figure 8. These typical multilayer profile

autocorrelation functions decay monotonically to essentially zero for  $z > z_{\max}$  which defines the extent of the multilayer profiles.  $z_{\max}$  was found to be 96A, 108A, and 116A for the AAMM, AAAM, and AAAA multilayers respectively. The multilayer autocorrelation functions contain small amplitude low-frequency oscillations around the zero-baseline for  $z > z_{\max}$  due to errors in the corrected intensity functions for  $q_z \leq \sim 0.02\text{\AA}^{-1}$ . These errors are a consequence of the background scattering correction.

The corrected intensity functions for the DDDA and DDD multilayer thin films are shown in figure 9. Since the DDDA multilayer to first approximation is composed of two bilayers, the corrected intensity function exhibits some of the features of a  $N=2$  diffraction pattern. One observes only scattering (ie. no interference) from the DDD multilayer since it is not composed of repeating unit cells. Note the absence of distinct zero-minima in the corrected intensity function for the DDD multilayer.

The multilayer autocorrelation functions for the DDDA and the DDD multilayers are shown in figure 10. The autocorrelation function calculated for the DDDA multilayer has pronounced positive correlations for  $z \sim z_{\max}$  ( $\sim 110\text{\AA}$ ) while the autocorrelation function calculated for the DDD multilayer has only negative correlations for  $z \sim z_{\max}$  (90A).

Figure 7

The background and Lorentz- $q_z$  corrected intensity functions for the AAMM (top), AAAM (middle), and AAAA (bottom) multilayers are shown. Due to the relatively low signal to noise ratio of the AAMM and AAAM intensity functions when compared to the AAAA intensity function, the AAMM and AAAM intensity functions were smoothed.

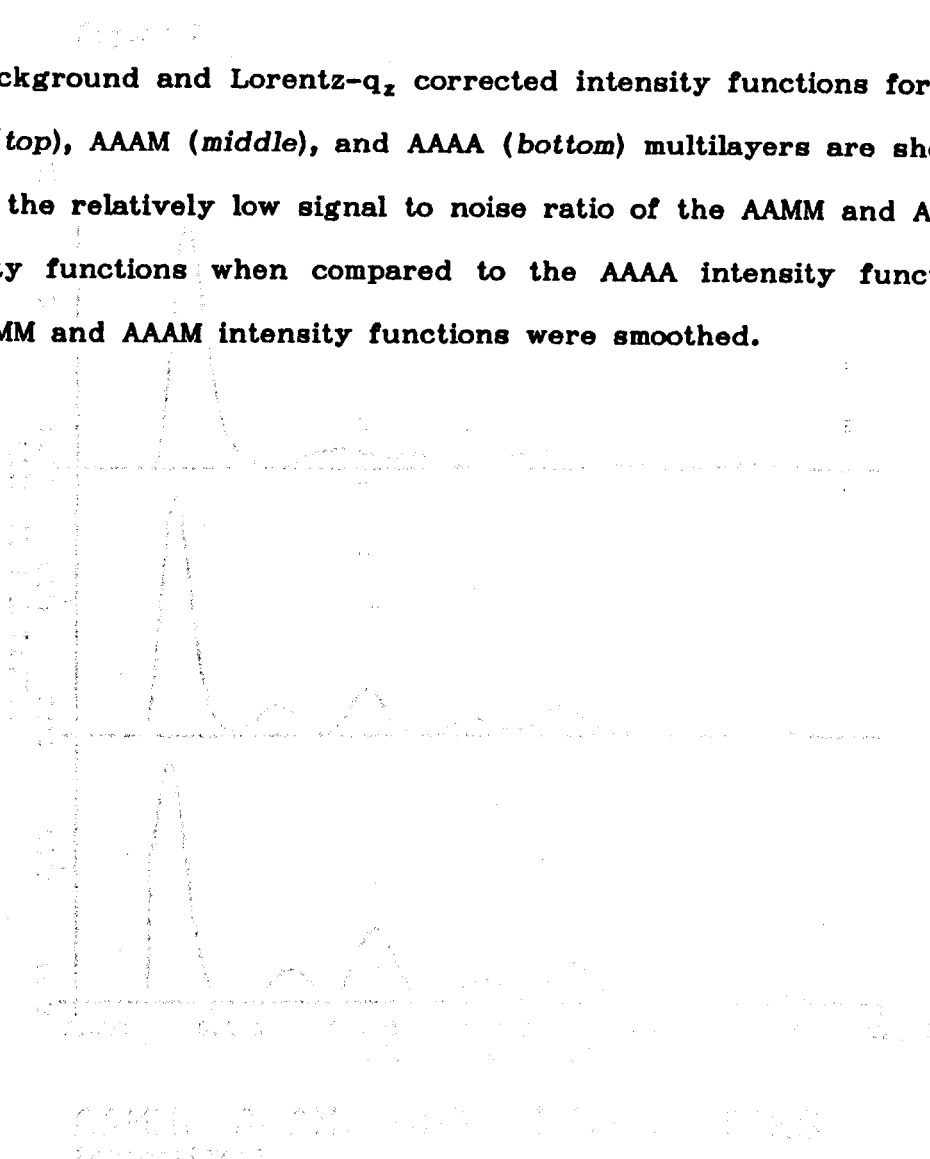
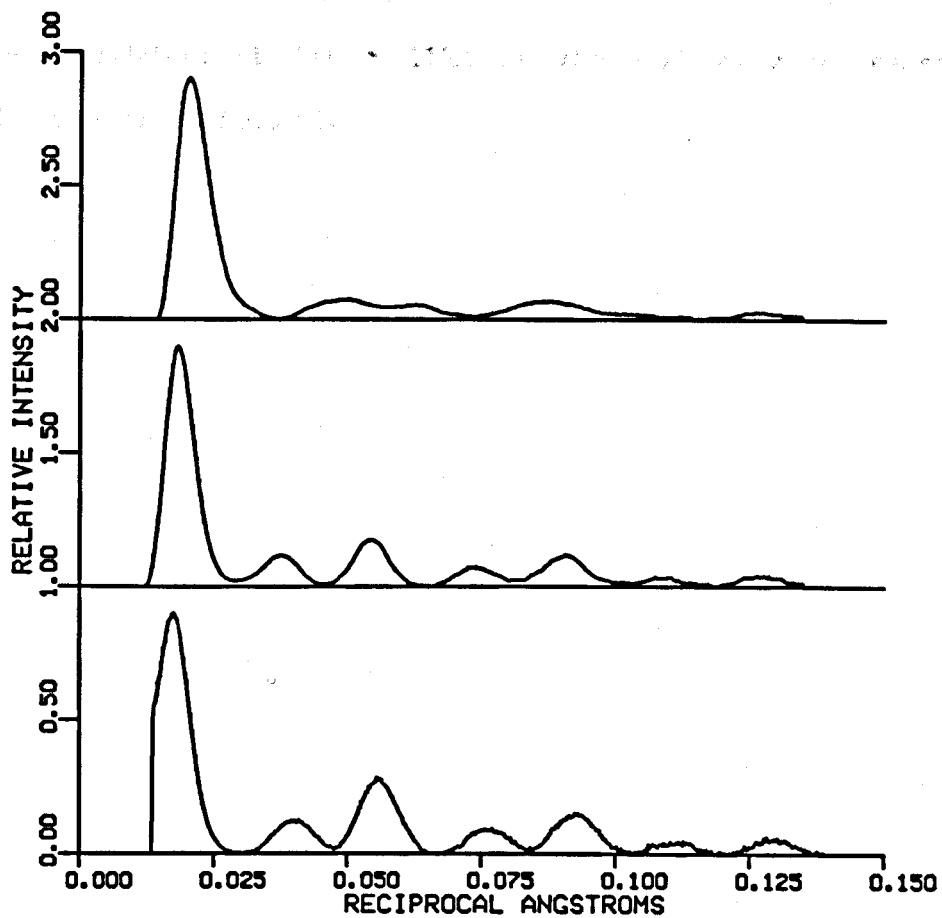


Figure 7



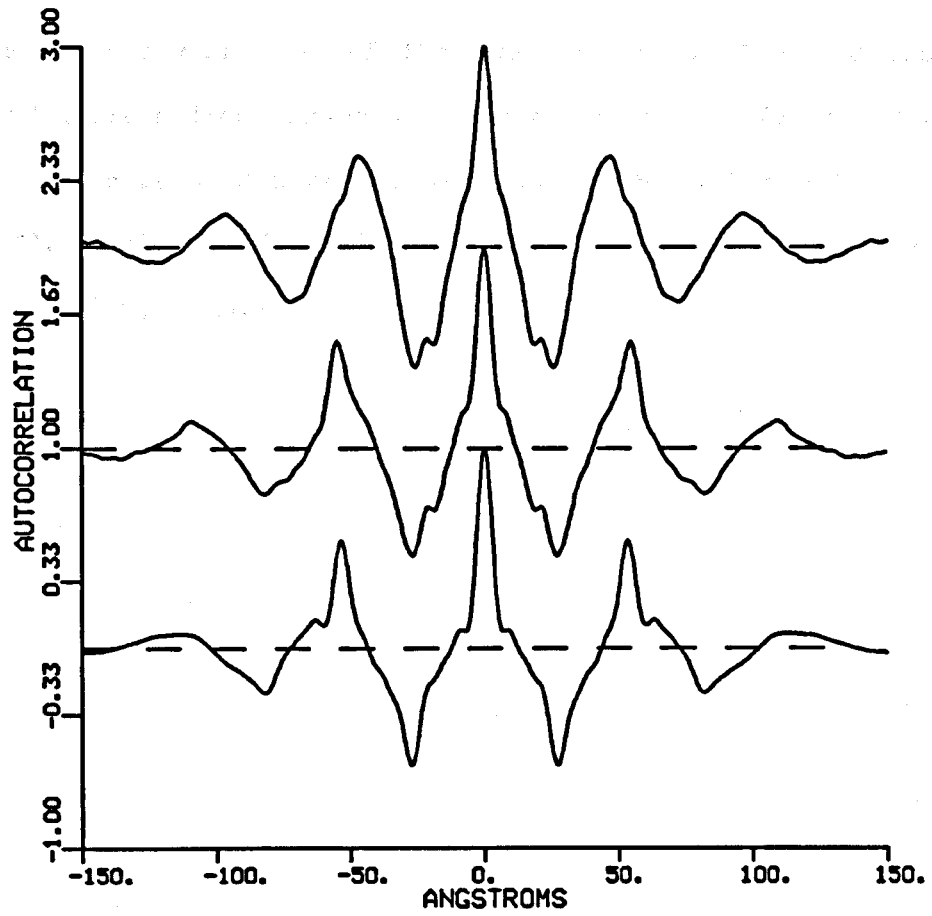
AAMM, AAAM, AAAA INTENSITIES  
(normalized)

**Figure 8**

The Patterson functions for the AAMM (*top*), AAAM (*middle*), and AAAA (*bottom*) multilayers. Note the shift to larger absolute  $z$  of the positive correlation at  $|z| \sim 110\text{\AA}$  as the multilayer increases in overall size (*top to bottom*).



Figure 8



AAMM, AAAM, AAAA MULTILAYER  
Patterson Functions

Figure 9

The corrected intensity functions for the DDDA multilayer (top) and the DDD multilayer (bottom) are shown. The scattering from the DDDA multilayer has some of the characteristics of the diffraction observed from a two bilayer multilayer for  $q_z < .075\text{\AA}^{-1}$ . Note in particular the zero or nearly zero minima between the maxima for  $q_z < .075\text{\AA}^{-1}$ . Scattering from the DDD multilayer is continuous over the full range of  $q_z$  measured.

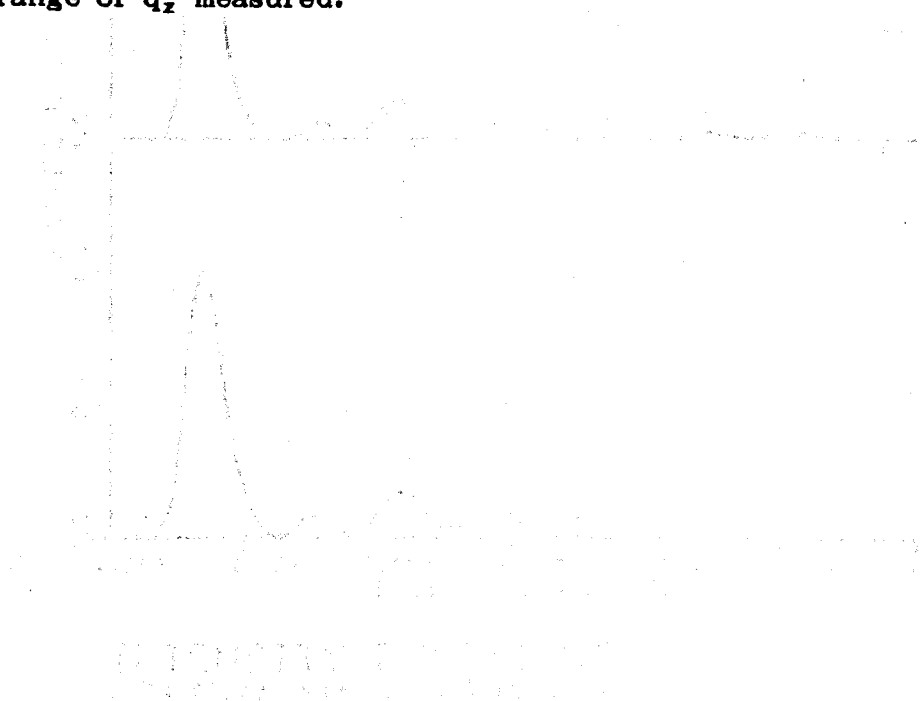
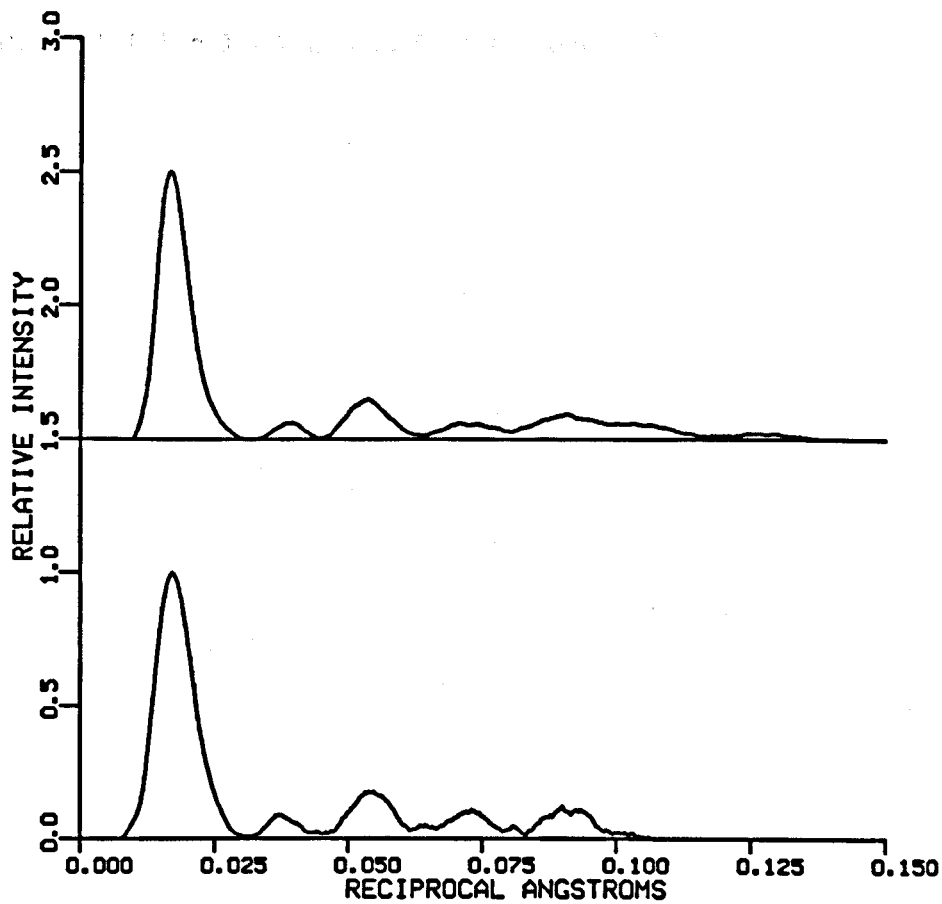


Figure 9



INTENSITY FUNCTIONS  
DDDA (top) versus DDD (bottom)



Figure 10

The Patterson functions for the DDDA (upper) and the DDD (lower) multilayers are compared. Note the disappearance of the positive correlation at  $|z| \sim 110\text{\AA}$  in the DDD Patterson function.

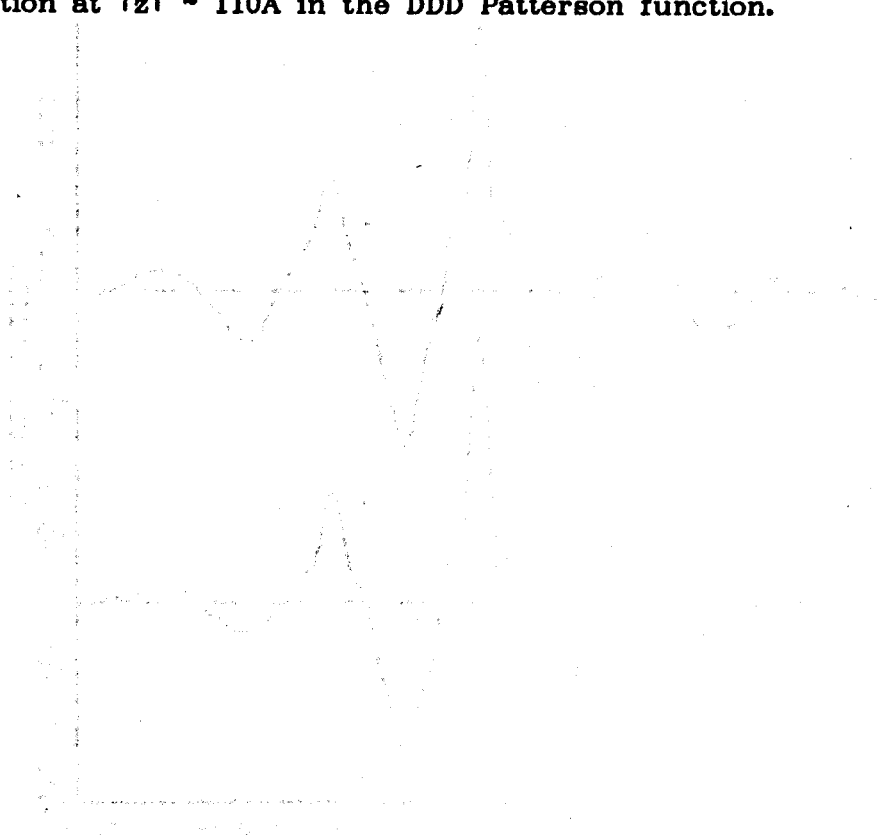
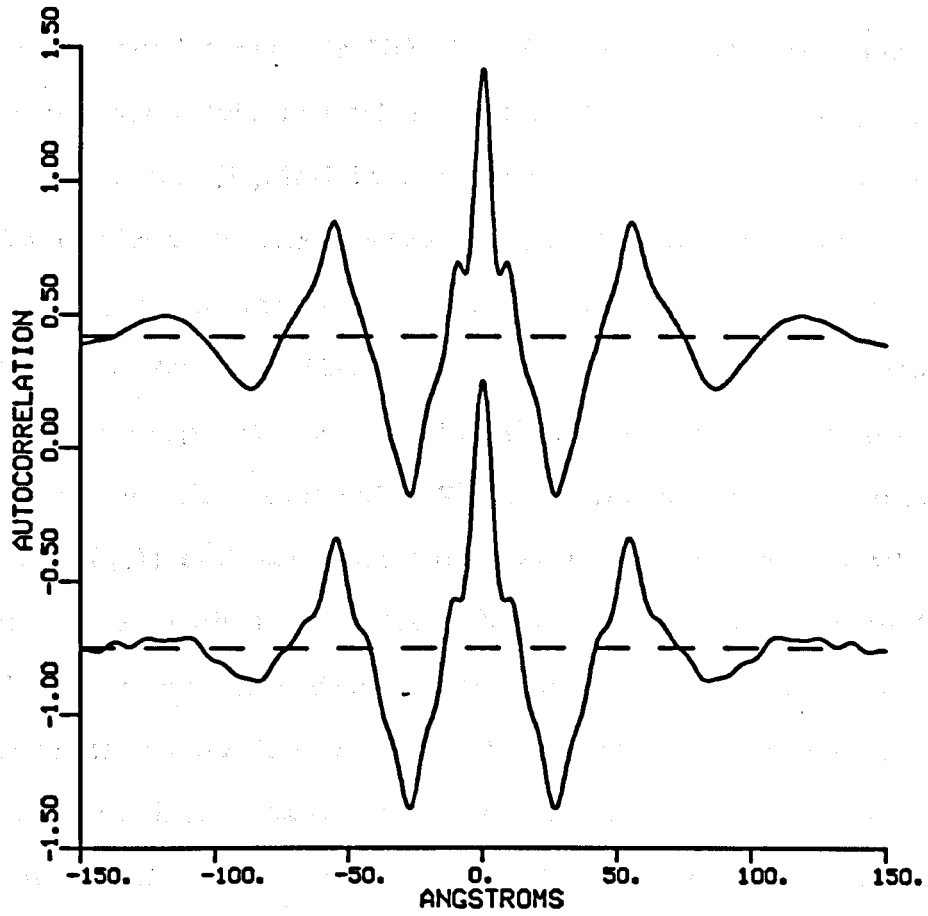


Figure 10



MULTILAYER PATTERNS  
DDDA (upper plot); DDD (lower plot)

## CHAPTER FIVE: ANALYSIS

### Part I. Arachidic Acid Multilayers

It is possible to uniquely reconstruct the unit cell Patterson  $[P_{uc}(z)]$  provided that the Patterson function for the multilayer profile is bounded (appendix III) [2-3, 5-1, 5-2]. If one assumes  $\rho_{uc}$  to be centrosymmetric around an origin [i.e.  $\rho_{uc}(z) = \rho_{uc}(-z)$ ] the unit cell Patterson  $[P_{uc}(z)]$  in turn can be deconvoluted uniquely to give the electron density profile  $[\rho_{uc}(z)]$  for the unit cell (or the average bilayer in the multilayer) by a recursive deconvolution method (appendix IV) [1-20, 2-3, 5-2]. Since the recursive deconvolution propagates errors, the final electron density profile is obtained by phasing (appendix V) the Lorentz-corrected intensity function  $[I_o(q_z)]$  and selecting the best phase combination which is most consistent with the electron density profile for the unit cell derived by the recursive deconvolution method.

Figure 11 shows the unit cell Patterson function for the two, three and five bilayer multilayers reconstructed from the multilayer Patterson function using the method of linear equations (appendix III). The linear equations were applied from  $0 < z < d$ .

Figure 12 shows the electron density profiles for the average bilayer for the two, three, and five bilayer multilayers derived by the unit cell Patterson recursive deconvolution outlined above. Errors in these profiles propagate from right to left; hence the asymmetry of the functions.

Figure 13 shows the electron density profiles for the average

bilayer for the two, three and five bilayer multilayers derived by the correctly phased Fourier synthesis (appendix V). All three rather typical electron density profiles exhibit a peak region of relatively high electron density for  $0.0 \leq |z| \leq 4.5\text{\AA}$  containing the  $-\text{COOH}$  polar headgroups, plateau regions of intermediate relative electron density near the mean for  $4.5\text{\AA} < |z| < 12.0\text{\AA}$  containing the hydrocarbon chain  $[-(\text{CH}_2)_{16}-]$  groups, and trough regions of relatively low electron density for  $21.0\text{\AA} < |z| < 29.5\text{\AA}$  containing the terminal methyl groups ( $-\text{CH}_3$ ). For these bilayers, the multilayer periodicity is the methyl group separation across the bilayer profile. Note the close similarity in detail of the profiles derived by recursive deconvolution and those derived by the correctly phased Fourier synthesis.

As  $N$  decreases, there is a corresponding decrease in the multilayer periodicity of the average bilayer profiles as evidenced by the decrease in the methyl group separation distance across the bilayer profile. For  $N = 5, 3, 2$ , the periodicities are  $55.9\text{\AA}$ ,  $54.4\text{\AA}$  and  $52.9\text{\AA}$  respectively. In addition to a decrease in multilayer periodicity, a broadening of the methyl trough regions into the neighboring hydrocarbon chain plateau regions and a subsequent decrease in the depth of the methyl trough regions are observed as the number of bilayers decreases. These changes in the hydrocarbon core region of the average bilayer profile with decreasing  $N$  are similar to those accompanying "kink" formation (time-average or ensemble average) in *all trans* hydrocarbon chains [5-3]. For

example, figure 14 shows the electron density profiles for a dipalmitoyl phosphatidylcholine (DPPC) bilayer at 35°C and 49°C, the former being below the phase transition temperature for chain melting of 41°C, the latter above. Note that within the hydrocarbon core regions of the profiles, the melted DPPC profile (dotted line) exhibits many of the features (due to the time-average "kink" formation in the fatty-acid chains) of the  $N = 2$  electron density profile of arachidic acid while the frozen DPPC profile displays the features (due to the *all trans* configuration of the fatty-acid chains) of the  $N = 5$  electron density profile of arachidic acid. In particular, note the similarly decreased average hydrocarbon chain length and broadened methyl trough features in both the melted DPPC and arachidic acid  $N = 2$  electron density profiles.

Assuming that the electron density profile for a bilayer structure is centrosymmetric and repeated  $N$  times in the multilayer profile becomes less valid as the number of bilayers in the multilayer thin film decreases. The fact that the background scattering corrected intensity function  $[I_o(q_z)]$  for  $N = 2$  and 3 (figure 5) is substantially non-zero between some adjacent diffraction maxima strongly suggests that the corresponding multilayer electron density profile may be asymmetric, inasmuch as the non-zero minima would disallow the phase of the structure factor to change at that value of  $q_z$  (see appendix V). A model for the multilayer electron density profile for  $N=2$  can be constructed by extending the electron density profile for the average bilayer (figure 13) to two bilayers (dotted line, figure

15). This centrosymmetric model for the multilayer profile yields the intensity function shown by the dotted line in figure 16. This figure shows the derived intensity function after convolution with the incident beam shape function,  $W(q_z)$ . The intensity function shows auxiliary maxima between major diffraction orders; convolution with  $W(q_z)$  suppresses the secondary maxima and introduces a non-zero "baseline" to the intensity function. Note, all the minima in the calculated intensity function for this centrosymmetric model are zero with respect to this baseline.

The direct Patterson function deconvolution method is limited in that it determines only the electron density profile of the average unit cell or bilayer in the multilayer. It cannot accommodate bilayer structures where the monolayer profile structures differ from one another; in particular, it cannot distinguish between the first monolayer on the alkylated substrate as compared to the last monolayer at the air interface. In general, it is impossible to phase asymmetric structures of infinite extent ( $N > 10$ , dependent on  $W(q_z)$ ) unless some special technique (e.g. isomorphous replacement) is employed. However, for finite systems (i.e. where the one-dimensional Fourier transform of the corrected intensity function  $[I_o(q_z)]$  gives a bounded multilayer Patterson function the box-refinement procedure (appendix VI) can be used to determine the multilayer electron density profile  $\rho_{m1}(z)$  [1-22].

This technique assumes a given phase for each point in  $q_z$  derived from the Fourier transform of some arbitrary "trial" function.

These phases are combined with the modulus of the multilayer structure factor  $|F_{m1}(q_z)|$  and Fourier transformed to give an initial electron density profile  $\rho_{m1}(z)$ . This electron density profile is in turn set to zero outside a box  $b(z)$  whose width is at least that of the multilayer profile. This truncated electron density profile becomes the new trial function and the process is repeated iteratively until the refinement converges. (As noted earlier, the intensity function, and thus  $|F_{m1}(q_z)|$  are sensitive to the finite extent of the sample. The broadening and shifting of the intensity maxima from the Bragg limit provide this information). The width of the box  $b(z)$  can be determined from the multilayer Patterson function;  $P_{m1}(z)$  must be zero for  $|z|$  larger than the maximum extent of  $\rho_{m1}(z)$  due to  $b(z)$ . It is the finite extent of the multilayers in  $z$  that provide the strong constraint needed for the box refinement technique to coverage to a solution for the multilayer profile  $\rho_{m1}(z)$ . The refinement continues until it has found a phase combination that will produce a multilayer electron density profile which is zero outside the box. Unfortunately there is no guarantee that the solution derived from the box refinement is unique; in fact, there are likely to be several "local" solutions that satisfy the box constraint [1-23]. The final solution may ultimately depend to some extent on the initial trial function. The trial function used in this analysis was the sum of a cosine and sine wave with a wavelength on the order of twice the total extent of the multilayer profile as derived from the multilayer Patterson function. Various other trial functions were also

tried (i.e. ramp functions of various sizes, pulse function of different widths) which refine to qualitatively similar multilayer profile structures.

The one, two and three bilayer multilayer systems were investigated with the box refinement technique. The three corrected intensity functions  $I_o(q_z)$  were refined to multilayer electron density profiles which exhibited features common to each multilayer electron density profile, as well as exhibited features common to each monolayer within the multilayer electron density profiles. Figure 17 shows the resulting multilayer electron density profiles (i.e. continuous profiles) for  $N = 1, 2, 3$  after twenty iterations from the box refinement technique. The figure also shows the trial function used in each refinement as well as the "box" used in applying the boundary constraint.

The continuous electron density profiles for the  $N = 3$  multilayer shows well-defined methyl troughs at  $z = 0A, 54A, 109A$ ; relatively flat hydrocarbon chain regions for  $-24A < z < -5A, 2A < z < 16A, 30A < z < 37A, 57A < z < 68A, 85A < z < 104A$ ; carboxyl peaks at  $z = -30A, 23A, 78A$ ; and a disordered, poorly defined methyl trough at  $z = 70A$ . The profile for  $N = 2$  shows well-defined methyl troughs at  $z = 0A$  and  $53A$ ; relatively flat hydrocarbon chains regions for  $-24A < z < -4A, 4A < z < 20A, 28A < z < 49A$ ; carboxyl groups at  $z = -29A$  and  $27A$ ; and a disordered methyl trough at  $z = 53A$ . Finally, the profile for  $N = 1$  shows a well-defined methyl trough at  $z = 0A$ ; a relatively flat hydrocarbon chain region for  $-5A < z < -26A$ ; a carboxyl group



at  $z = -31\text{\AA}$ ; and a disordered methyl trough at  $z = -57\text{\AA}$ . In general, a multilayer profile consisting of  $N$  arachidic acid bilayers exhibit  $N$  equally-spaced well-defined methyl troughs,  $N$  equally-spaced well-defined carboxyl peaks and one ill-defined and broad methyl trough at one end. The broadening of this trough causes the hydrocarbon chain region adjacent to the trough to become non-flat. The mean carboxyl-methyl trough distance is  $27\text{\AA}$ .

Figure 11

The unit cell Patterson functions for the five (— — —), the three (-----), and the two (————) bilayer arachidic acid multilayers reconstructed from the respective multilayer Patterson functions (figure 6) are shown. The three unit cell Patterson functions are typical for fatty acid multilayers with the sharp negative correlation at  $z = \pm d/2$ , and the sharp positive correlation at  $z = \pm d$ .

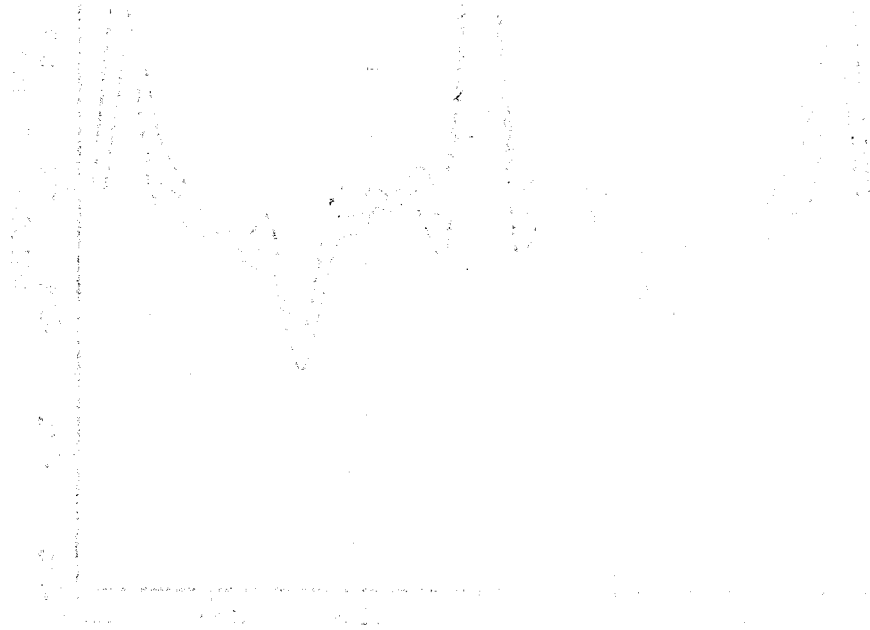
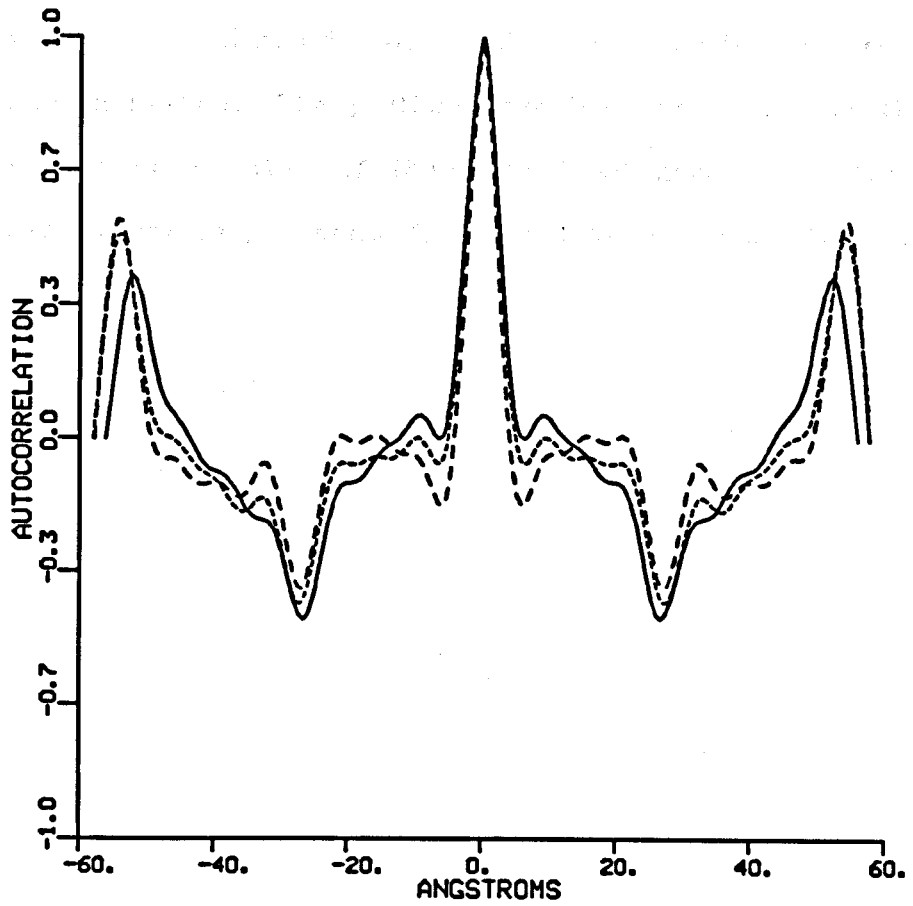


Figure 11



UNIT CELL PATTERSON  
N=2,3,5 arachidic acid

Figure 12

The electron density profiles for the average bilayer for the five (— — —), the three (-----), and the two (————) bilayer arachidic acid multilayers derived by unit cell Patterson recursive deconvolution method. The profiles have been normalized so that the relative electron densities of the polar head groups are the same. The recursive errors propagate from right to left in the figure.

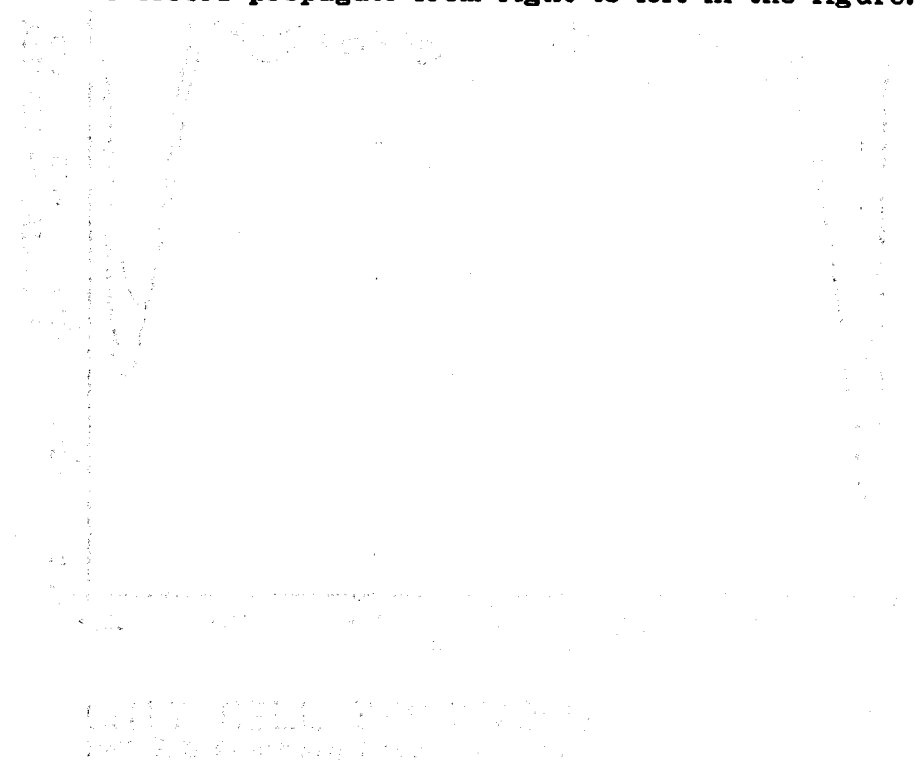
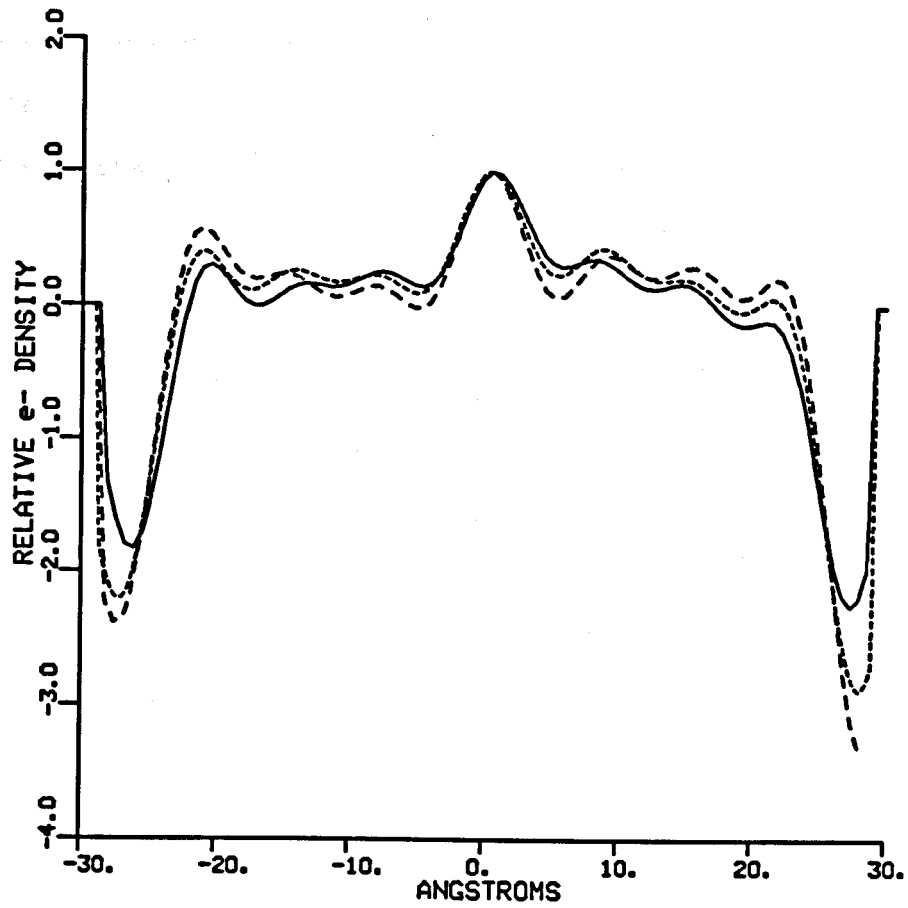


Figure 12



UNIT CELL DECONVOLUTION  
N=2,3,5 Arachidic Acid Bilayers

Figure 13

The electron density profiles for the average bilayer for the five (— — —), the three (— — — — —), and the two (————) bilayer arachidic acid multilayers derived by a correctly phased Fourier synthesis. The profiles have been normalized so that the relative electron densities of the polar headgroups are the same.

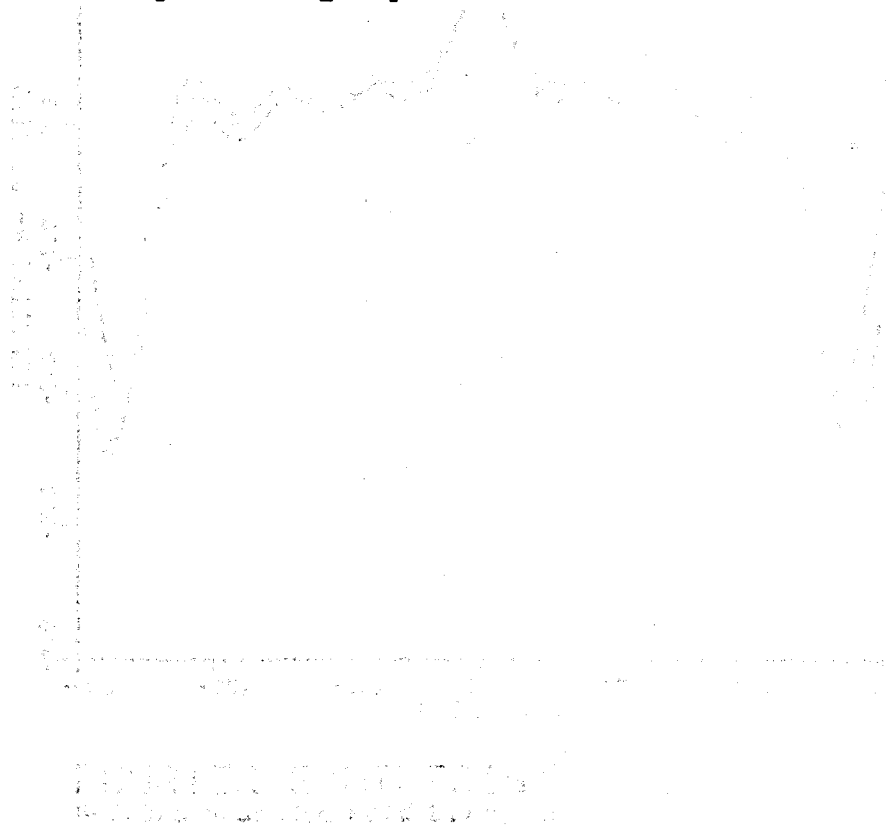
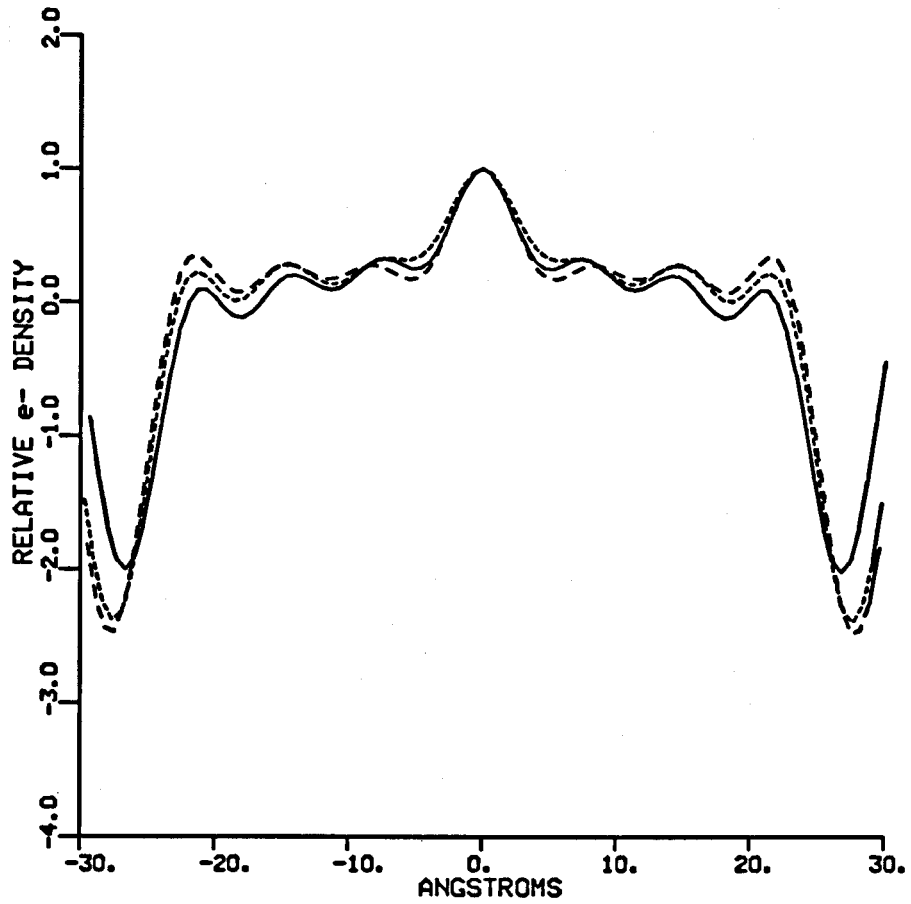


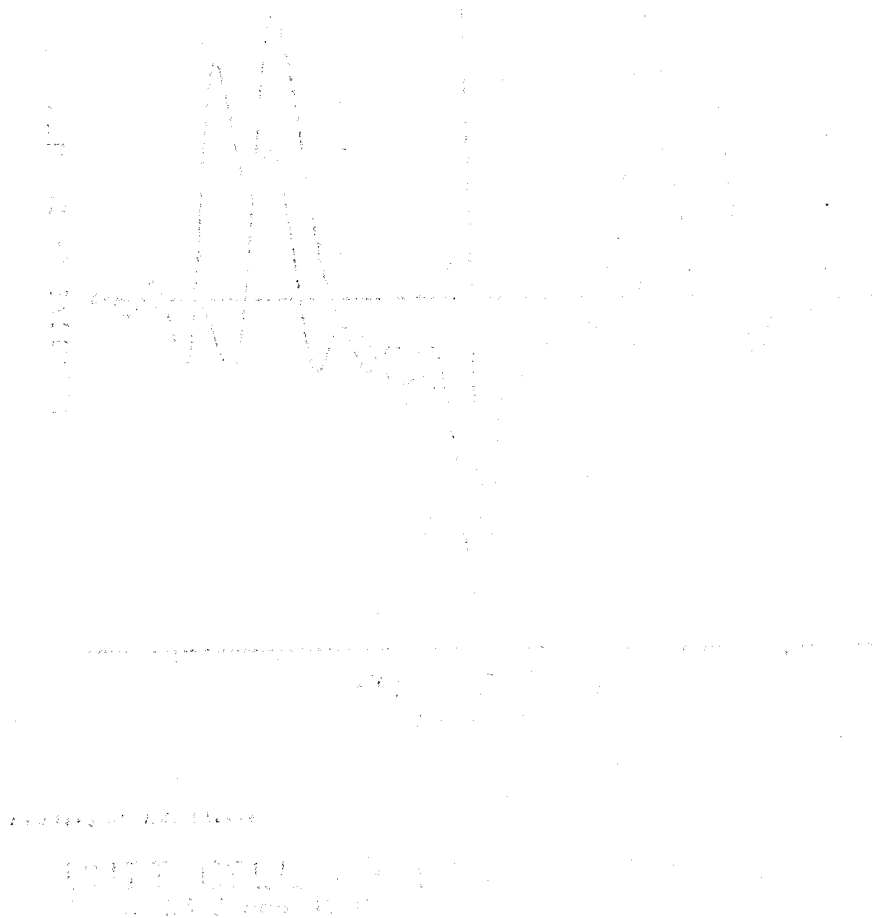
Figure 13



FOURIER SYNTHESIS  
N=2, 3, 5 Arachdic Acid Bilayers

**Figure 14**

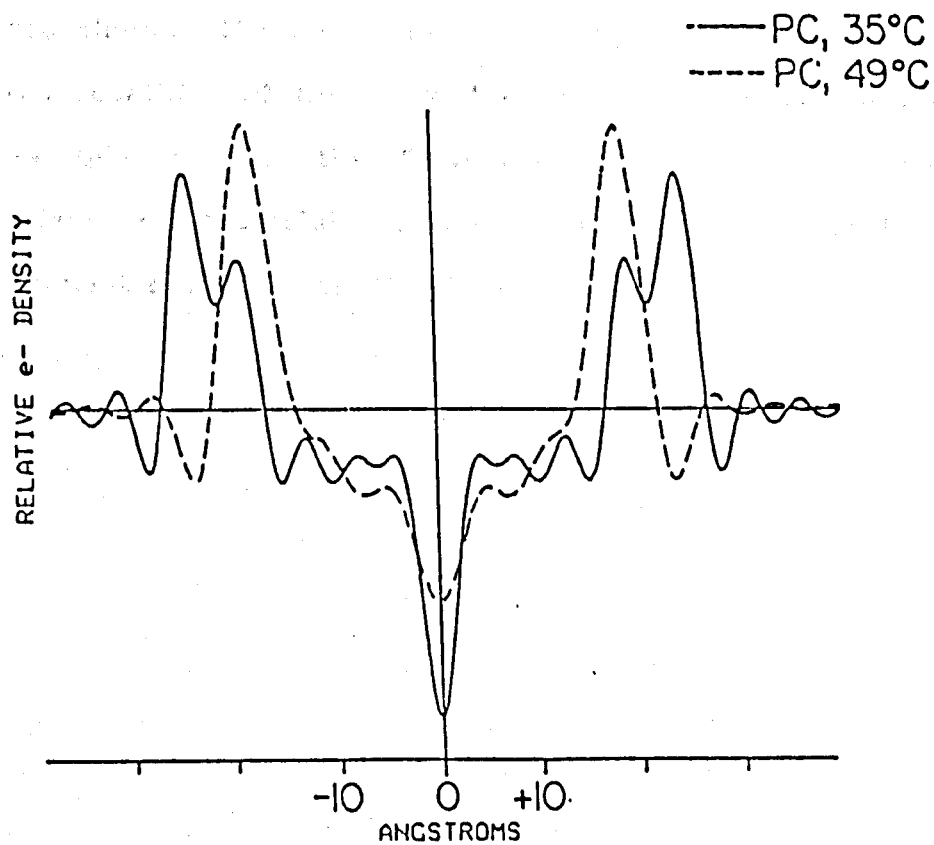
The unit cell electron density profile for a dipalmityl phosphatidyl choline (DPPC) bilayer at 35°C and 49°C. The former is below the phase transition temperature for chain melting, the latter above.



**Courtesy of J.K. Blasie from J. Cain, G. Santillan, and J.K. Blasie, Proceedings of 1972 ICN-UCLA Symposium on Molecular Biology. In Membrane Research, editor C.F. Fox, Academic Press, New York.**



Figure 14



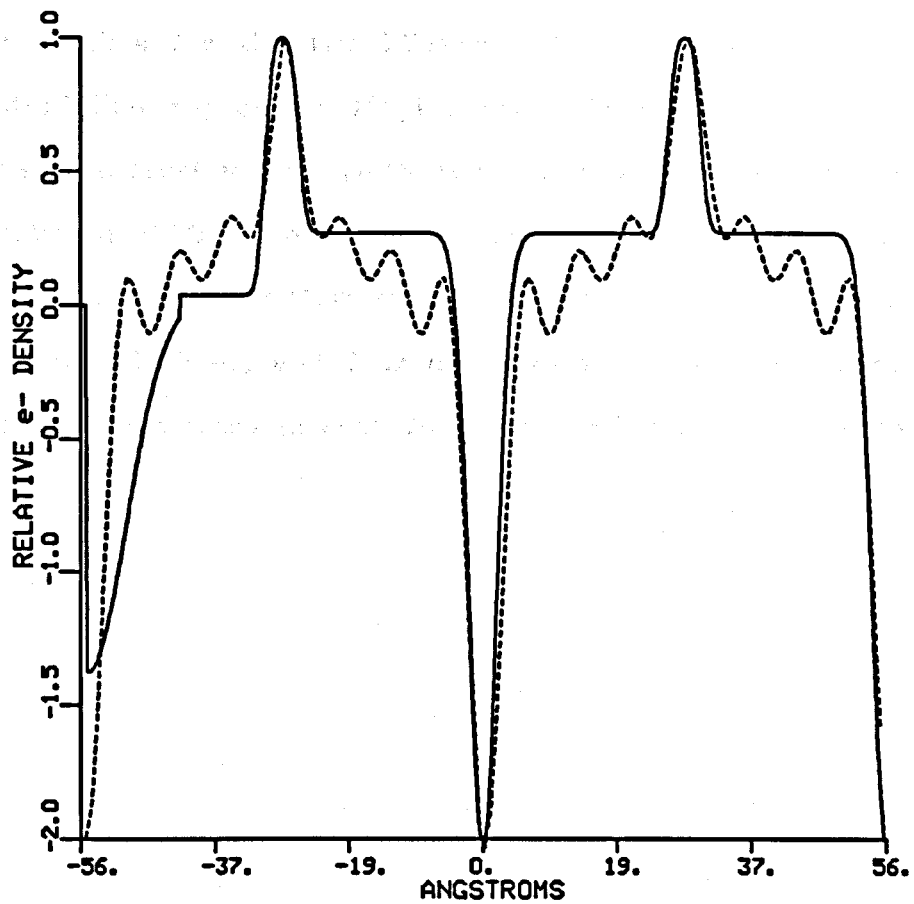
courtesy of J.K. Blasie

UNIT CELL e- DENSITY PROFILES  
DPPC, 35 C and 49 C

Figure 15

Two model multilayer electron density profiles for the two bilayer multilayer are shown. The dotted line represents a symmetric model based on the repetition of the derived electron density profile for the average bilayer from the Patterson function deconvolution procedure (*figure 13*); the solid line is an asymmetric model based on the box refinement multilayer profile (*figures 17 and 20*)

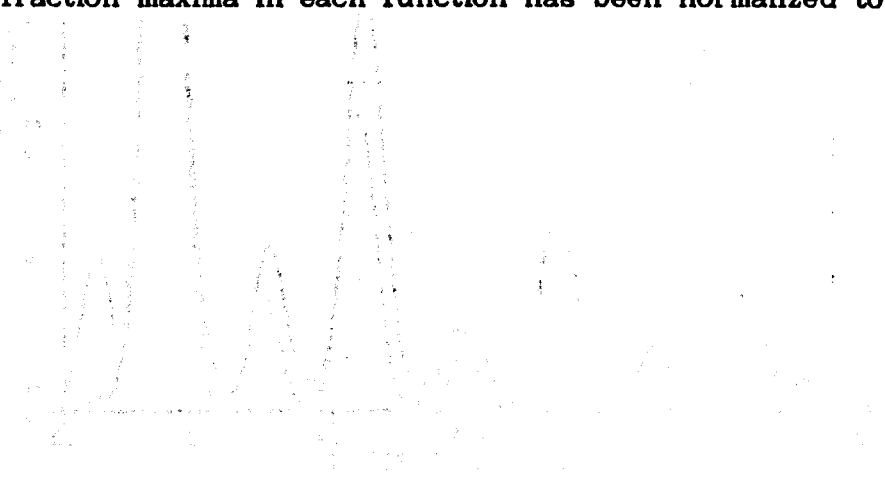
Figure 15



MODEL ELECTRON DENSITIES  
symmetric and asymmetric models (N=2)

Figure 16

Meridional intensity functions (after convolution with the incident beam-shape function) derived from the model multilayer electron density profiles for the two bilayer multilayer shown in figure 15. The dotted line represents  $I(q_z)$  derived from the symmetric model. Note the zero-level minima (with respect to a non-zero baseline, see text) between diffraction maxima. The solid line represents  $I(q_z)$  derived from the asymmetric model. The minima between diffraction maxima two and three, and four and five are clearly non-zero. The first diffraction maxima in each function has been normalized to one.

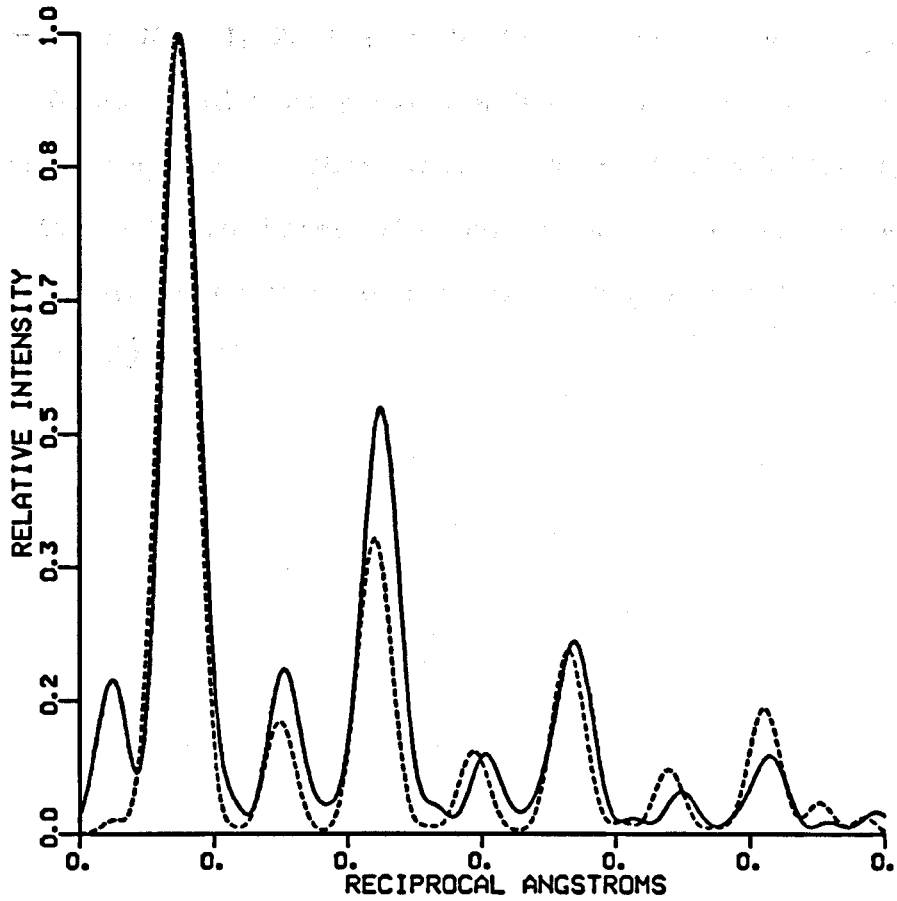


11/10/67

Figure 16

Two models were used to calculate the convoluted intensities for the symmetric (solid) and asymmetric (dashed) models. The results are shown in Figure 16.

The symmetric model (solid line) shows a sharp peak at approximately 0.05 reciprocal angstroms, reaching a relative intensity of 1.0. The asymmetric model (dashed line) shows a broader peak at the same position, reaching a relative intensity of approximately 0.95. Both models show smaller peaks at higher reciprocal angstrom values, with the symmetric model generally having higher relative intensities than the asymmetric model.

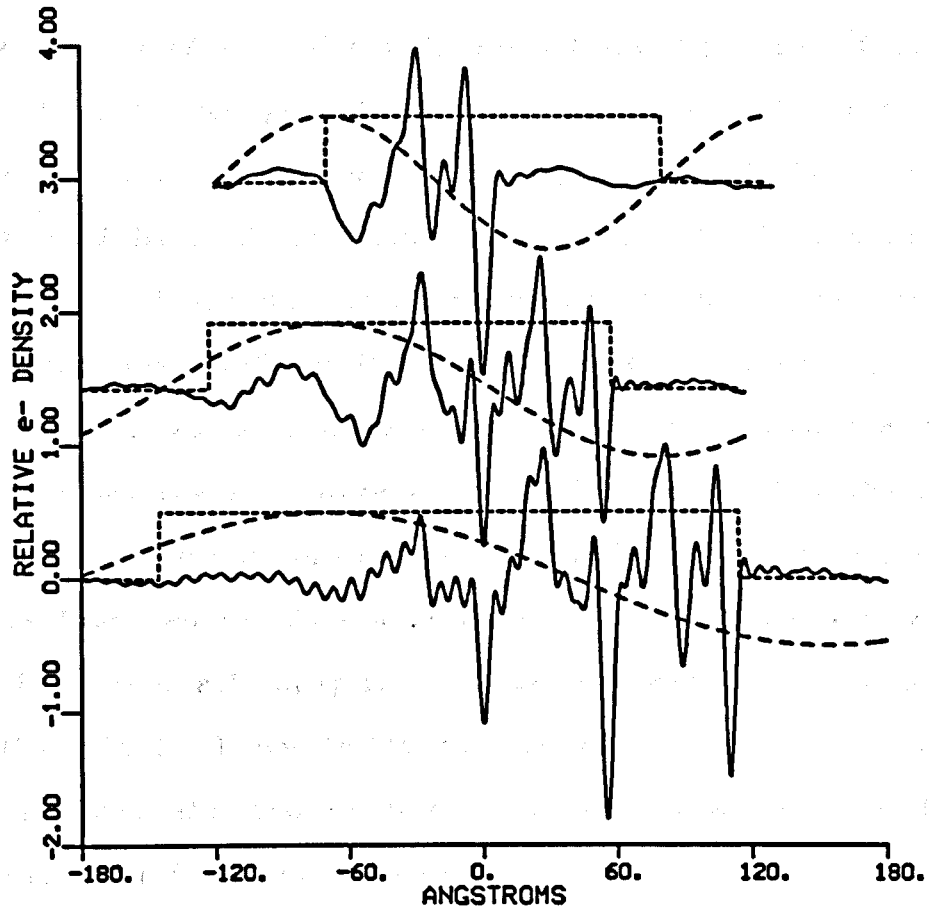


SYMMETRIC AND ASYMMETRIC MODEL  
convoluted intensities (N=2)

Figure 17

Box refinement trial functions (— — —), box boundary constraint functions (-----), and derived multilayer electron density profiles (————) for  $N = 1, 2, 3$  (top to bottom) bilayer multilayers are shown. These multilayers provide a homologous series for the box refinement procedure. Note that each profile exhibits features common to each multilayer electron density profile, as well as exhibiting features common to each monolayer within the multilayer electron density profile.

Figure 17



**BOX REFINEMENT PROFILES**  
N=1,2,3 arachidic acid bilayers

## Part II. Arachidic Acid, Myristic Acid, and 10,12 Pentacosadiynoic Acid Mixed Multilayers

An additional constraint to the box-refinement technique which is applicable when one wishes to determine the multilayer electron density profiles of several closely related multilayer thin films was developed for the analysis of the mixed multilayers. Box refinement itself requires that the electron density profile of the multilayer being refined be of finite extent. The additional criterium that we have established for our enhanced refinement (or "corefinement") requires that the multilayer thin films in question form a homologous series; namely, we assume that the profile structures for these multilayers are the same over a specified region. Thus the AAAA, AAAM, and AAMM multilayers are assumed to form a homologous series with the first two monolayers in each of the multilayers being an identical arachidic acid bilayer. The corefinement technique then adds the additional constraint to the box refinement procedure demanding that the two or more electron density profiles being simultaneously refined (*ie.* corefined) refine to profiles with the same electron density over the assumed appropriate region in real space. This is accomplished by numerically averaging the resultant electron density profiles over this corefined region of real space after each iteration. Corefinement may then be allowed to relax its additional constraint after a specified number of iterations.

Figure 18A shows the multilayer electron density profile for the AAAA multilayer corefined with the AAAM multilayer, figure 18B the



multilayer electron density profile for the AAAA multilayer corefined with the AAMM multilayer, and figure 18C the multilayer electron density of the AAMM multilayer corefined with the AAAM multilayer. In each case the electron density profiles were corefined over the region  $31\text{\AA} < z < 150\text{\AA}$ ; this region encompasses the first two arachidic acid monolayers. Relatively sharp, electron deficient troughs representing well-ordered terminal methyl groups are found at  $z = 84\text{\AA}$  and  $z = 32\text{\AA}$ , and an electron dense peak representing carboxyl headgroups is evident at  $z = 57\text{\AA}$  in each multilayer electron density profile. The last monolayer in each multilayer profile has a broad, electron deficient trough representing disordered terminal methyl groups at  $z \sim -24\text{\AA}$  for the AAAA multilayer,  $z \sim -20\text{\AA}$  for the AAAM multilayer, and  $z \sim -11\text{\AA}$  for the AAMM multilayer. The carboxyl head group peak region between the third and fourth monolayers is at  $z = 10\text{\AA}$  for the AAMM multilayer, and at  $z = 2\text{\AA}$  for the AAAM and AAAA multilayers.

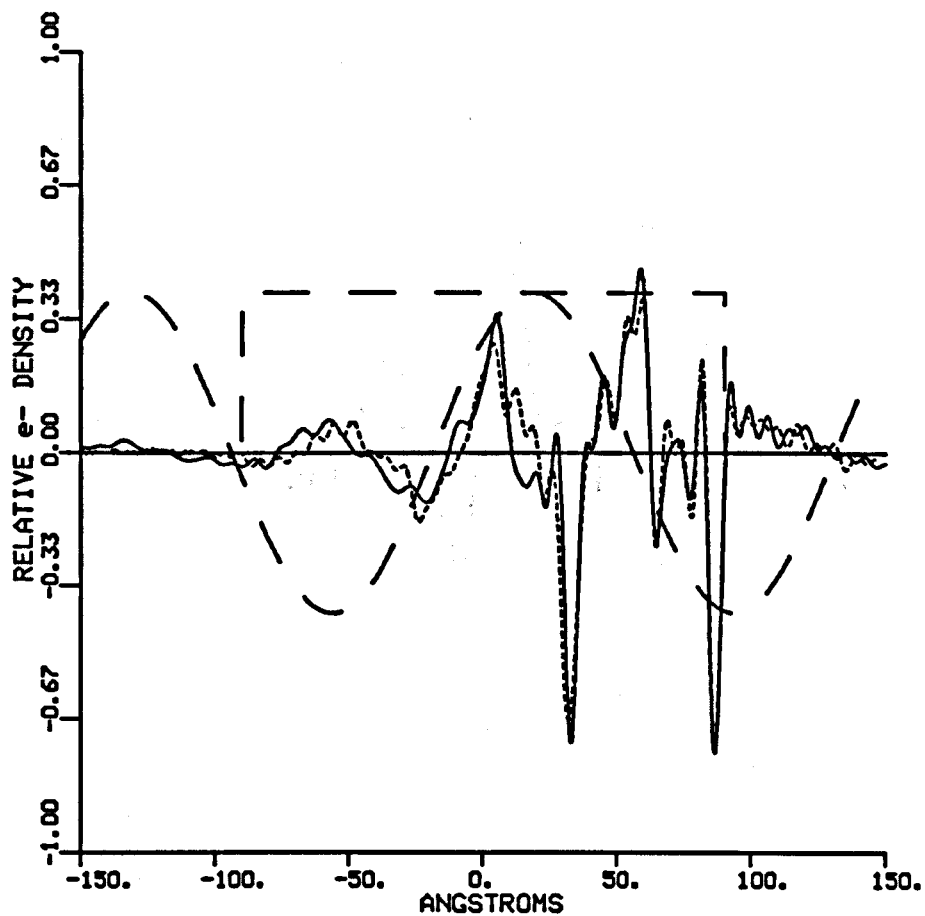
Figure 19 shows the derived multilayer electron density profiles for the DDDA multilayer and the DDD multilayer. The two profiles (thin solid lines) were corefined using the same initial trial (dotted lines) and box functions (dashed lines), and allowed to iterate eleven times. The region in real space where the two profiles were constrained to have the same electron densities are shown by the heavy solid lines. Both multilayer electron density profiles have sharp troughs representing well-ordered terminal methyl groups at  $z = 85\text{\AA}$  and  $z = 30\text{\AA}$ , and a carboxyl headgroup peak at  $z = 57\text{\AA}$ . Two

features in figure 5 should be noted. First, the carboxyl headgroup peak at  $z \sim 0A$  shows a significant decrease in electron density comparing the DDD multilayer electron density profile with the DDDA multilayer electron density profile. Second, the entire region  $-30A \leq z \leq 0A$  in the DDDA multilayer electron density profile, corresponding to the broad trough of disordered terminal methyl groups and adjacent hydrocarbon chain region of the arachidic acid monolayer, has a relative electron density well below zero level. For  $z < -30A$  the profile for the DDDA multilayer simply oscillates about zero electron density level. For the DDD multilayer, the electron density profile simply oscillates about the zero level for  $z < -5A$ .

Figures 18A, 18B, and 18C

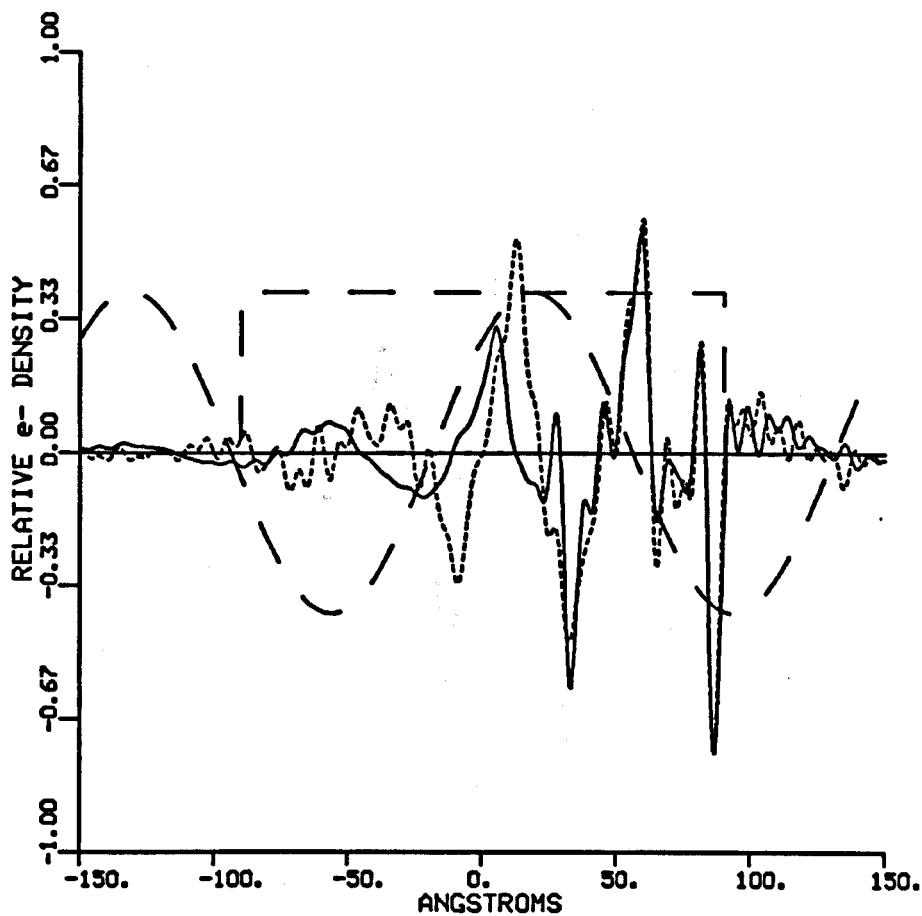
The electron density profiles derived by the variant of box refinement are shown. These profiles were corefined for five iterations and allowed to relax for an additional iteration. The refinements were corefined in real space for  $z > 35\text{\AA}$ . Figure 18A compares the electron density profiles derived by corefining the AAAA (solid line) and the AAAM (dotted line) multilayers. Figure 18B compares the electron density profiles derived by corefining the AAAA (solid line) and the AAMM (dotted line) multilayers. Figure 18C compares the electron density profiles derived by corefining the AAAM (solid line) and the AAMM (dotted line) multilayers. The initial trial function and the "box" used to truncate the profiles after each iteration are in each figure.

Figure 18A



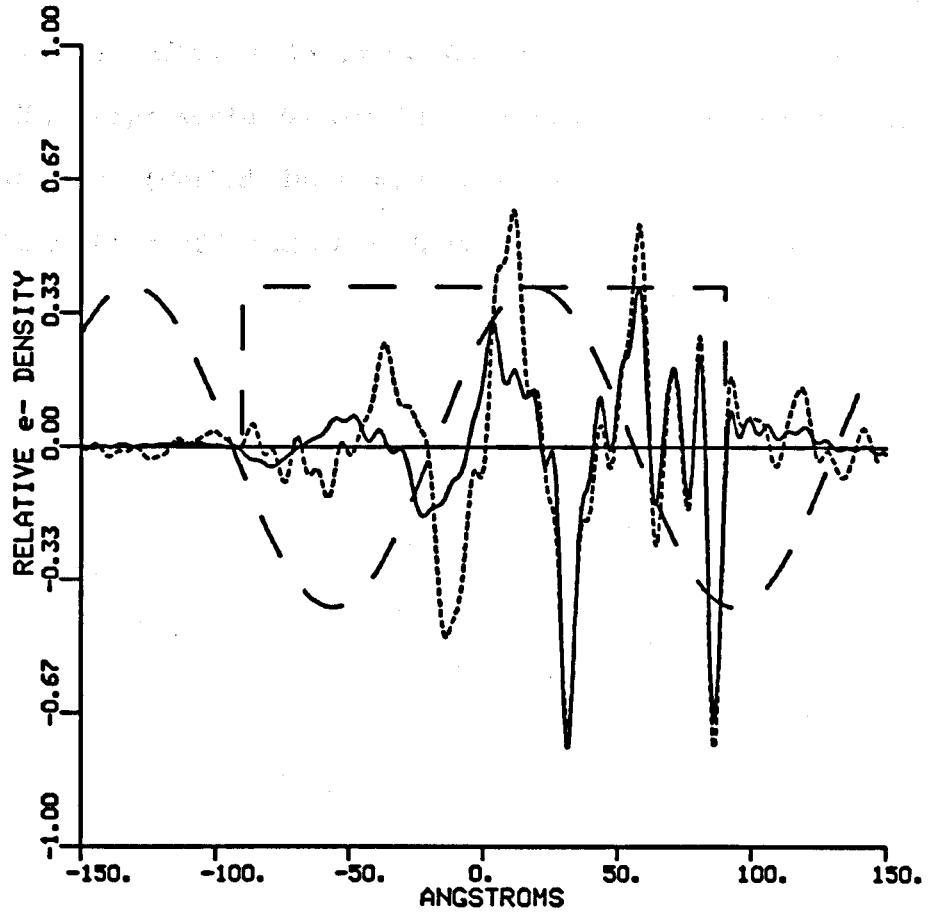
AAAM/AAAA COREFINEMENT  
AAAM (dotted line); AAAA (solid line)

Figure 18B



AAMM/AAAA COREFINEMENT  
AAMM (dotted line); AAAA (solid line)

Figure 18C



AAMM/AAAM COREFINEMENT  
AAMM (dotted line); AAAM (solid line)

Figure 19

The derived electron density profiles for the DDDA (upper) and DDD (lower) multilayers are shown. The profiles were corefined for ten iterations and allowed to relax for one additional iteration. The heavy line represents to corefined region in the refinement. The trial function (dotted line) and the "box" (dashed line) used in truncating the profiles after each iteration are also shown.

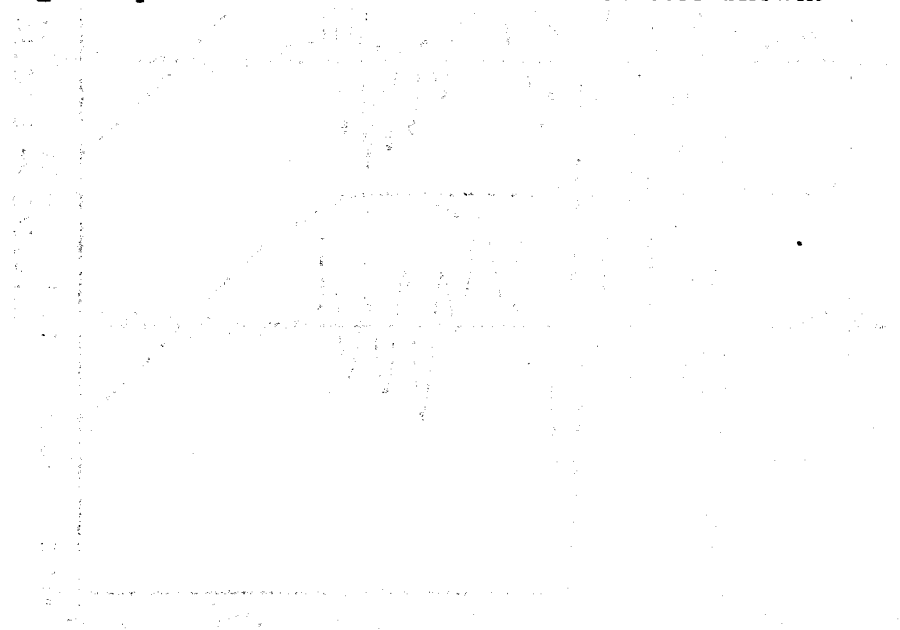
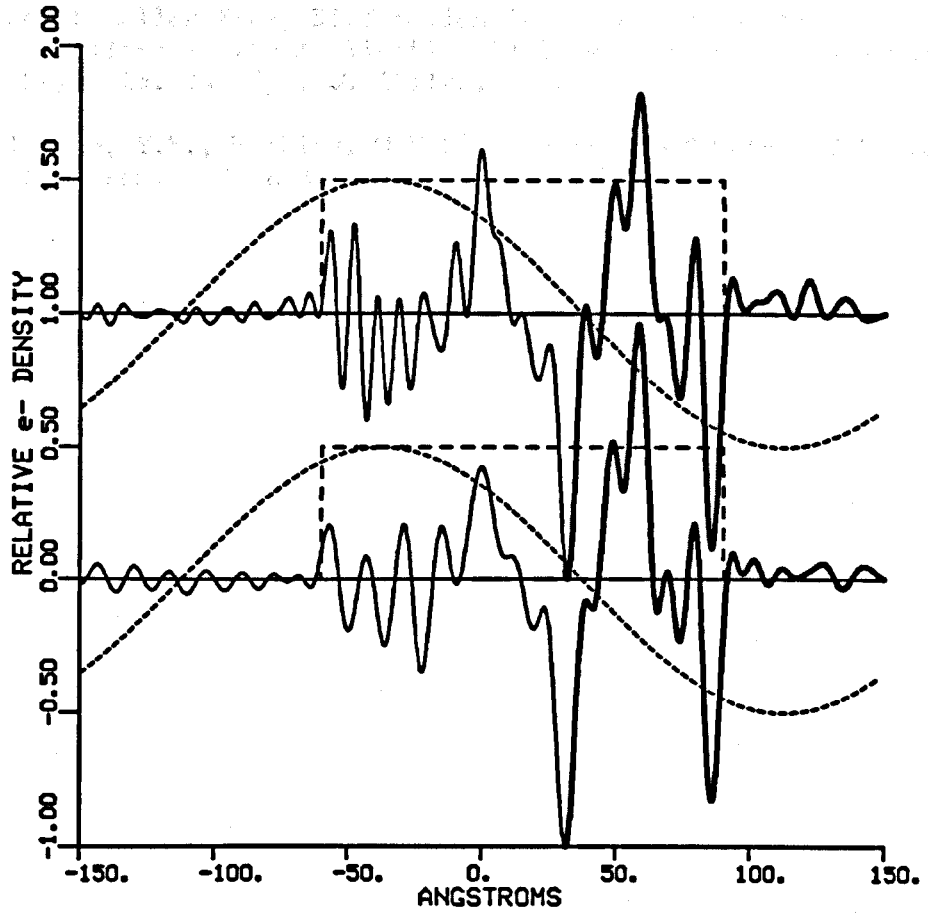


Figure 19



DDDA/DDD COREFINEMENT  
DDDA (upper plot); DDD (lower plot)



## REFERENCES FOR CHAPTER FIVE

- [5-1] Lesslauer, W., Cain, J., Blasie, J.K. On the Location of 1-Anilo-8-Naphthalene-Sulfonate in Lipid Model Systems. *BBA* 241:547-566 (1971)
- [5-2] Schwartz, S., Cain, J., Dratz, E., Blaise, J.K. An Analysis of Lamellar X-Ray Diffraction From Disordered Membrane Multilayers with Application to Data from Retinal Rod Outer Segments. *Biophys. J.* 15:1201-1233 (1975)
- [5-3] Levine, Y.K., Wilkins, M.H.F. Structure of Oriented Lipid Bilayers. *Nature New Biology* 230:69-72 (1971)

## CHAPTER SIX: DISCUSSION

### Part I. Arachidic Acid Multilayers: Box Refinement

The dotted-lines in figures 5 and 6 represent the corrected intensity and Patterson functions respectively for the one, two and three arachidic acid bilayer multilayers calculated from the multilayer profiles derived by the box refinement technique. The calculated corrected intensity functions and the calculated multilayer Patterson functions all agree extremely well with the original experimental functions. The calculated intensity function reproduces the shape, the relative intensity, and the position of the diffraction maxima; the fine features of the multilayer Patterson function are also reproduced. The continuous multilayer electron density profiles all show an anomaly at  $z = -9A, 47A, 104A$  for the  $N = 1, 2, 3$  multilayer sample respectively. This anomaly has the same characteristics in each of the derived profiles; it is a positive spike following the first well-defined methyl trough at one end of the multilayer profile. The derived multilayer electron density profiles must conform to a reasonable physical-chemical interpretation. Aside from the above mentioned anomaly, they all do.

To study the anomaly, step-function model electron density profiles equivalent to the continuous multilayer profiles were constructed (figure 20). The anomaly is shown as a dashed line in each model. Each step represents  $\sim 3A$  in  $z$ . The anomaly was attenuated to between 12 - 25% of its original magnitude in the model profiles, from which model intensity functions and model multilayer

Patterson functions were calculated and compared to the original corrected intensity functions  $I_0(q_z)$  and multilayer Patterson functions  $P_{m1}(z)$ .

Figure 21 shows the intensity functions calculated from the continuous multilayer electron density profile, the step-function model profiles, and the original Lorentz corrected intensity function  $I_0(q_z)$  for the N=2 multilayer. Note, the excellent agreement between the intensity function derived from the continuous multilayer electron density profile and the experimental intensity function. The step-function models also give good agreement with the experimental intensity function, with some qualifications. By constructing step-function model profiles of finite spatial resolution, the magnitude of the diffraction maxima for  $q_z > .075\text{\AA}^{-1}$  were perturbed; their shape and position remained the same. Differences between the derived model intensity function and the corrected intensity function  $I_0(q_z)$  for  $N = 2$  occur mainly at  $q_z \sim .02\text{\AA}^{-1}$  and reflect a difference in the magnitude of the first diffraction maximum. Other features of the corrected intensity function including the diffraction maxima shapes, positions and magnitudes are preserved. As previously mentioned, unavoidable errors in determining the magnitude of the first order diffraction maxima occur due to the background scattering correction applied to the uncorrected intensity function. Error in the relative magnitude of the first diffraction maxima contributes to errors in the multilayer electron density profiles derived by box refinement. Box refinement cannot compensate for errors in the

corrected intensity function, rather it will just refine to them. The origin (with respect to the intensity function) of a particular feature in the continuous multilayer electron density profile can be investigated by perturbing the feature and calculating corresponding intensity functions.

The multilayer Patterson function calculated from the multilayer electron density profile derived by box refinement (figure 22) and the multilayer Patterson function  $P_{m_1}(z)$  calculated from the corrected intensity function  $I_0(q_z)$  agree extremely well, as do the step-function model derived multilayer Patterson functions. The step-function model derived Patterson functions deviate from  $P_{m_1}(z)$  for  $z > 1.5d$  (where  $d$  is the "average" periodicity of the multilayer profile). The vectors contributing to the Patterson function for  $|z| > 1.5d$  represent correlations between the first and the last monolayer; these correlations correspond primarily to momentum transfer vectors  $q_z < .013\text{\AA}^{-1}$ . This region of momentum transfer space corresponds to the first diffraction maxima; the magnitude of which is most prone to error in the analysis. The small ringing of the multilayer Patterson function at  $|z| > 2d$  is also partially a result of this error and the truncation of the data for  $q_z < 0.01\text{\AA}^{-1}$ . Since the step-function models are of limited spatial resolution the feature at  $z = \pm 62\text{\AA}$  in  $P_{m_1}(z)$  has become a shoulder on the multilayer Patterson function derived from the step-function models.

Hence, it has been shown that errors in  $I_0(q_z)$  for  $q_z < .02\text{\AA}^{-1}$  are essentially responsible for the anomalies in the box refinement

derived multilayer electron density profiles. However, these errors do not deter the box refinement technique from determining correctly the general features of the multilayer electron density profiles.

Figure 20

The step-function models derived from the continuous multilayer electron density profiles shown in figure 17. The anomaly is shown by the dotted line.

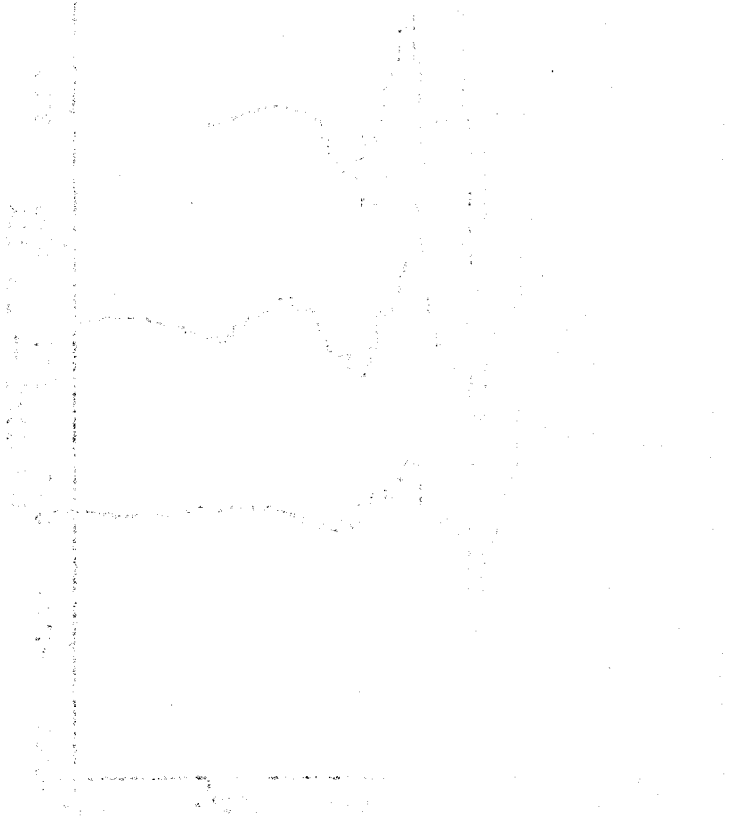
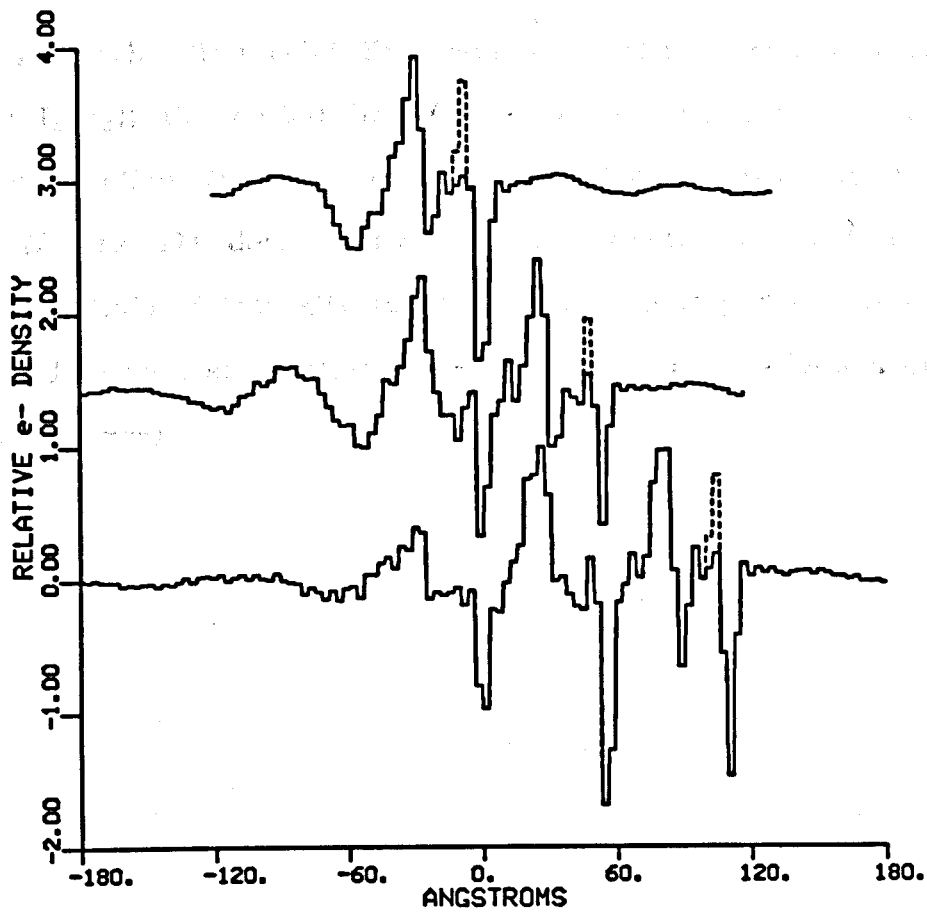


Figure 20



STEP-FUNCTION MODELS  
N=1,2,3 arachidic acid bilayers

Figure 21

Calculated Lorentz- $q_z$  corrected intensity functions for the two bilayer multilayer versus the corrected experimental intensity function,  $I_o(q_z)$ . The solid line represents the corrected intensity function  $I_o(q_z)$ ; the dotted line (— · — · —) represents the calculated intensity function from the continuous multilayer electron density profile (figure 17) derived by box refinement; the dashed lines represent calculated intensity functions from the step-function models (figure 20) without attenuation (— — —) and with attenuation of the anomaly (— — —)

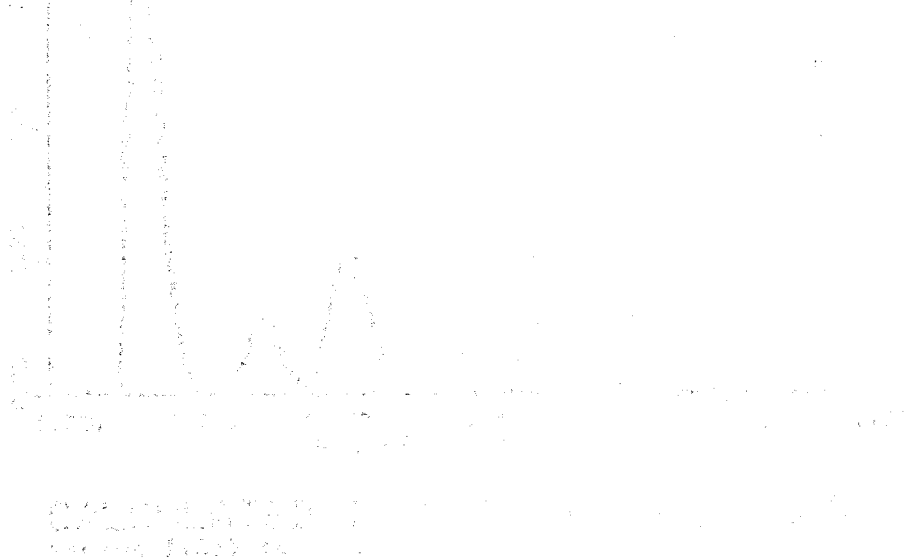
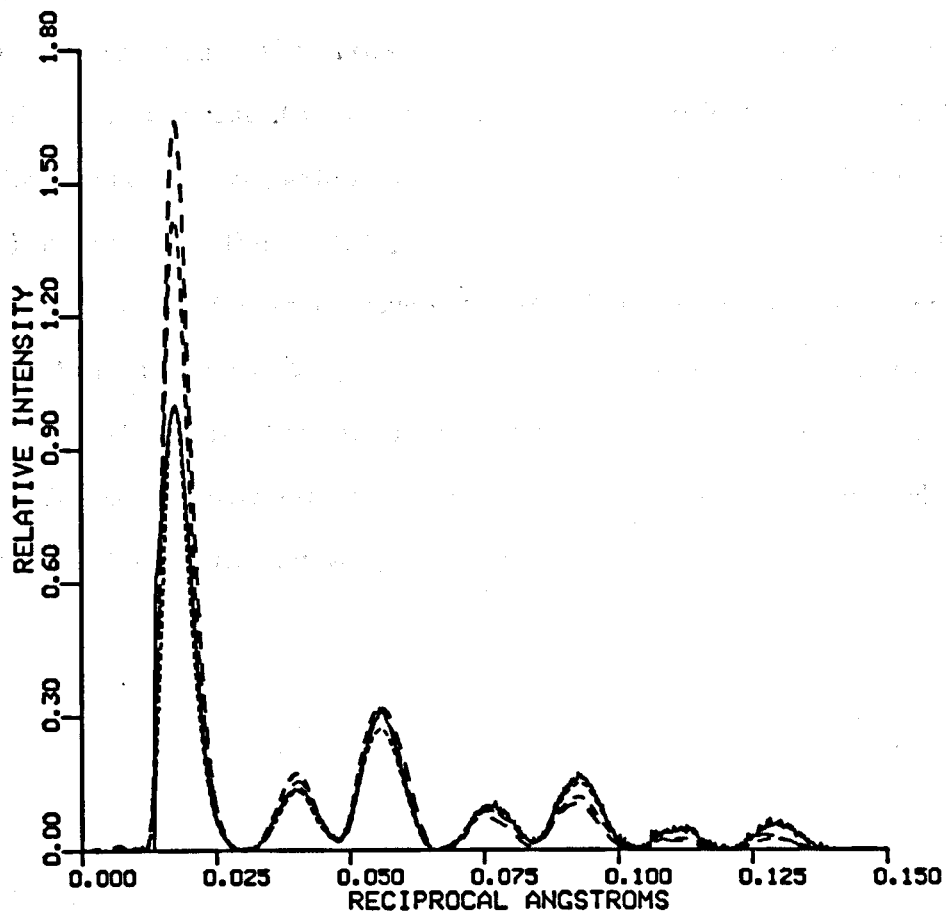




Figure 21

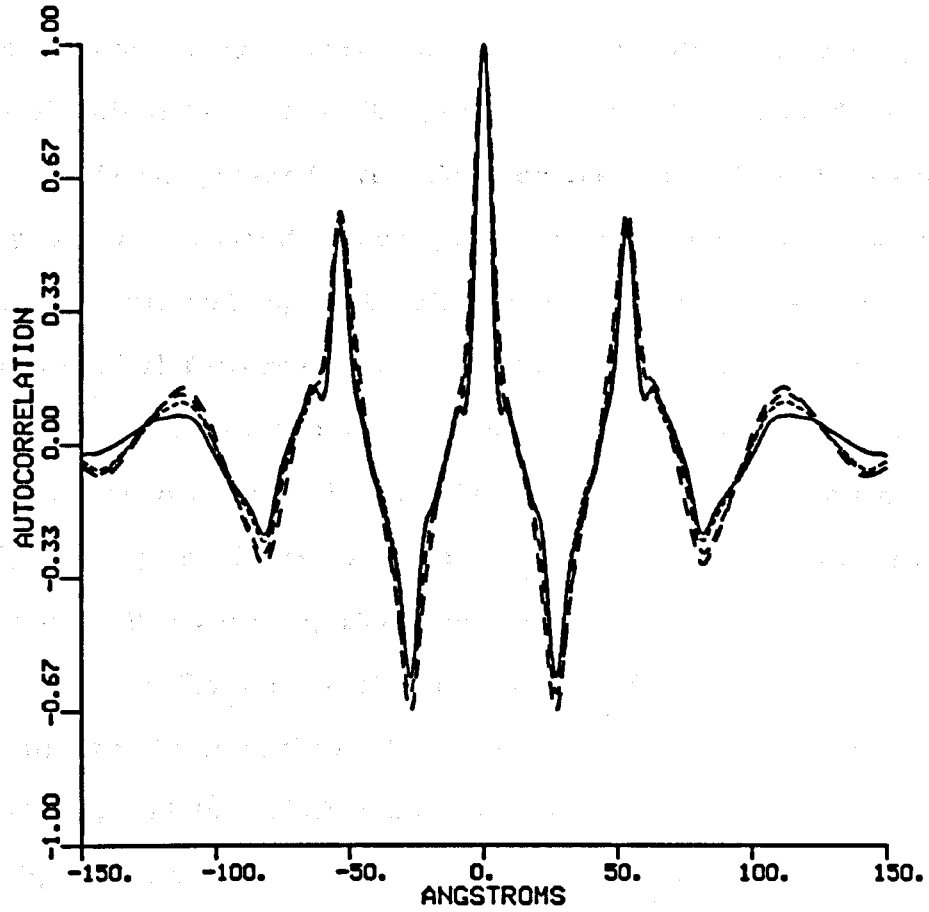


CALCULATED INTENSITY FUNCTIONS  
versus  $I(Qz)$  for  $N=2$

Figure 22

Calculated multilayer profile Patterson functions for the two bilayer multilayer versus the multilayer Patterson function derived by Fourier transforming the Lorentz  $q_z$  corrected intensity function. The solid line represents the multilayer Patterson function derived from the corrected experimental intensity function; the dotted line (— · — ·) represents the multilayer Patterson function calculated from the continuous multilayer electron density profile (figure 17) derived by the box refinement procedure; the dashed lines represent multilayer Patterson functions calculated from the step-function models (figure 20) without attenuation of the anomaly (— — —) and with attenuation of the anomaly (— —).

Figure 22



CALCULATED PATTERSON FUNCTIONS  
versus  $P_{m1}(z)$  for  $N=2$

## Part II. Arachidic Acid Multilayers: Model Calculations

It is possible to investigate the derived multilayer electron density profiles further by constructing physical-chemically reasonable, yet mathematically simple multilayer electron density profiles (using only analytical functions) and calculating the meridional intensity and multilayer Patterson functions from these models. While the intensity functions derived from the step-function model profiles described above yield excellent agreement with the experimental intensities, not all their features represent true physical-chemical features in the multilayer electron density profiles. Three types of errors can be seen in these models. The first is a high frequency oscillation in the electron density profile as a result of only using a finite number of diffraction maxima in the calculations. For example, the step-function model for  $N = 2$  shows about a 20% oscillation in the magnitude of the electron density profile in the hydrocarbon chain region. This is not physically interpretable, and is probably due to this type of error. The second is a very low frequency error resulting from errors in truncating  $I_0(q_z)$  for  $q_z < 0.02\text{\AA}^{-1}$ . The third results from not deconvoluting the beam width function,  $W(q_z)$ , from the intensity function. This error causes the electron density profile to be modulated by a Gaussian-like function whose full width at half maximum is proportional to the inverse of the FWHM of  $W(q_z)$ . In a model, it is reasonable to replace the high frequency oscillations with a constant electron density value and then recalculate the intensity and compare

it to the experimental intensity. Other features can also be replaced; the methyl troughs can be fitted with Gaussian functions for instance.

The continuous electron density profiles derived by the box refinement method yield intensity functions which match the experimental intensity very well (figures 5 and 21). These calculated intensities are zero for  $q_z < .01\text{\AA}^{-1}$  and  $q_z > .14\text{\AA}^{-1}$ . While data was not collected in these regions of momentum transfer space, the intensity function is not truly zero in those regions.

Before constructing a physical-chemical model for the multilayer profile based on the step-function model electron density profile derived from the box refinement, it is necessary to investigate some of the features of the corrected intensity function,  $I_o(q_z)$ . The N=2 data set was chosen for modeling since it was the most accurate with respect to the previously mentioned errors. The first diffraction maxima was reasonably resolved from the specular scattering and the beam-shape function was considerably more narrow than the diffraction maxima. Consider the corrected intensity function for N = 2 in figure 21 (solid line). The corrected intensity function has non-zero minima at  $q_z = .048\text{\AA}^{-1}$  and  $q_z = .085\text{\AA}^{-1}$ , between diffraction maxima two and three, and maxima four and five respectively. These non-zero minima can arise from asymmetry in the multilayer electron density profile. The centrosymmetric multilayer profile model discussed earlier (dotted line, figure 15) did not reproduce the intensity function very well (dotted line, figure 16).

In addition, maxima two and three, and four and five are shifted closer together, and are not spaced exactly  $1/d$  apart. Maxima four and six have shoulders at  $q_z = .071\text{\AA}^{-1}$  and  $.107\text{\AA}^{-1}$  respectively. The shoulder may very well arise from convoluting the beam width function with the modulus squared of the multilayer profile structure factor. This beam width convolution is responsible for the auxiliary maxima appearing as shoulders on the principal maxima in  $|F_m(q_z)|^2$ .

The solid line in figure 15 shows an electron density profile model which has some of the features of the centrosymmetric two bilayer model (dotted line, figure 15), but is simpler and asymmetric. The relative magnitudes of the carboxyl peaks ( $z = \pm 27.5\text{\AA}$ ) compared to the methyl troughs at  $z = 0\text{\AA}$  and  $z = 56\text{\AA}$  have been maintained. The hydrocarbon chain regions between the peaks and troughs are now flat. The methyl trough at  $z = -56\text{\AA}$  was broadened and shifted one Angstrom toward the center of the multilayer profile. The hydrocarbon chain region for  $-42\text{\AA} < z < 32\text{\AA}$  also has an average electron density lower than the other hydrocarbon chain regions by about 7.5%. (This is required on physical grounds, namely an increased area/chain in the plane of the bilayer of the hydrocarbon chain region is required if the methyl trough at  $z = -56\text{\AA}$  is to become broad, shallow and shifted toward the neighboring carboxyl peak). The calculated intensity,  $I(q_z)$ , and its anti-symmetric component (see appendix VII),  $I_A(q_z)$  are shown in Figure 23. Note the non-zero minima at  $q_z = .046\text{\AA}^{-1}$  is entirely due to the anti-symmetric component of the intensity function, while  $I_A(q_z)$

contributes about 50% to the non-zero minima at  $q_z = .82A^{-1}$ . Also note the auxiliary maxima at  $q_z = .061A^{-1}$  and  $.102A^{-1}$  as well as non-zero calculated intensity at  $z < .01A^{-1}$  and  $z > .130A^{-1}$ . The relative intensities and shapes of the diffraction maxima seem to be in reasonable agreement with the corrected intensity function  $I_o(q_z)$  (figures 5 and 21) except for the relative magnitude of the first maxima. As previously mentioned, errors in the magnitude of the first diffraction maxima occur due to errors in background scattering correction. The odd maxima decay with increasing  $q_z$  slower than do the even maxima in both the calculated and corrected intensities, with the fourth maximum being about the same magnitude as the second. The seventh maximum is slightly more intense than the sixth; the second is about 50% the magnitude of the third; and the fourth maximum is about 50% of the fifth. The sixth and seventh maxima are about the same magnitude. The non-zero minima have also been reproduced.

The solid-line in figure 16 shows the calculated intensity function convoluted with the experimental incident beam-shape function. Note that the auxiliary maxima have flattened and caused the broadening of adjacent maxima. This is especially apparent at  $q_z = .033A^{-1}$ ,  $.076A^{-1}$  and  $.112A^{-1}$ . Convoluting the calculated intensity function with the experimental beam-shape function makes it non-zero everywhere. However, the calculated intensity function's minima at  $q_z = .055A^{-1}$  and  $.092A^{-1}$  are above this new base-line, and reproduce the corrected intensity function  $[I_o(q_z)]$  fairly accurately (figures 5 and

21).

The results from the box-refinement method for  $N = 1, 2,$  and  $3$  multilayers and the model calculations for  $N = 2$  indicate that only one monolayer at one edge of the multilayer is disordered. For the  $N = 1, 2,$  and  $3$  multilayers, this one disordered monolayer has a broad shallow methyl trough and a non-flat hydrocarbon chain region characteristic of disordered chains whose average end-end chain length is less than that for all *trans* chains. This first series of experiments cannot conclusively determine whether the first monolayer which interfaces the glass-OTS surface, or the last monolayer which interfaces air, is the disordered monolayer. This result is not surprising when one considers that the OTS hydrocarbon chain is very similar (on a macromolecular level) to that of arachidic acid. Deposition of the first arachidic acid monolayer onto the glass-OTS surface should not be very different (with respect to inter-molecular forces between monolayers) than depositing the third monolayer onto the second, or the fifth onto the fourth, *et cetera*. The last monolayer is not constrained by the terminal methyl groups of a juxtaposed monolayer. The chain terminal methyl groups of the last monolayer interface with air; consequently these chains appear to have more degrees of freedom than the chain terminal methyl groups of the internal monolayers in the multilayer.



Figure 23

The calculated intensity function  $I(q_z)$  (solid line) for the two bilayer multilayer and its anti-symmetric contribution  $I_A(q_z)$  (dotted line). These functions were calculated from the two bilayer asymmetric model (figure 15, solid line) and were not convoluted with the incident beam shape function.

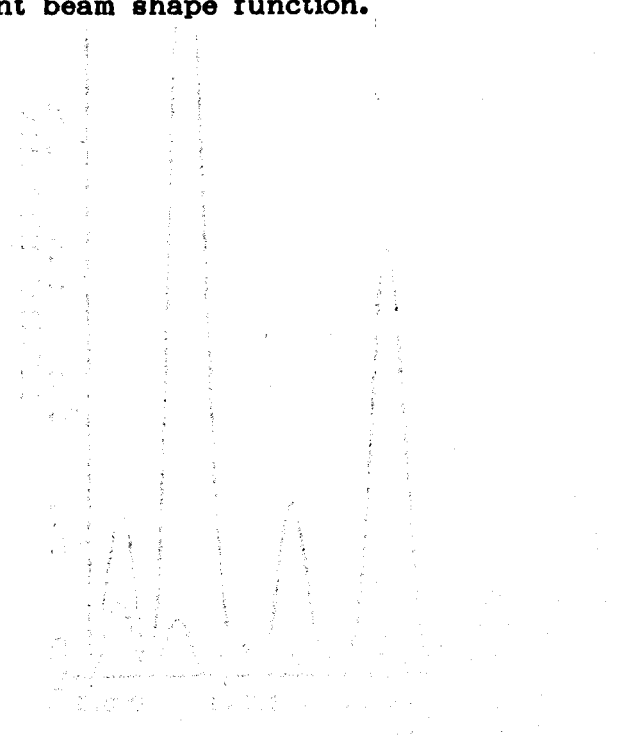
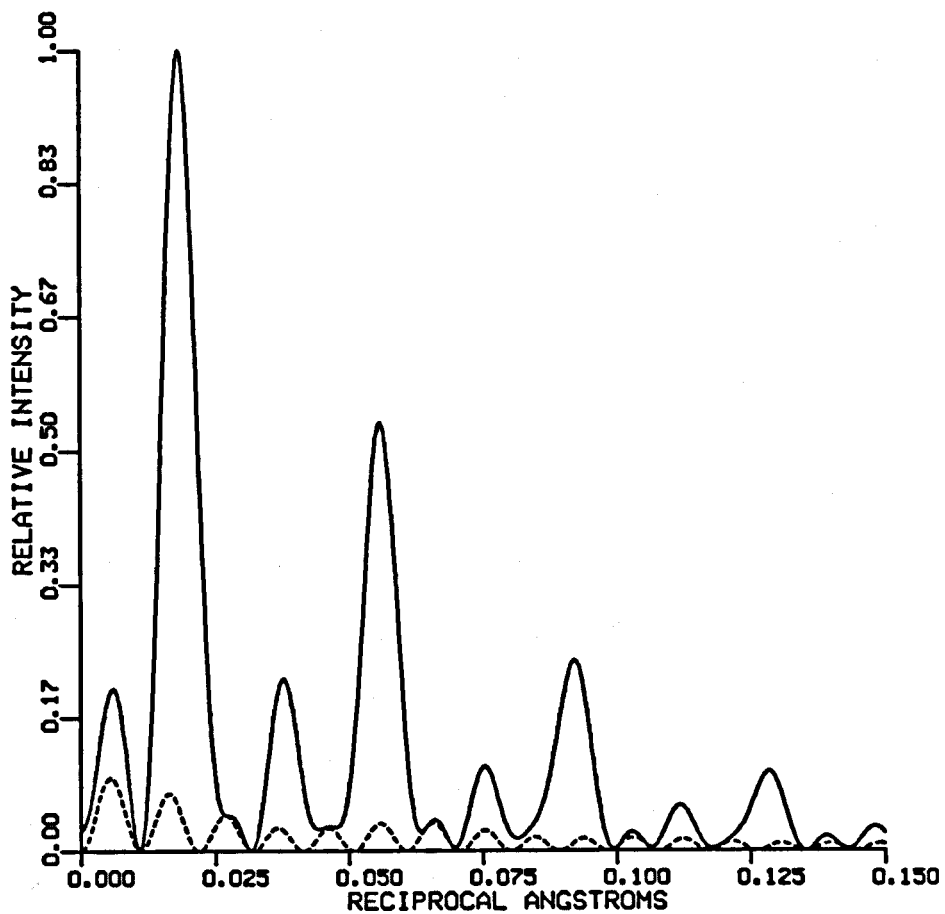


Figure 23



MODEL INTENSITY (N=2)  
AND ASYMMETRIC CONTRIBUTION

### Part III. Arachidic Acid, Myristic Acid, and 10,12 Pentacosadiynoic Acid Mixed Multilayers

The decreasing values of  $z_{\max}$  for the multilayer profile autocorrelation functions for the AAAA, AAAM, and AAMM multilayers are consistent with the expected changes in the extent of the multilayer profiles. However, difficulty in determining  $z_{\max}$  with certainty due to errors in  $I(q_z)$  for  $z < \sim .02\text{\AA}^{-1}$  limits its usefulness in the determination of the precise extent of the multilayer profiles (figure 8). Periodic multilayers, where the unit cell translation vector projected onto the z-axis has magnitude  $d$ , have autocorrelation functions which contain local maxima at integer multiples of  $d$ . In figure 8 the autocorrelation function of the AAAA multilayer shows such a local maximum at  $|z| = 54\text{\AA}$  dominated by the entirely positive correlations between the first monolayer and the third monolayer and between the second monolayer and the fourth monolayer; in addition a local minimum occurs at  $|z| = 27\text{\AA}$  dominated by the negative correlations between the electron deficient terminal methyl groups ( $-\text{CH}_3$ ) of the arachidic acid monolayers and the electron dense carboxyl headgroups ( $-\text{COOH}$ ) of adjacent monolayers. The autocorrelation function of the AAMM multilayer has a local maximum at  $|z| = 48\text{\AA}$  with distinct shoulders at  $|z| = 54\text{\AA}$  and  $|z| = 38\text{\AA}$ ; and local minima at  $|z| = 27\text{\AA}$  and  $|z| = 19\text{\AA}$ . Note the absence of such features at  $|z| = 19\text{\AA}$ ,  $|z| = 38\text{\AA}$ , and  $|z| = 48\text{\AA}$  in the autocorrelation function for the AAAA multilayer. In addition note the appearance of a positive shoulder at  $|z| = 48\text{\AA}$  and a distinct

negative feature at  $|z| \approx 19\text{\AA}$  in the autocorrelation function for the AAAM multilayer. The derived electron density profiles for the AAAA, AAAM, and AAMM multilayers (figures 18A, 18B, 18C) yield an average myristic acid carboxyl-methyl distance per monolayer of  $22 \pm 1\text{\AA}$  and an average arachidic acid carboxyl-methyl distance per monolayer of  $27 \pm 1\text{\AA}$ . The features noted above in the autocorrelation functions of the AAAA, AAAM, and AAMM multilayer profiles clearly demonstrate the sensitivity of the multilayer profile autocorrelation function in detecting changes in composition of the monolayers in the multilayer thin film.

The hydrocarbon chains of the macromolecules in one monolayer at the edge of each multilayer profile are significantly disordered as evidenced by a relatively broad methyl trough feature consistently at one end of the multilayer electron density profile. From the electron density profiles, the calculated difference in the average carboxyl-methyl end group distance between the arachidic acid and the myristic acid monolayers as noted above is consistently  $\sim 5\text{\AA}$  for the AAAA, AAAM, and AAMM multilayers. Hence, by varying the carboxyl-methyl end group distance for the last one or two monolayers in the deposition sequence by substituting myristic acid for arachidic acid in the AAAA/AAAM/AAMM experiments, one observed the appropriate shifting of the broad methyl trough feature at one end of the electron density profile (AAAA versus AAAM), or the appropriate shifting of both the broad methyl trough feature and the adjacent carboxyl headgroup region (AAAA versus AAMM, AAAM

versus AAMM) in the multilayer electron density profiles (figures 18A, 18B, 18C). The changes in the multilayer electron density profile of the DDDA multilayer (figure 19) upon the removal of the final arachidic acid monolayer to form the DDD multilayer is clearly evident. The electron density profile for the latter shows the absence of the broad methyl trough at  $z = -25\text{\AA}$ , as well as the decrease by factor of two of the carboxyl head group peak feature between the third and fourth monolayer at  $z = 0\text{\AA}$  when the fourth monolayer is removed. The multilayer profile autocorrelation function for the DDDA and DDD multilayers are consistent with the removal of the last arachidic acid monolayer. The pronounced positive correlations for  $z \sim z_{\text{max}}$  ( $\sim 110\text{\AA}$ ) for the DDDA multilayer are between the electron deficient terminal methyl group regions of the first (D) and last (A) monolayers deposited. The only negative correlations for  $z \sim z_{\text{max}}$  ( $\sim 90\text{\AA}$ ) for the DDD multilayer are between the electron dense carboxyl headgroup region of the last or third monolayer (D) and the electron deficient terminal methyl group region of the first monolayer (D) at the OTS-glass substrate surface.

Since we know the sequence in which the different macromolecular monolayers were deposited during the fabrication of the multilayers, the two sets of experiments constituting the second part of this work unambiguously demonstrate that the surface monolayer at the multilayer-air interface is disordered. Conversely, the monolayer at the OTS-glass substrate surface, as well as all interior monolayers in the multilayer are well-ordered.

This result is not surprising when one considers that the OTS hydrocarbon chain is very similar (on a macromolecular level) to that of arachidic acid. Deposition of the first monolayer onto the glass-OTS surface should not be very different (with respect to inter-molecular forces between monolayers) than depositing the third monolayer onto the second, or the fifth onto the fourth, *et cetera*. The last monolayer is not constrained by the terminal methyl groups of a juxtaposed monolayer. The chain terminal methyl groups of the last monolayer interface with air; consequently these chains appear to have more degrees of freedom than the chain terminal methyl groups of the internal monolayers in the multilayer.

## CHAPTER SEVEN: CONCLUSION

The box refinement technique is a very powerful method for solving the phase problem in structures which are of finite extent. Unfortunately, box refinement alone generally cannot provide a unique phase solution which satisfies the box refinement constraint of zero electron density contrast outside the box for asymmetric structures [1-22, 1-23]. Usually some additional criteria must also be used. Applying the box refinement techniques to series of homologous multilayers allows one to confidently establish the correct electron density profile.

The  $N = 1, 2, 3$  arachidic acid multilayers provide a homologous series for the box refinement technique. That three vastly different corrected intensity functions  $I_o(q_z)$  refined to quantitatively analogous multilayer electron density profiles is strong evidence that the refinement did indeed converge to the correct solution in each case. Furthermore, a mathematically simple and physical-chemically reasonable model has been constructed for the arachidic acid  $N = 2$  case which further clarifies the box refinement result. Additional evidence supporting the validity of the box refinement solutions comes from the fact that the results are consistent with the average bilayer electron density profiles derived from the deconvolution of the multilayer Patterson function  $P_{m1}(z)$ . The Patterson function deconvolution technique employing the Fourier synthesis gives bilayer profile structures which represent the average structure of the bilayer ensemble. As the number of bilayers decreases, the

average bilayer electron density profile becomes more sensitive to perturbations in any given bilayer. It is therefore consistent that the average bilayer electron density profile for the arachidic acid  $N = 2, 3$  and  $5$  represents a more well-ordered system as  $N$  increases, if the number of perturbed bilayers (or monolayers) in the multilayer remains constant.

The Patterson deconvolution technique can lead to an erroneous conclusion concerning the multilayer electron density profiles of the arachidic acid multilayers; namely, that as the number of bilayers decrease, the multilayer as a whole disorders. The box refinement procedure demonstrated that only the last monolayer was in fact disordered. This shows that the assumption used in the Patterson function deconvolution technique (the existence of a repeated unit cell or bilayer) was incorrect. The Patterson function deconvolution was limited in that it could only produce the electron density profile of the average unit cell.

From the arachidic acid multilayer study alone it is impossible to conclusively determine whether the first fatty acid monolayer (juxtaposed with the glass-OTS substrate) or the last surface monolayer (interfaced with air) in the monolayer deposition sequence was responsible for the broad methyl trough feature at one edge of the multilayer electron density profiles. It simply demonstrated that on a macromolecular scale, one monolayer at one edge of the multilayer profile was consistently disordered; all other monolayers in the multilayers containing one, two, three and five bilayers were



well-ordered. By systematically varying the chain length of the fatty acid molecules in the different monolayers of the multilayer, the second study was able to prove that the last or surface monolayer in the deposition sequence was indeed the disordered monolayer. In addition, when the last deposited monolayer was chemically removed (DDDA versus DDD) , the multilayer electron density profile no longer exhibited the broad methyl trough feature at one end. Since the multilayer films were non-periodic, standard structural methods which rely on the repetition of an average structural unit could not be employed. The corefinement technique is effectively the real space analog of holographic interferometry described previously [7-1]. It utilizes the reasonable physical-chemical constraint that the multilayer structures in the homologous series remain invariant over a specified region in real space; it does not however make any a priori assumptions as to the nature of the invariant portion of the electron density profiles.

The arachidic acid multilayer study coupled with the mixed monolayer study necessarily leads to the conclusion that the surface monolayer of an amphiphilic molecule at the multilayer-air interface in Langmuir-Blodgett multilayer thin films can be ordered by the deposition of another bilayer (or monolayer). This overlayer-induced ordering of the underlying monolayer is not only interesting in statistical mechanical terms concerning relevant physical interactions between the different monolayers in the multilayer, but it must also be considered in the fabrication of stable Langmuir-Blodgett

multilayer films where intramolecular/intermolecular ordering within a monolayer is critical for device applications [7-2].

The Langmuir-Blodgett technique is a very powerful tool in creating multilayer systems composed of a finite number of monolayers, each of a defined chemical composition. X-ray diffraction can now be used to probe the structure of such multilayer systems, even to the level of one bilayer or individual monolayer. The box refinement and corefinement techniques (provided one uses a homologous series of multilayers) can yield excellent results in determining the multilayer electron density profiles for each of the series in the absence of the stringent requirement that the multilayer be composed of a finite number of repeated symmetric units, e.g. symmetric bilayers, bilayer pairs, *et cetera*.

The auxiliary maxima observed in the meridional diffraction data can be well resolved by improving  $\Delta q_z$  resolution. This requires improved detector spatial resolution and x-ray optics, or requires an increase in specimen to detector distance with focusing x-ray optics. The latter generally necessitates either greater x-ray flux or extended total exposure time to maintain the statistical accuracy of the data. Improving both the statistical accuracy of the data and the  $\Delta q_z$  resolution of the experimental system is essential in the structural study of multilayer thin films by x-ray diffraction techniques since the methods of data analysis employed depend critically on these parameters.

**REFERENCES FOR CHAPTER SEVEN**

- [7-1] Lesslauer, W., Blasie, J.K. X-Ray Holographic Interferometry in the Determination of Planar Multilayer Structures. Theory and Experimental Observations. *Acta Cryst* A27:456-461 (1970)
- [7-2] Garito, A.F., Singer, K.D. Organic Crystals and Polymers — A New Class of Nonlinear Optical Materials. *Laser Focus* 18:59-63 (1982)

CHAPTER EIGHT: THE STUDY OF THIN MULTILAYER FILMS — A DISCUSSION OF  
A BIOPHYSICAL APPLICATION

McConnell has utilized lipid monolayers attached to planar glass surfaces by the Langmuir-Blodgett technique to study the specific binding and triggering of cellular components of the immune system. His work has been motivated by a desire to use well-defined planar model membranes as surfaces with controlled physical and chemical properties which serve as a target for specific cell surface recognition studies.

Specifically, McConnell studied the binding of guinea pig peritoneal macrophages to supported planar lipid monolayers. He fabricated planar lipid monolayers supported on alkylated glass containing one mole per cent of a lipid hapten (dipalmitoyl phospholipid nitroxide hapten I) [1-16]. A hapten is a small molecule which is only immunologically active in the presence of an existing specific antibody; it is unable to trigger antibody synthesis *in situ* [8-1]. The monolayers were either "fluid" in the layer plane when DMPC (dimyristoyl phosphatidylcholine) was used in their preparation, or "solid" when DPPC (dipalmitoyl phosphatidylcholine) was employed. The binding affinity of the macrophage to the hapten is increased by three to four orders of magnitude when a specific anti-hapten immunoglobulin of the class IgG is bound to the lipid hapten. The IgG antigen specific antibody mediates or triggers the response of the macrophage to the antigen (hapten) by binding to surface receptors on the macrophage.

The structural nature of the interaction between the monolayer membrane and the macrophage membrane is basic to the study of the mechanisms of membrane-membrane interactions in the immune system. Understanding the changes in the macrophage membrane structure when IgG is bound both to the lipid hapten and to the surface receptors of the macrophage is important for elucidating the mechanism by which immunoglobulins trigger intracellular components during an immune response. Both of these biological problems, namely the mechanism of membrane-membrane interactions and the mechanism of the response of membranes to extracellular mediation, are therefore strongly structural in nature.

McConnell found that the cellular response of the guinea pig peritoneal macrophages to the supported lipid monolayers to be both qualitatively and quantitatively similar to the response of macrophage binding to lipid hapten containing vesicles [1-16]. He concluded that supported planar monolayer were indeed a good model system for studying the binding and triggering of the cellular components of the immune system.

The use of supported planar multilayers or monolayers are also ideal for structural studies of the membrane-membrane interaction between the macrophage and monolayer membranes since they can be utilized to orient the macrophage membrane for x-ray scattering measurements. The work in this thesis demonstrated that meridional (out of plane) scattering from as few as two molecular monolayers can be collected and analyzed to provide the electron density profile of

each monolayer provided sufficient statistics can be obtained over a range of  $q_z \leq (q_z)_0$ , which determines the spatial resolution in the derived profile. For biological samples, this could easily be accomplished by using the increased flux of a synchrotron x-ray source. The additional flux would allow measurements of equatorial (in plane) scattering, which would provide information about correlations in the planes parallel to the monolayer surface [8-2]. This would facilitate measurements of the chain tilt of the lipids with respect to the monolayer surface normal and membrane fluidity.

Meridional x-ray scattering data from supported planar lipid multilayers or monolayers with a single layer of bound macrophage membrane could be phased by refinement techniques provided there was a reference structure available. This reference structure would simply be a supported planar lipid multilayer without bound macrophage. The reference structure and the macrophage bound lipid multilayer would be a homologous series. Hence the profile structure of the multilayer and the multilayer with the attached macrophage membrane could be accurately determined as a function of changes in either the lipid hapten monolayer (on the multilayer surface) and/or the macrophage membrane upon forming the monolayer-membrane "complex".

Thus, thin multilayer films attached to planar surfaces can not only be used to study membrane-membrane interactions and the triggering of cellular components of the immune system [1-16], they can also be used as a powerful tool in the structural study of the

membranes in the membrane-membrane interaction and the triggering mechanism since they can greatly facilitate both the collection and phasing of the x-ray scattering data.

**REFERENCES FOR CHAPTER EIGHT**

- [8-1] Roitt, I. *Essential Immunology*, Blackwell Scientific Publishing, Inc., 1980.
- [8-2] Seul, M., Eisenberger, P., McConnell, H.M. X-ray Diffraction by Phospholipid Monolayers on Single-Crystal Silicon Substrates. *PNAS* 80:5795-5797 (1983)



**APPENDIX I: FOURIER TRANSFORM OF AN INFINITE PERIODIC ARRAY OF DELTA FUNCTIONS**

An infinite array of delta functions of periodicity  $d$  can be expressed as follows:

$$\rho(z) = \sum \delta(z - \ell d) \quad (\text{AI-1})$$

It's Fourier transform is given by:

$$F(q_z) = \int \sum_{-\infty}^{+\infty} \delta(z - \ell d) \exp[2\pi i z q_z] dz \quad (\text{AI-2})$$

Evaluating the integral yields:

$$\begin{aligned} F(q_z) &= \sum_{-\infty}^{+\infty} \exp[2\pi i \ell d q_z] \\ &= \sum_{-\infty}^{+\infty} \exp[2\pi i d q_z]^\ell \end{aligned} \quad (\text{AI-3})$$

Equation (AI-3) can be expanded in terms of two similar sums:

$$\begin{aligned} F(q_z) &= \sum_0^{+\infty} \exp[2\pi i d q_z]^\ell + \sum_0^{+\infty} \exp[2\pi i d q_z]^{-\ell} - 1 \\ &= \sum_0^{+\infty} \exp[2\pi i d q_z]^\ell + \sum_0^{+\infty} \exp[-2\pi i d q_z]^\ell - 1 \end{aligned} \quad (\text{AI-4})$$

Utilizing the power series of equation (AI-5):

$$\frac{1}{1 - \xi} = 1 + \xi + \xi^2 + \xi^3 + \xi^4 + \dots \quad (\text{AI-5})$$

for  $\xi = \exp[2\pi i d q_z]$  and  $\xi = \exp[-2\pi i d q_z]$  yields:

$$F(q_z) = \frac{1}{1 - \exp[2\pi i d q_z]} + \frac{1}{1 - \exp[-2\pi i d q_z]} - 1 \quad (\text{AI-6})$$

Evaluating (AI-6) yields  $F(q_z)$ :

$$\begin{aligned} F(q_z) &= 0 && \text{for } \exp[*2\pi i d q_z] \neq 1 \\ &\rightarrow \infty && \text{for } \exp[*2\pi i d q_z] = 1 \end{aligned}$$

The singularities are periodic and occur when:

$$2\pi d q_z = 2\pi \ell \quad (\ell = \text{integer})$$

$$q_z = \frac{\ell}{d}$$

Thus,  $F(q_z)$  tends to infinity at integer multiple of  $1/d$ . We can therefore utilize the delta in expressing  $F(q_z)$ .

$$F(q_z) = \frac{1}{d} \sum_{-\infty}^{+\infty} \delta(q_z - \ell/d) \quad (\text{AI-7})$$

The factor  $1/d$  is to provide the proper normalization. Generally since we deal with only relative quantities, the  $1/d$  is dropped for convenience.

QED

APPENDIX II: SHIFTING OF DIFFRACTION MAXIMA FOR MULTILAYERS OF  
FINITE EXTENT

Taking the derivative of equation (II-56), assuming  $W(q_z) = \delta(q_z)$  yields

$$\frac{dI}{dq_z} = 2F_{uc} \cdot L_n \left[ F_{uc} \cdot \frac{dL_n}{dq_z} + \frac{dF_{uc}}{dq_z} \cdot L_n \right] \quad (\text{AII-1})$$

For  $I(q_z)$  to be a maximum requires

$$F_{uc} \cdot \frac{dL_n}{dq_z} + \frac{dF_{uc}}{dq_z} \cdot L_n = 0 \quad (\text{AII-2})$$

Evaluating (AII-2) for  $q_z = \lambda/d$  yields:

$$\frac{dF_{uc}}{dq_z} \cdot L_n = 0 \quad (\text{AII-3})$$

since  $dL_n/dq_z = 0$  for  $q_z = \lambda/d$  if  $L_n$  to be a maximum at  $q_z = \lambda/d$  (II-57).

Therefore if  $dF_{uc}/dq_z = 0$  (ie.  $F_{uc}$  is a maximum) at  $q_z = \lambda/d$  the diffraction maxima will not be shifted from the Bragg limit position and will occur at the  $q_z = \lambda/d$ . If  $dF_{uc}/dq_z < 0$  for  $q_z = \lambda/d$  the diffraction maximum will be shifted to higher  $q_z$ ; conversely, if  $dF_{uc}/dq_z > 0$  at  $q_z = \lambda/d$  the diffraction maximum will be shifted to lower  $q_z$ .

**APPENDIX III: RECONSTRUCTION OF THE UNIT CELL PATTERSON BY THE  
METHOD OF LINEAR EQUATIONS**

If one assumes a profile structure to be composed of a repeating subunit (ie. unit cell) it is possible to reconstruct the unit cell Patterson function from the multilayer Patterson function. Equation (II-58) (assuming  $w(z) = 1$ ) can be written to yield:

$$\begin{aligned} P_{m1}(z) &= [\rho_{uc}(z) * l(z)] * [\rho_{uc}(-z) * l(-z)] \\ &= [\rho_{uc}(z) * \rho_{uc}(-z)] * [l(z) * l(-z)] \\ &= P_{uc}(z) * \tilde{l}^2(z) \end{aligned} \quad (\text{AIII-1})$$

For  $P_{uc}(z) = 0$  for  $|z| > d$

$$\text{and } \tilde{l}^2(z) = \sum_{-\infty}^{+\infty} \delta(z-nd) \cdot [b(z) * b(-z)]$$

$$\text{with } \begin{array}{ll} b(z)=1 & -Nd/2 \leq z \leq Nd/2 \\ b(z)=0 & \text{otherwise} \end{array}$$

$N =$  number of unit cells

If  $0 < \beta < d$  and  $W_k = P_{m1}(kd)$  where  $k$  is an integer such that  $0 < k < +N$  then:

$$P_{m1}(kd+\beta) = W_k P_{uc}(\beta) + W_{k+1} P_{uc}(d-\beta) \quad (\text{AIII-2})$$

Equation (AIII-2) simply states that the multilayer Patterson function at any point is just the weighted sum of the unit cell Patterson function at  $z=\beta$  and  $z=d-\beta$ . The weighting factor arises from the autocorrelation of the box function,  $b(z)$ , and can be taken as the magnitude of the local maxima of the multilayer Patterson

function at  $z = kd$ .

For  $\beta \rightarrow d - \beta$  equation (AIII-2) yields:

$$P_{m1}(kd+d-\beta) = W_k P_{uc}(d-\beta) + W_{k+1} P_{uc}(d-d+\beta) \quad (\text{AIII-3})$$

Solving (AIII-2) and (AIII-3) for  $P_{uc}(d-\beta)$  and  $P_{uc}(\beta)$  yields:

$$P_{uc}(d-\beta) = \frac{W_k P_{m1}([k+1]d-\beta) - W_{k+1} P_{m1}(kd+\beta)}{W_k^2 - W_{k+1}^2} \quad (\text{AIII-4})$$

$$P_{uc}(\beta) = \frac{W_k P_{m1}(kd+\beta) - W_{k+1} P_{m1}([k+1]d-\beta)}{W_k^2 - W_{k+1}^2} \quad (\text{AIII-5})$$

where  $W_k = P_{m1}(kd)$  and  $W_{k+1} = P_{m1}([k+1]d)$ .

A special case is when  $k = N$ . Then  $W_{k+1} = 0$  and (AIII-4) and (AIII-5) reduce to:

$$P_{uc}(d-\beta) = \frac{P_{m1}([k+1]d-\beta)}{W_k} \quad (\text{AIII-6})$$

$$P_{uc}(\beta) = \frac{P_{m1}(kd+\beta)}{W_k} \quad (\text{AIII-7})$$

This proves that the unit cell Patterson function is just the multilayer Patterson function over the interval  $Nd$  to  $[N+1]d$  divided by  $W_k$ .

Equations (AIII-2) through (AIII-7) are valid for  $-N < k < 0$  with the provision that  $k+1$  goes to  $k-1$ . This is of course is a consequence of the fact that Patterson functions are symmetric.

Theoretically it is possible to determine the unit cell Patterson over any interval, however the best statistics are obtained over the

first interval, namely  $k=0$ . Equations (AIII-6) and (AIII-7) show it is possible to determine the unit cell Patterson by inspection alone; unfortunately, the statistics for the interval defined by  $k= *N$  are poor.

#### APPENDIX IV: DIRECT DECONVOLUTION METHOD

This method can be applied to deconvolute either the multilayer electron density profile from the multilayer Patterson, or the unit cell electron density profile from the unit cell Patterson. Therefore no subscripts denoting unit cell or multilayer have been included.

Let us begin with the definition of the Patterson (or autocorrelation) function (II-42):

$$P(z) = \rho(z) * \rho(-z) \quad (\text{AIV-1})$$

where  $\rho(z) = 0 \quad |z| > d/2$   
and  $P(z) = 0 \quad |z| > d$

Note,  $P(z)=P(-z)$  must always be true. This is obvious from equation (AIV-1).

By definition equation (AIV-1) yields:

$$P(z) = \int_{-\infty}^{+\infty} \rho(u) \rho(u+z) du$$

Since  $\rho(z)$  and  $P(z)$  are finite:

$$P(z) = \int_{-d}^{+d} \rho(u) \rho(u+z) du \quad (\text{AIV-2})$$

Rewriting the integral as a sum yields

$$P(z) = \sum_{n=-\ell}^{+\ell} \rho(n\Delta u) \rho(n\Delta u+z) \Delta u \quad (\text{AIV-3})$$

where  $\ell = d/2\Delta u$   
and  $\Delta u \neq 0$

If we let  $z = -d + k\Delta u$

$$P(-d + k\Delta u) = \sum_{n=-\ell}^{+\ell} \rho(n\Delta u) \rho([n+k]\Delta u-d) \Delta u \quad (\text{AIV-4})$$

where  $k$  ranges from 0 to  $2d/\Delta u$ .

There are  $2\ell+1$  terms in the above sum for each  $P$ ; however equation (AIV-4) can be reduced to include only non-trivial terms.

$$P(-d + k\Delta u) = \sum_{n=\ell-k}^{+\ell} \rho(n\Delta u) \rho([n+k]\Delta u-d) \Delta u \quad (\text{AIV-5})$$

$\rho(n\Delta u)$  is zero for  $n > \ell$ ; likewise,  $\rho([n+k]\Delta u-d)$  is zero for  $n < \ell-k$ .

For  $k = 0$ , (AIV-5) yields:

$$P(-d) = \rho(\ell\Delta u) \rho([\ell\Delta u]-d)$$

since  $\ell = d/2\Delta u$

$$P(-d) = \rho(d/2) \rho(-d/2) \quad (\text{AIV-6})$$

Assuming  $\rho$  is symmetric, allows us to solve for  $\rho(\mp d/2)$ :

$$\rho(\mp d/2) = \pm \sqrt{P(d)} \quad (\text{AIV-7})$$

In general for  $k \neq 0$ , from equation (AIV-5) we have:



$$P(-d + k\Delta u) = \sum_{n=\ell-k}^{\ell-1} \rho(n\Delta u) \rho([n+k]\Delta u-d) \Delta u + \rho(\ell\Delta u) \rho([\ell+k]\Delta u-d) \Delta u \quad (\text{AIV-8})$$

and solving for  $k=1$ , with  $\ell=d/2\Delta u$  yields:

$$\begin{aligned} P(-d+\Delta u) &= \rho(-d/2+\Delta u) \rho(d/2) \Delta u + \rho(d/2-\Delta u) \rho(-d/2) \Delta u \\ \rho(\mp d/2\pm\Delta u) &= \frac{P(-d+\Delta u)}{2\rho(\pm d/2)\Delta u} \end{aligned} \quad (\text{AIV-9})$$

For  $k \neq 0,1$  equation (AIV-5) yields:

$$P(-d + k\Delta u) = \sum_{n=\ell-k+1}^{\ell-1} \rho(n\Delta u) \rho([n+k]\Delta u-d) \Delta u + \rho(\ell\Delta u) \rho([\ell+k]\Delta u-d) \Delta u + \rho([\ell-k]\Delta u) \rho(\ell\Delta u-d) \Delta u$$

since  $\ell=d/2\Delta u$

$$P(-d + k\Delta u) = \sum_{n=\ell-k+1}^{\ell-1} \rho(n\Delta u) \rho([n+k]\Delta u-d) \Delta u + \rho(d/2) \rho(-d/2+k\Delta u) \Delta u + \rho(d/2-k\Delta u) \rho(-d/2) \Delta u$$

$$P(-d + k\Delta u) = \sum_{n=\ell-k+1}^{\ell-1} \rho(n\Delta u) \rho([n+k]\Delta u-d) \Delta u + 2\rho(\pm d/2) \rho(\mp d/2 \pm k\Delta u) \Delta u$$

$$\rho(\mp d/2 \pm k\Delta u) = \frac{\left[ P(-d+k\Delta u) - \sum_{n=\ell-k+1}^{\ell-1} \rho(n\Delta u) \rho([n+k]\Delta u-d) \Delta u \right]}{2\rho(\pm d/2)\Delta u} \quad (\text{IV-10})$$

Given a finite Patterson function (and consequently a finite electron density profile) it is possible to directly deconvolute the Patterson function, assuming the electron density profile is symmetric (see equation (AIV-7) above). However, this method is a recursive technique (equations (AIV-9) and (AIV-10)) and propagates errors rapidly. Generally, the direct deconvolution method is not used to deconvolute the multilayer Patterson function since there is too much uncertainty in the multilayer Patterson function at  $z \sim \pm d$ ; there is no theoretical reason why it could not be done however.

APPENDIX V: FOURIER SYNTHESIS OF THE ELECTRON DENSITY PROFILE

Rewriting equation (II-38) for a multilayer yields:

$$\rho_{m1}(z) = \int_{-\infty}^{+\infty} F_{m1}(q_z) \exp[2\pi i q_z z] dq_z \quad (\text{AV-1})$$

where

$$|F_{m1}(q_z)|^2 = |F_{uc}(q_z)|^2 \cdot |L_n(q_z)|^2 * W(q_z)$$

From equation (II-56) we have simply that

$$I(q_z) = |F_{m1}(q_z)|^2$$

or

$$|F_{m1}(q_z)| = \sqrt{I(q_z)} \quad (\text{AV-2})$$

Additionally

$$F_{m1}(q_z) = |F_{m1}(q_z)| \exp[i\phi(q_z)]$$

where  $\phi(q_z)$  is the phase function.

If we assume  $\rho_{m1}(z)$  to be centrosymmetric

$$\rho_{m1}(z) = \rho_{m1}(-z)$$

then  $\phi(q_z)$  can have values of only 0 or  $\pi$ . Thus equation (1), after substituting (AV-2) and (AV-3) becomes:

$$\rho_{m1}(z) = 2 \int_{-\infty}^{+\infty} \pm \sqrt{I(q_z)} \cos(2\pi q_z z) dq_z \quad (\text{AV-4})$$

For  $F_{m1}(q_z)$  to be a continuous function,  $\phi(q_z)$  can only change from  $0 \rightarrow \pi$  or from  $\pi \rightarrow 0$  when  $F_{m1}(q_z) = 0$ ; otherwise  $F_{m1}(q_z)$  would be a

multivalued function. Thus the number of possible phase combinations is  $2^{\ell}$  where  $\ell$  is the number of observed diffraction maxima. Since half of the solutions differ by a shift in the z-origin by  $d/2$  ( $d$  = unit cell translation vector projected onto the z-axis), the effective number of solutions is  $2^{\ell-1}$ .

The Fourier synthesis outlined above does not solve for  $\phi(q_z)$  but is only a prescription for possible phase combinations. Generally, the number of possible phase combination is infinite; it is only because we assume  $\rho_m(z)$  to be centrosymmetric that we are able to limit the number of possible phase combinations to  $2^{\ell}$ .

## APPENDIX VI: BOX REFINEMENT TECHNIQUE

The box refinement technique is an iterative procedure for calculating the phase solution for finite systems. The background and Lorentz- $q_z$  corrected intensity function for a multilayer of finite size or extent exhibits a broadening and shifting of diffraction maxima from the Bragg (i.e. infinite extent) limit. Auxiliary maxima may also be observed; the number and position of which depend on the number of monolayers in the multilayer as well as the experimental system  $\Delta q_z$  resolution. These features in the intensity function,  $I(q_z)$ , which are attributed to the finite size of the multilayer contain the information which the box refinement technique needs to converge to a phase solution. The modulus of the structure factor,  $|F(q_z)|$ , is given by the square root of the corrected intensity function:

$$|F(q_z)| = \sqrt{I_{\text{cor}}(q_z)} \quad (\text{AVI-1})$$

One chooses a trial multilayer electron density function,  $\rho_0(z)$ , and calculates its Fourier transform (equation AVI-2). After some simple algebra (equations AVI-3 and AVI-4) we are left with the expressions for the cosine and sine of the trial phase (equations AVI-5 and AVI-6, respectively). The subscript  $n$  refers to the iteration index; it is zero for  $\phi_n(q_z)$  calculated from the trial electron density profile.

$$F_n(q_z) = \int \rho_n(z) \exp[2\pi i q_z z] dz \quad (\text{AVI-2})$$

$$\begin{aligned}
&= \int \rho_n(z) \cos[2\pi q_z z] dz + \\
&\quad i \int r_n(z) \sin[2\pi q_z z] dz \\
&= |F_n(q_z)| \exp[i\phi_n(q_z)]
\end{aligned}$$

$$\begin{aligned}
\therefore |F_n(q_z)|^2 &= \left[ \int \rho_n(z) \cos[2\pi q_z z] dz \right]^2 + \\
&\quad \left[ \int \rho_n(z) \sin[2\pi q_z z] dz \right]^2 \quad (\text{AVI-3})
\end{aligned}$$

and

$$\phi_n(q_z) = \tan^{-1} \left[ \frac{\int \rho_n(z) \sin [2\pi q_z z] dz}{\int \rho_n(z) \cos [2\pi q_z z] dz} \right] \quad (\text{AVI-4})$$

with

$$\cos[\phi_n(q_z)] = \left[ \frac{\int \rho_n(z) \cos [2\pi q_z z] dz}{|F(q_z)|} \right] \quad (\text{AVI-5})$$

$$\sin[\phi_n(q_z)] = \left[ \frac{\int \rho_n(z) \sin [2\pi q_z z] dz}{|F(q_z)|} \right] \quad (\text{AVI-6})$$

The multilayer electron density profile is just the inverse Fourier transform of the structure factor (AVI-7).  $|F(q_z)|$  is known (AVI-1); we substitute  $\phi_n(q_z)$  for  $\phi(q_z)$  and calculate  $\rho_{n+1}(z)$  (AVI-8).

$$\rho_{m1}(z) = \int F(q_z) \exp[-2\pi i q_z z] ds \quad (\text{AVI-7})$$

$$\begin{aligned}
\text{where } F(q_z) &= |F(q_z)| \exp[i\phi(q_z)] \\
\text{and } \phi(q_z) &= \text{unknown phases}
\end{aligned}$$

$$\rho_{n+1}(z) = \int F'_n(q_z) \exp[-2\pi i q_z z] ds \quad (\text{AVI-8})$$

where  $F'_n(q_z) = |F(q_z)| \exp[i\phi_n(q_z)]$   
and  $\phi_n(q_z) =$  phases derived from  $\rho_n(z)$

After some algebra, (AVI-8) yields (AVI-9):

$$\begin{aligned} \rho_{n+1}(z) = & \int |F(q_z)| \cos[\phi_n(q_z)] \cos 2\pi q_z z ds + \\ & i \int |F(q_z)| \sin[\phi_n(q_z)] \cos 2\pi q_z z ds + \\ & \int |F(q_z)| \sin[\phi_n(q_z)] \sin 2\pi q_z z ds + \\ & i \int |F(q_z)| \cos[\phi_n(q_z)] \sin 2\pi q_z z ds \end{aligned}$$

$$\begin{aligned} \rho_{n+1}(z) = & \int |F(q_z)| \cos[\phi_n(q_z)] \cos 2\pi q_z z ds + \\ & \int |F(q_z)| \sin[\phi_n(q_z)] \sin 2\pi q_z z ds \end{aligned}$$

$$\rho_{n+1}(z) = \rho_{S_{n+1}}(z) + \rho_{A_{n+1}}(z) \quad (\text{AVI-9})$$

where  $\rho_{S_{n+1}}(z) = \int |F(q_z)| \cos[\phi_n(q_z)] \cos 2\pi q_z z ds$

$$\rho_{A_{n+1}}(z) = \int |F(q_z)| \sin[\phi_n(q_z)] \sin 2\pi q_z z ds$$

and  $\cos[\phi_n(q_z)], \sin[\phi_n(q_z)]$  are given by (AVI-5) and (AVI-6).

Note,  $\rho_{S_{n+1}}(z)$  is the cosine or symmetric Fourier transform of  $F'_n(q_z)$ ;  $\rho_{A_{n+1}}(z)$  is the sine or antisymmetric Fourier transform of  $F'_n(q_z)$ . We now apply the box constraint to  $\rho_{n+1}(z)$  (AVI-10). We demand that  $\rho_{n+1}(z)$  be zero outside some box,  $\beta(z)$ . The width of this box must at least be the size or extent of the multilayer. This minimum box width is determined from the multilayer Patterson function and is given by  $z = Z$  where  $P_{m1}(Z) \rightarrow 0$ .

$$\rho_{n+1}^+(z) = \rho_{n+1}(z) \cdot \beta(z) \quad (\text{AVI-10})$$

$$\text{where } \beta(z) = 1 \text{ for } \beta_1 < z < \beta_2$$

$$\beta(z) = 0 \text{ otherwise}$$

$$\text{and } |z| \leq \beta_2 - \beta_1$$

$\rho_{n+1}^+(z)$  is substituted for  $\rho_n(z)$  in equation (AVI-2) and the process is iterated until:

$$\rho_{n+1}(z) = \rho_n(z) \quad (\text{AVI-11})$$

or

$$\rho_{n+1}^+(z) = \rho_{n+1}(z) \quad (\text{AVI-12})$$

Equation (AVI-11) states that the refinement is complete when two subsequent iterations give the same  $\rho(z)$ ; equation (AVI-12) emphasizes that this will occur when  $\rho_{n+1}(z)$  iterates to be zero for  $z < \beta_1$  and  $z > \beta_2$ .



**APPENDIX VII: SYMMETRIC AND ANTISYMMETRIC CONTRIBUTIONS OF THE  
ELECTRON DENSITY PROFILE TO THE INTENSITY FUNCTION**

The electron density profile can always be split into its symmetric component,  $\rho_S(z)$ , and its antisymmetric component,  $\rho_A(z)$ :

$$\rho(z) = \rho_S(z) + \rho_A(z) \quad (\text{VII-1})$$

where  $\rho_S(z) = \rho_S(-z)$

and  $\rho_A(z) = -\rho_A(-z)$

The Fourier transform of (VII-1) yields the structure factor (VII-2) from which the intensity function (VII-3) can be calculated:

$$\begin{aligned} f(q_z) &= \int \left[ \rho_S(z) + \rho_A(z) \right] \exp[2\pi i q_z z] dz \\ &= \int \rho_S(z) \cos 2\pi q_z z dz + i \int \rho_A(z) \sin 2\pi q_z z dz \end{aligned} \quad (\text{VII-2})$$

$$I(q_z) = \int \left[ \rho_S(z) \cos 2\pi q_z z dz \right]^2 + \int \left[ \rho_A(z) \sin 2\pi q_z z dz \right]^2$$

$$I(q_z) = I_S(q_z) + I_A(q_z) \quad (\text{VII-3})$$

The square of the cosine transform of the electron density profile is called the symmetric intensity function,  $I_S(q_z)$ , while the square of the sine transform of the electron density profile is called the ant-symmetric intensity function  $I_A(q_z)$ . The intensity function,  $I(q_z)$  is just the sum of the symmetric and antisymmetric functions.

## BIBLIOGRAPHY

- Ashcroft, N.W., Mermin, N.D., *Solid State Physics*, Holt, Rinehart and Winston, 1976.
- Baym, G., *Lectures on Quantum Mechanics*, Benjamin/Cummings Publishing Company, 1978.
- Blodgett, K. Monomolecular Films of Fatty Acids on Glass. *JACS*. 56:495 (1934)
- Blodgett, K. Successive Monomolecular Layers on a Solid Surface. *JACS*. 57:1007-1022 (1935)
- Blodgett, K., Langmuir, I. Built-up Films of Barium Stearate and thier Optical Properties. *Physical Review*. 51:964-982 (1937)
- Clark, G., Leppla, P. X-ray Diffraction Studies of Built-up Films. *JACS*. 58:2199-2201 (1936)
- Clark, G., Sterrett, R., Leppla, P. X-ray Diffraction Studies of Built-up Films of Long-Chain Compounds. *JACS*. 56:495-496 (1934)
- Coley, J.M., *Diffraction Physics*, North-Holland Publishing Company, 1981.
- Ehrenberg, W., Franks, A. Small-Angle X-Ray Scattering. *Nature* 170:1076-1077 (1952)
- Franks, A. An Optically Focusing X-Ray Diffraction Camera. *Proc. Phys. Soc. B* 68:1054-1064 (1955)
- Gabriel, A. Position Sensitive X-Ray Detector. *Rev. Sci. Instrum.* 48:1303-1305 (1977)
- Gabriel, A., DuPont, Y. A Position Sensitive Proportional Detector for X-Ray Crystallography. *Rev. Sci. Instrum.* 43: 1600-1602 (1972)
- Garito, A.F., McGhie, A.R., Kalyanaraman, P.S. Kinetics of Solid State Polymerization of 2,4-Hexadiyne-1,6-Diol-Bis (P-Toluene Sulfonate) in *Molecular Metals*, W. Hatfield, ed., Plenum Publishing (1979)

- Garito, A.F., Singer, K.D. Organic Crystals and Polymers — A New Class of Nonlinear Optical Materials. *Laser Focus* 18:59-63 (1982)
- Gruner, S.M., Milch, J.R., Reynolds, G.T. Slow-Scan Silicon-Intensified Target-TV X-Ray Detector for Quantitative Recording of Weak X-Ray Images. *Rev. Sci. Instrum.* 53:1770-1778 (1982)
- Hafeman, D., Tscherner, V., McConnell, H. Specific Antibody-Dependent Interactions between Macrophages and Lipid Haptens in Planar Lipid Monolayers. *PNAS* 78:4552-4556 (1981)
- Holley, C., Bernstein, S. X-ray Diffraction by a Film of Counted Molecular Layers. *Phys. Rev.* 49:403 (1936)
- Hoseman, R., Bagchi, S.N., *Direct Analysis of Diffraction by Matter*, North-Holland Publishing Company, 1962.
- Kopp, F., Cuendet, P., Mühlethaler, K., Zuber, H. Hydrophobic Membrane Protein from Chromatophores of *Rhodospirillum Rubrum*. Structural and Spectroscopic Studies of Monolayers and Multilayers. *BBA* 553:438-449 (1979)
- Langmuir, I., Schaefer, V. Activities of Urease and Pepsin Monolayers. *JACS* 60:135[1-1357 (1938)
- Langmuir, I., Schaefer, V. Improved Methods of Conditioning Surfaces for Adsorption. *JACS* 59:1762-1763 (1937)
- Langmuir, I., Schaefer, V. Optical Measurements of the Thickness of a Film Adsorbed From a Solution. *JACS* 59:1406 (1937)
- Langmuir, I., Schaefer, V., Wrinch, D. Built-up Films of Proteins and their Properties. *Science* 85:76-80 (1937)
- Lesslauer, W., Blasie, J.K. Direct determination of the Structure of Barium Stearate Multilayers by X-ray Diffraction. *Biophys. J.* 12:175-190 (1972)
- Lesslauer, W., Blasie, J.K. X-Ray Holographic Interferometry in the Determination of Planar Multilayer Structures. Theory and Experimental Observations. *Acta Cryst* A27:456-461 (1970)
- Lesslauer, W., Cain, J., Blasie, J.K. On the Location of 1-Anilo-8-Naphthalene-Sulfonate in Lipid Model Systems. *BBA* 241:547-566 (1971)

- Levine, Y.K., Wilkins, M.H.F. Structure of Oriented Lipid Bilayers. *Nature New Biology* 230:69-72 (1971)
- Makowski, L. The Use of Continuous Diffraction Data as a Phase Constraint. I. One-Dimensional Theory. *J. Appl. Cryst.* 14: 160-168 (1981)
- McIntosh, T., Waldbillig, R., Robertson, D. Lipid Bilayer Ultrastructure Electron Density Profiles and Chain Tilt Angles as Determined by X-ray Diffraction. *BBA* 448:15-33 (1976)
- McLean, L., Durrani, A., Whittam, M., Johnston, D., Chapman, D. Preparation of Stable Polar Surfaces Using Polymerizable Long-Chain Diacetylene Molecules. *Thin Solid Films* 99:127-131 (1983)
- Merzbacher, E., *Quantum Mechanics*, John Wiley and Sons, 1970.
- Milch, J.R. Slow Scan SIT Detector for X-Ray Diffraction Studies Using Synchrotron Radiation. *IEEE Trans. Nucl. Sci.* NS-26:338-341 (1979)
- Müller, A. The X-ray Investigation of Fatty-Acids. *J. Chem Society.* 123:2043-2047 (1923)
- Müller, A., Shearer, G. Further X-Ray Measurements of Long-chain Compounds and a Note on their Interpretation. *J. Chem Society.* 123:3156-3164 (1923)
- Packham, N., Dutton, P.L., Mueller, P. Photoelectric Currents Across Planar Bilayer Membranes Containing Bacterial Reaction Centers. *Biophys. J.* 37:465-473 (1982)
- Pomerantz, M., Segmüller, A. High Resolution X-ray Diffraction From Small Numbers of Langmuir-Blodgett Layers of Manganese Stearate. *Thin Solid Films* 68:33-45 (1980)
- Roitt, I. *Essential Immunology*, Blackwell Scientific Publishing, Inc., 1980.
- Sagiv, J. Organized Monolayers by Adsorption. I. Formation and Structure of Oleophobic Mixed Monolayers on Solid Surfaces. *JACS.* 102:92-98 (1980)
- Schwartz, S., Cain, J., Dratz, E., Blaise, J.K. An Analysis of Lamellar X-Ray Diffraction From Disordered Membrane Multilayers with Application to Data from Retinal Rod Outer Segments. *Biophys. J.* 15:1201-1233 (1975)

Seul, M., Eisenberger, P., McConnell, H.M. X-ray Diffraction by Phospholipid Monolayers on Single-Crystal Silicon Substrates. *PNAS* 80:5795-5797 (1983)

Stroud, R., Agard, D. Structure Determination of Asymmetric Membrane Profiles Using an Iterative Fourier Method. *Biophys. J.* 25:495-512 (1979)

Tieke, B., Lieser, G., Wegner, G. Polymerization of Diacetylenes in Multilayers. *Journal of Polymer Science.* 17:1631-1644 (1979)

Tscharner, V., McConnell, H. Physical Properties of Lipid Monolayers on Alkylated Planar Glass Surfaces. *Biophys. J.* 36:421-427 (1981)

Uzigiris, E., Kornberg, R. Two-dimensional Crystallization Technique for Imaging Macromolecules, with Application to Antigen-Antibody-Complement Complexes. *Nature* 301:125-129 (1983)

## INDEX

antibody-antigen complex	2, 127
arachidic acid	37, 39, 55, 60, 70
asymptotic solution	12
autocorrelation function (see Patterson function)	
auxiliary maxima	34, 125
Born approximation	15, 16
Bragg limit	34, 35
Bragg's law	27, 29
Bravais lattice	24
collapse pressure	38
constructive interference	24, 60
convolution operator	19
Coulombic potential	7
deconvolution	70
delta function, Dirac	10, 34
delta function, Fourier transform of infinite array	132
delta function, Kronecker	25
diacetylene	1
diacetylene polymer	41
differential cross section	17, 18
diffraction maxima, shifting and broadening	35, 55, 113, 134
diffraction, finite system	32
diffraction, infinite systems	24
diffraction, non-zero minima	60, 72, 112
dimyristoyl phosphatidylcholine	127
dipalmitoyl phosphatidylcholine	72, 127
direct methods, deconvolution	2, 70, 73, 138
direct methods, linear equations	70, 73, 122, 135
electron density distribution	17, 19
electron density distribution, projection	19, 20, 21
electron density profile	21
electron density profile, average unit cell	70, 91
electron density profile, multilayer	74, 75, 91, 101, 111, 119, 120

Ewald's sphere of reflection	25, 26, 27
film balance	37
Fourier synthesis	70, 122 142
Fourier transform	17
Frank's optics	44
Fraunhofer condition	12
Green's function	9, 11
Hamiltonian operator	7
haptens	127
holographic interferometry	124
homologous series	91, 122
immune system	127
immunoglobulin	127, 128, 129
incident beam-shape function	32
intensity function	45, 60, 101, 148
intensity function, calculated	101
intensity function, symmetric and anti-symmetric components	113, 148
interference function	32
interference function	34
isotherm	38
Langmuir-Blodgett	1, 2
Langmuir-Blodgett, film preparation	37
Lorentz correction	47
macrophage, guinea pig peritoneal	127, 129
membrane, transmembrane potential	2
membrane-membrane interaction	128, 129, 130
model, asymmetric	73
model, centrosymmetric	73
model, multilayer electron density profile	72, 73
model, physico-chemical	111, 112
model, step-function electron density	101, 102
momentum distribution	7, 44
mosaic spread	44, 46
multilayer profile, asymmetric	60
multilayer, profile box function	32
multilayers, oriented fatty acid	1

myristic acid	37, 40, 60
nickel filters	44
octadecyltrichlorosilane (OTS)	37
omega scan	44, 47
overlayer-induced ordering	124
Patterson function	2, 3, 19, 32, 55, 60, 101, 103, 118, 124
Patterson function, calculated	101, 103
Patterson function, unit cell	33, 70, 135
10,12 pentacosadiynoic acid	39, 40, 60
position sensitive detector (PSD)	44
powder patter	1
primitive vectors	24
proteins	1, 2
quantum mechanics	7
reciprocal lattice function (see interference function)	
refinement, box	3, 91, 74, 75, 102, 112, 122, 123, 144
refinement, corefinement	91, 124
resolution	44, 125
rocking curve	45
scattering, air	44
scattering, background	61, 72, 102, 114
scattering, equations one dimensional scattering theory	22
scattering, general theory	7
Schrödinger equation	8
secondary maxima (see auxilliary maxima)	
silicon-intensified target (SIT) detector	47
specular scattering	45, 46
structure amplitude	17
structure factor	17
synchrotron x-radiation source	47, 129



theta-two theta scan	27
ultra-violet radiation	41
unit cell profile structure factor	32
unit cell, average electron density profile	33
von Laue formulation	24, 28